# FEATURES OF APATITE IN KIMBERLITE FROM EKATI DIAMOND MINE AND SNAP LAKE: MODELLING KIMBERLITE COMPOSITION

by

Rachel S. Milligan

Submitted in partial fulfilment of the requirements
for the degree of Master of Science

at

Dalhousie University
Halifax, Nova Scotia
November 2017

**Table of Contents**

## List of Tables

## List of Figures

## Abstract

Magmatic volatiles ($H_2O$, $CO_2$, F, Cl) and the timing of fluid exsolution have implications for kimberlite melt composition, eruption and preservation of diamonds. Apatite, $Ca_5(PO_4)_3(F,Cl,OH)$, is a common groundmass mineral in kimberlite, often used as an indicator of volatile behaviour in igneous rocks because it is a major host for halogens, rare earth elements (REEs) and Sr. This study reports on the diversity of apatite in kimberlite, and explores its for indicating kimberlite volatile histories, using pipes from Ekati Diamond Mine and Snap Lake Mine, located in the Northwest Territories, Canada. Experimental partition coefficients from the literature for apatite and various crystallization media (silicate melt, carbonate melt, aqueous fluid), are employed to estimate concentrations of trace elements in hypothetical melts coexisting with kimberlitic apatite. The constructed models are consistent with kimberlitic-apatite crystallization from a melt nearer to carbonate composition, while some apatite grains preserve evidence of magmatic fluid separation from the kimberlite melt. Evidence from groundmass apatite supports the current models for kimberlite eruption and can be a robust way to assess volatile histories in kimberlite pipes.

## List of Abbreviations and Symbols Used

| | |
|---|---|
| ° C | degrees Celsius |
| apfu | atoms per formula unit |
| BSE | back scattered electron |
| C.I. | contamination index |
| CK | coherent kimberlite |
| CL | cathodoluminescence |
| EMP | electron microprobe |
| GPa | gigapascal |
| HK | hypabyssal kimberlite |
| HREE | heavy rare earth element |
| HFSE | high field strength element |
| KPK | Kimberley-type pyroclastic kimberlite |
| LA-ICPMS | laser ablation-inductively coupled plasma mass spectrometry |
| LILE | large ion lithophile element |
| LREE | light rare earth element |
| MREE | middle rare earth element |
| mm | millimeter |
| ppm | parts per million |
| REEs | rare earth elements |
| RVK | resedimented volcaniclastic kimberlite |
| SEM | scanning electron microcscopy |
| SL | Snap Lake |
| T | temperature |
| µm | micrometer |
| WDS | wavelength dispersive spectroscopy |
| wt % | weight percent |

**Acknowledgements**

There are several people I would like to thank for their help, guidance and support in bringing this thesis together and getting me to the finish line.

Funding for this research was generously provided by the Northwest Territories Geological Survey, DeBeers Exploration, and through research grants from the Geological Society of America, Shell Canada, and the National Sciences and Engineering Research Council of Canada Discovery and CRD grants (to Yana Fedortchouk). I whole-heartedly thank the convenors of the 11$^{th}$ International Kimberlite Conference for the financial support to present my research at the meeting in Gaborone, Botswana; a truly unique experience for an MSc. student.

I am grateful to DeBeers Canada for providing samples and bulk rock data for Snap Lake and BHP Billiton Diamonds Inc. for supplying Ekati kimberlite samples. I thank Drs. Zoltan Zajacz and A. Sasha Tsay for their invaluable assistance with operation of the LA-ICPMS and subsequent volumes of data. Dr. Michael Robertson warrants special thanks for his generous help with the SEM-CL equipment and data, and his continued interest and support during the development of this research. I am also grateful for technical EPMA support from Dan MacDonald, and technical SEM support from Xiang Yang. I thank Ryan Kressall for providing his unpublished perovskite data from the Ekati kimberlite pipes, which is used for melt models in the discussion section.

I would like to thank the members of my supervisory committee (Drs. Yana Fedortchouk, Philippe Normandeau, Alexandrina Fulop and James Brenan) for their continued support and advice throughout this process. I'm continually grateful for the unique perspectives of Philippe and Alexandrina, as well as their valuable experience and guidance. James – partition coefficients took on a whole new meaning for me during the research for this project, and without your help they would have haunted me far longer and with more malice than they managed these past two years. Yana – I sincerely appreciate the opportunity to work with you for so many years. I have learned so much under your tutelage and I am so grateful for your support and guidance.

I would like to express my gratitude to everyone I have met during my time at Dalhousie. Thanks to the members in our petrology group for the engaging and animated discussions. A special thanks to Bryan for the innumerable consultations, conversations and deliberations about apatite, and to everyone in our office for tolerating all the apatite talk: Erin, Taylor, Laura, Cody and Xueni. I would also like to thank the outstanding administrative and technical staff in our department for all their assistance: Darlene, Norma, Anne, Brant and John T.

I am forever grateful to my family, who can always give me a laugh when I need one, and whose unwavering support has gotten me to where I am today.

Lastly, I want to acknowledge some who saw me through the longest days in this process. Ian and Samantha - thanks for being my rocks in the storm.

# CHAPTER 1 INTRODUCTION

## 1.1 Apatite in magmatic systems

Calcium-phosphate apatite, a subgroup of the apatite Supergroup [$A_{10}(ZO_4)_6(X)_2$], is ubiquitous in the Earth, and is the primary host for phosphorous in most igneous systems. The abundance of its major constituents, Ca and P, in the crust allows for abundant apatite crystallization throughout many different geologic settings. The general formula $Ca_5(PO_4)_3(F,Cl,OH)$ along with a sturdy and tolerant structural arrangement in $P6_3/m$ space group symmetry allows for easy adoption of elemental substitution (Hughes et al. 1989; Hughes and Rakovan 2002; Pan and Fleet 2002). The result is a diverse spectrum of apatite species and compositions.

The plethora of complex chemical variants of apatite and incorporation of important trace elements (REEs, Sr) makes it an excellent indicator of magmatic behaviour and evolution. The usefulness of this mineral to estimations of volatile, hydrothermal and magmatic histories has been widely explored and documented (Korzhinskiy 1981; Kusebauch et al. 2015a; Piccoli and Candela 1994), yielding abundant data outlining specific apatite chemical signatures, in a wide range of magmatic environments (Belousova et al. 2002; Mao et al. 2016; Piccoli and Candela 2002).

One rock where the applicability of apatite chemistry has not been fully investigated is in kimberlite. Highly complex and not fully understood, the primary composition, evolution, and fluid behaviours of kimberlite magmas are obscured by host rock contamination, volatile loss and extensive hydrous alteration. Since the properties of interest cannot be directly measured, groundmass minerals can serve as secondary indicators of magmatic and fluid behaviour and composition in kimberlite magmas. Here, crystal chemistry and occurrence of groundmass apatite from seven kimberlite bodies (six pipes at Ekati Diamond Mine and Snap Lake kimberlite dyke) are used to model kimberlite composition and volatile eruption behaviours.

Apatite grains are analyzed from several kimberlite pipes with varied geological features. Apatite grains are examined for abundance, texture, zoning, cathodoluminescence, and major and trace element compositions. Since apatite is known to be highly sensitive to

magma and fluid conditions, variation in kimberlitic volatiles, magmatic composition and facies should be reflected by variation in groundmass apatite crystallization and composition. Data and interpretations from natural apatite samples will be compared to existing models for kimberlite eruption and diamond preservation.

### 1.1.1 Variation in apatite composition

In the hexagonal crystallographic group, the apatite unit cell has six $ZO_4$ tetrahedra, two volatile anions, four A1 polyhedral sites in nine-fold coordination with oxygen, six A2 sites in six-fold coordination with oxygen and one bond to the stacked halogen anion column. Apatite is particularly useful as an indicator of magmatic fluid behaviour because it incorporates halogens/

Variation in the halogen site occupant is commonly restricted to the three anions seen in the formula (F,Cl,OH), though some other elements may occupy the site to enable charge-compensating coupled substitutions into other sites. Fluorapatite is the most common species of calcium-phosphate apatite, crystallizing in almost all magmatic settings. Fluorapatite, however, is not necessarily a pure-halogen endmember, and, on average, contains 0.2 atoms per formula unit (apfu) OH (in a 1-anion site). Cl is the least common component found in the anion column, and is forced to lie significantly outside the mirror plane of the column because of its large radius. Non-ideal structural arrangement of the apatite structure, caused by incorporation of significant Cl into the anion column, can result in crystallization of the mineral in the $P2_1/b$ space group (Hughes et al. 1989).

The extent to which the three major anion components (F, Cl, OH) can exist in solid solution in the apatite structure is still under investigation. Occupation of the anion column by two or more species of anion, while possible, would require extensive structural rearrangement, including the creation of new anion sites, and rearrangement of the connective A2 polyhedral sites (Hughes et al. 1989). Boyce et al. (2014) pointed out the issue these structural constraints pose to accurately using apatite halogen concentrations as a monitor of coexisting fluids. If incorporation of a halogen species into apatite is impeded because of strain on the structure, proportional concentrations of F, Cl and OH in apatite would not be representative of the surrounding conditions during crystallization. It is suggested that, rather than the application of Nernst partition coefficients, halogens in

apatite be treated as major elements (Boyce et al. 2014), or that, when modeling hydrothermal systems, halogen concentrations are calculated based on activities and halogen-exchange equilibrium constants (Boyce et al. 2014; Webster and Piccoli 2015). This method has been employed by several studies (Korzhinskiy 1981; Kusebauch et al. 2015a; Kusebauch et al. 2015b; Piccoli and Candela 1994). In this study, halogen site occupancy is briefly examined in kimberlitic apatite grains, and considered for evidence of fluid exsolution in a semi-quantitative sense.

Other elements residing in apatite can reasonably be used as monitors of magmatic fluid activity within a kimberlite. Direct substitutions into the apatite Ca polyhedral sites by trace elements ($Sr^{2+}$, $Ba^{2+}$, $Mn^{2+}$, $Pb^{2+}$ etc.) and the tetrahedral phosphate site ($VO_4^{3-}$, $AsO_4^{3-}$ etc.) are common. Replacement of the cation and phosphate groups by other elements with variable valences (such as $REE^{3+}$ ions) can be attained by balancing charge with coupled substitutions. The main mechanisms for incorporation of $REE^{3+}$ ions into the apatite structure are:

$$REE^{3+} + Na^{+} = 2Ca^{2+} \quad (1)$$

$$REE^{3+} + SiO_4^{4-} = Ca^{2+} + PO_4^{3-} \quad (2)$$

$$2REE^{3+} + [v] = 3Ca^{2+} \quad (3)$$

Where $[v]$ represents a vacancy in the apatite structure. Apatite is known to incorporate significant amounts of REEs, to the point of crystallizing many natural and synthetic REE-apatite species (Pan and Fleet 2002; and references therein). Because of their sensitivity to surrounding magmatic and fluid conditions, and their ready uptake into Ca-phosphate apatite, the REEs and their methods of substitution are critical factors in trace element modelling. These indicators, along with careful review of available partition coefficients, coexisting minerals (e.g. perovskite) and features of apatite should allow us to make an estimate of the relative timing of fluid exsolution compared to apatite crystallization. Since fluid exsolution is proposed to be the driver for kimberlite eruption (Russell et al. 2012), and apatite is crystallizing as a groundmass phase (late in magmatic evolution), apatite should retain some chemical signature indicating exsolution before, after or during crystallization.

### 1.1.2 Modelling trace element uptake into apatite

To constrain the conditions under which apatite was crystallizing in the selected kimberlite pipes, Nernst-style partition coefficients (D) are used to reconstruct hypothetical melts coexisting with apatite. These models will be compared to bulk rock data for the studied kimberlite pipes.

Distribution of trace elements between apatite and kimberlite melts has not previously been studied, nor is the exact composition of kimberlite melts well established. Two possible end-member compositions for kimberlite melt (silicate melt vs. carbonate melt; e.g. Kopylova et al. 2007; Mitchell 2004; Price et al. 2000; Sparks et al. 2009) were tested using coefficients from the literature for apatite and similar liquids (i.e. basanite/basalt melts, carbonatite melts). To reduce the error of using factors from melts with attributes unlike kimberlite, the effects of external conditions on D values of elements entering apatite are examined in the following sections, specifically the REEs. Then it is possible to evaluate how trace element partitioning would change in the presence of a kimberlitic melt. Existing partitioning data for trace elements between apatite and various melt compositions and temperatures of interest, i.e. similar to potential kimberlite conditions, are represented in Fig. 1.1, with references provided in Table 1.2.

***Temperature controls*** Watson and Green (1981) explored the effect of temperature on element partitioning between apatite and silicate melts. With partition coefficients experimentally determined at two temperatures, they estimate isotherms as a function of $SiO_2$ content in the melt (illustrated in Fig. 1.2a). Their isotherms define a decrease in the mean partition coefficient by a factor of ~2 for the 130 °C increase in temperature between their sets of experiments. Using this model, and extrapolating for another 130 °C increase, the expected mean partition coefficient trend for 1210 °C (Fig. 1.2a). Comparing these results with the partition coefficients reported by Prowatke and Klemme (2006) at 1250 °C, the isothermal model proposed by Watson and Green (1981) is inconsistent with the experimental data from the later study. Furthermore, the isotherms converge at approximately 47 wt% $SiO_2$. Therefore, partitioning has low T dependence in melts with less silica, such as kimberlite melts. Additionally, these results demonstrate that the role of T in controlling the partitioning of elements between apatite and silicate melts is not fully understood, and further experiments are needed to constrain this parameter.

***Melt composition*** Klemme and Dalpé (2003) evaluated the effects of melt composition on distribution coefficients for REEs into apatite. They compared data from their own study with that from Watson and Green (1981) and defined trends for changes in $D_{REE}$ with changes in melt proportions of $P_2O_5$, CaO and $SiO_2$. Here (Fig. 1.2b) data from the study by Prowatke and Klemme (2006) is plotted with the previously established trends and note that data for $P_2O_5$ and CaO contents in the melt are consistent with the trends. $SiO_2$ contents, however, produce $D_{REE}$ values which aren't predicted by the trend. Generally, $D_{REE}$ values decrease with decreasing melt $SiO_2$ contents (decreasing melt polymerization), which is consistent with previous studies (Ryerson and Hess 1978; Watson 1976); however, the complex behaviour of $SiO_2$ in melt systems results in less predictable models for $D_{REEs}$.

***Pressure*** Partition coefficients are plotted as a function of pressure and are plotted in Fig. 1.2c. The effects of changing pressure on REE distribution appear to be minimal.

***Apatite composition*** Depending on the starting materials and conditions for the experiments conducted, partitioning data could be affected by the starting composition of apatite used. In Fig. 1.2d $SiO_2$ concentrations in apatite are compared to $D_{REE}$ determined in the experiments. The data from Watson and Green (1981) do not show any correlation to $SiO_2$ content of the apatite. Partitioning data from Prowatke and Klemme (2006), however, seem to have negative correlation of $D_{REE}$ with $SiO_2$ content in the apatite. This apparent trend could be the result of other factors, such as changing melt composition, or preferential operation of different substitution mechanisms.

***Melt halogens*** Watson and Green (1981) conducted experiments to determine apatite/melt partition coefficients with variations in melt composition, temperature and volatile proportions. Though they cited no correlation between halogen species activity and REE partitioning, Fleet and Pan (1997) claimed to recognise a positive trend between $H_2O/FeF_3$ in the run products and $D_{REEs}$ determined by Watson and Green (1981) in experiments with an aqueous phase. The exact relationship between these variables is not clear, though the possibility of melt halogen control on REE partitioning should not be ignored.

For this enquiry into changes in distribution coefficient, these external parameters operate as a function of melt polymerization. Generally, $D_{REE}$ should decrease with decreasing melt

polymerization, as determined by two-liquid experimental partition coefficients (Ryerson and Hess 1978; Watson 1976).

### 1.1.3 Apatite-biotite thermometry

Constraints are still being determined for temperatures of kimberlite melts at the time of eruption and emplacement. A study by Fedortchouk and Canil (2004) used olivine-spinel and ilmenite-rutile thermometry to estimate temperatures of four kimberlite melts at the time of olivine-rim crystallization. For Leslie and Grizzly kimberlite pipes (also examined in this study) they calculated between 1015-1102 ºC and 1057-1133 ºC, respectively.

Here, the apatite-biotite thermometer calibrated by Zhu and Sverjensky (1992) is used, which calculates the exchange of F between apatite and biotite as a function of T. With the new calibration, they employed this thermometer on several different rock types, including one South African kimberlite sample from Hervig and Smith (1981), and calculated a temperature of 986ºC. These temperatures are compared with temperatures calculated from apatite-biotite xenocryst pairs in kimberlite samples from this study.

## 1.2 Kimberlite

Kimberlite is a complex and varied type of rock, crystallized from magma originating in the upper mantle. Rapid ascent and common explosivity is driven by high proportions of volatiles; however, the exact nature of kimberlite magmatism is still under debate. Additionally, the composition of kimberlite magmas and the magmatic volatiles are extensively obscured by wall-rock contamination, volatile loss and hydrous alteration. Since many of the relevant intensive variables are difficult to measure, groundmass mineral analysis is a viable method of obtaining data about the physical and chemical attributes of kimberlite liquids during the eruption process.

Despite being a relatively common phase in kimberlite, the occurrence and habit of groundmass apatite has previously been documented only by a few studies (Armstrong et al. 2004; Larson and Amini 1981; Votyakov et al. 1989; White et al. 2012). More recently, research is moving towards obtaining quantitative analyses of groundmass apatite and beginning to probe its potential for indications of late-stage magmatic conditions within kimberlite melts (Abersteiner et al. 2017; Malarkey et al. 2010). Considering the extensive data available for apatite and its use as an indicator of magmatic and hydrothermal

condition, apatite is an ideal candidate for approaching some of the remaining questions concerning the late stages of kimberlite magmatism.

Other minerals have the potential to incorporate trace elements, which would obscure the evaluation of melt composition from apatite distribution coefficients. For example, perovskite, another common groundmass mineral in kimberlite, is known to incorporate REEs and HFSE's. Perovskite is present as a groundmass phase in kimberlite from Ekati Diamond Mine (Nowicki et al. 2004); however, it is absent throughout the Snap Lake kimberlite (Kopylova and Mogg 2010). Partition coefficients for trace elements between perovskite and kimberlite/carbonatite melts have been determined by Beyer et al. (2013), and are included in Fig 1.1 for comparison with those of apatite. The presence of perovskite, and its relationship to the timing of apatite crystallization, will be considered during trace element modelling of the selected kimberlite samples.

### 1.3 Objectives and organization of the study

The primary aims of this study are to:

1) Observe and record the variations in apatite occurrence, texture, habit and composition between different kimberlite bodies,
2) Evaluate apatite as a kimberlite indicator mineral for exploration, and
3) Explore the use of apatite to discern magmatic volatile and trace element behaviours during the late stages of kimberlite eruption.

To achieve these goals, apatite grains are analyzed from several kimberlite pipes with varied geological features, summarized in Table 1.1. Apatite grains were examined for abundance, texture, zoning, cathodoluminescence, and major and trace element composition. These data were then compared with data obtained from apatite grains from various environments, including other ultra mafic and alkaline igneous rocks to assess the use of detrital apatite to indicate a kimberlitic source.

Trace element analyses were used with partition coefficients from the literature to examine variations in elemental distribution between apatite and melt in the different kimberlite samples. This can have indications for melt composition, temperature, presence of fluids, phosphorous saturation and trace element behaviours in the various kimberlite melts

studied. Apatite data on these factors was then compared to current models of eruption for each kimberlite pipe, and made conclusions for the applicability of apatite as an indicator of magmatic behaviour in kimberlite melts, and its uses in exploration.

Since apatite is known to be highly sensitive to magmatic conditions, variation in kimberlitic volatiles, magmatic composition and eruption should be reflected by variation in groundmass apatite crystallization and composition.

The remaining section of the introduction reviews the geological background for the selected kimberlite bodies. Chapter 2 overviews the methods which were applied to locate and analyse apatite grains in the selected samples. The results of apatite occurrence and composition as found in the kimberlite pipes are outlined in Chapter 3. Chapter 4 discusses the potential of apatite for use in kimberlite exploration, the origin and crystallization of kimberlitic apatite, and the support of data from this study for kimberlite eruption models. The final section of this thesis, Chapter 5, concludes the research and outlines potential avenues for future inquiry.

### 1.4 Geological background

To test the possibility of using apatite as an indicator of kimberlitic fluid and magmatic composition, kimberlite pipes were selected whose different geological features suggest varied volatile behaviours (Table 1.1). Selecting pipes with diverse eruption styles enables us to test the fluid and trace element models from apatite for a variety of potential volatile histories. Six kimberlite pipes at Ekati Mine (Koala, Panda, Leslie, Misery, Grizzly and Beartooth) and the Snap Lake Mine kimberlite dyke are all located in the Slave craton, Northwest Territories, Canada (Fig 1.3a). Here, the main features of the selected kimberlite pipes are outlined, as well as current models for eruption and volatile exsolution.

***Ekati kimberlite pipes*** The sampled kimberlite bodies from the Ekati Diamond Mine all comprise discrete, single-pipe formations, excepting Misery, which is seen to have multiple cross-cutting lobes. Kimberlite materials in this area have been extensively studied (Armstrong et al. 2004; Fedortchouk et al. 2005; Fedortchouk et al. 2010; Nowicki et al. 2004; Nowicki et al. 2008), and generally fall within the geochemical range of Group 1 kimberlite (Nowicki et al. 2008). They comprise four steep sided pipes filled with various

volcaniclastic materials (Panda, Koala, Misery and Beartooth) and two steep sided pipes which are filled with hypabyssal kimberlite facies (Leslie and Grizzly). Panda is filled with discontinuous steeply dipping units of resedimented volcaniclastic kimberlite (RVK) and volcaniclastic material, some of which are bedded, and which are primarily distinguished based on proportions of macrocrystic olivine. The kimberlite also contains minor intrusive units of coherent kimberlite (CK) and is juvenile-olivine rich. Koala kimberlite is unique, in that it contains sub-horizontal bedding of Kimberley-type pyroclastic kimberlite (KPK), using the terminology from Scott Smith et al. (2013), with sharp transitions, subdivided into seven distinct phases with minimal resedimentation (Nowicki et al. 2004). Leslie and Grizzly pipes contain intra-crater CK at similar erosion levels to the volcaniclastic kimberlite pipes, indicating direct, shallow emplacement of the kimberlite melt in these pipes (Berg and Carlson 1998). The Leslie kimberlite preserves minor amounts of volcaniclastic material around the margins of the pipe (Nowicki et al. 2004). Misery is a complex multi-phase pipe comprising several overlapping units of KPK, CK, RVK and other distinct volcaniclastic units. Relative locations of the pipes on the Ekati property are shown in Fig. 1.3b.

The current models of eruption for kimberlite generally involve two stages of volatile degassing. The first is decarbonational degassing, which is the production of $CO_2$ vapour in response to mantle wall-rock assimilation and dissolution of orthopyroxene and clinopyroxene. This process is thought to be the driver for buoyancy-fueled ascent of kimberlitic magmas. The volume change and overpressure caused by release of $CO_2$ gases at depth (>2 GPa) propels the magma into the crust and to the surface in a matter of hours (Russell et al. 2012; Stone and Luth 2016). The second degassing event occurs closer to the surface (<1 GPa), where decompression results in the release of $CO_2$ and $H_2O$ gases and begins the process of crater formation. The depth at which crater formation and decompressional degassing begin to occur is a complex function of melt composition, and initial concentrations of $SiO_2$ and $H_2O$ in the melt (Moussallam et al. 2016; Moussallam et al. 2015). This second degassing process also causes a large volume change and speeds ascent of the kimberlite magma. The larger volume of volatiles exsolved at depth creates increased buoyancy in the kimberlite melt, and results in a faster ascent rate.

Based on diamond dissolution studies (Fedortchouk et al. 2010; Zhang et al. 2015), Misery, Panda, Beartooth and Koala likely had a $H_2O$ fluid present during the kimberlite eruption, while Grizzly and Leslie kimberlite melts had lost their volatiles to the open system. This would have resulted in extremely rapid ascent of Misery, which had the earliest release of volatiles (Zhang et al. 2015), as well as the other volcaniclastic kimberlite bodies, and slower ascent of the dry magmas, Leslie and Grizzly, resulting in the observed diamond grades at the surface (given in Table 1.1). Longer residence time because of a slow magmatic ascent rate leaves more time for diamond dissolution and results in a lower grade kimberlite.

While Leslie and Grizzly have been shown to have lost volatiles (Fedortchouk et al. 2010), and are both comprised of magmatic kimberlite material, they did have crater formation before the magmatic infill. In this case, one possibility involves the model proposed by Hetman et al. (2004), in which the volatile phase is physically separated from the magma, forming a fluid degassing front ahead of the magma ascent. The volatiles explosively form a crater with little or no magmatic material incorporated, and the kimberlite magma follows and quietly fills in the open crater with apparently intrusive textures.

***Snap Lake dyke*** The Snap Lake kimberlite is unique due to its intrusive emplacement as a sub-horizontal dyke, and its extensive alteration and complex interactions with the host rock. Multiple zones with clear mineralogical differences have previously been interpreted as being a result of separate magma batches, differences in magma viscosity, or localized alteration (Field et al. 2009; Gernon et al. 2012; Kopylova and Mogg 2010). A recent study by Fulop et al. (2017) records a complex history of metasomatic alteration of the Snap Lake dyke, from the outer edges to the core by deuteric kimberlite fluids. Per Fulop et al. (2017), interaction of kimberlitic liquids with the surrounding granitoid wall-rocks, as well as assimilation of this material has resulted in progressive zones of alteration from the outward contacts of the dyke into the centre (Fig 1.4). The centre represents the freshest expression of kimberlite material in the dyke; however, there is still significant alteration compared to the kimberlite at Ekati, and no juvenile olivine is preserved. These transitional zones have been described as six units, hypabyssal kimberlite (HK;1-6), where HK1 and HK2 are the least altered units, in the centre of the dyke. HK3, HK4 and HK6 are

progressively more altered units, on the margins of the dyke. Unit HK5, describes a specific subset of alteration facies where the kimberlite material in the least altered units (HK1 and HK2) is more extensively altered in areas surrounding large xenoliths. The dyke has variable thicknesses (2-16 m), therefore the fresher units of the dyke (HK1, HK2, HK5) are discontinuous in the kimberlite body.

The hypabyssal Snap Lake dyke formed by a similar model to the other hypabyssal kimberlite melts described above. Early fluid exsolution and degassing would leave behind a slow-moving magma. The lack of a crater in this instance could indicate that the pressure differential of the volatiles at shallow levels was not enough to breach the surface in an explosive manner, but likely aided in conduit formation for the following magma. The Snap Lake dyke also shows significant metasomatic alteration by high-T fluids. It is possible that the kimberlite magma, though showing low explosivity, was reaching fluid saturation through decompression as it neared the shallow crust.

Table 1.1 Geology and age of selected kimberlite pipes, terminology from Scott Smith et al. (2013)

| Kimberlite | Dominant geology | Age (Ma) | Diamond grade (ct/t)[c] |
|---|---|---|---|
| Beartooth | RVK | 53.1 ± 4.6[a] | 1.2 |
| Grizzly | intra-crater CK | 51.5 ± 5.2[a] | 0.5 |
| Koala | KPK | 53.3 ± 0.9[a] | 1 |
| Leslie | intra-crater CK | 52.0 ± 6.6[a] | 0.33 |
| Misery | KPK | 2437 ± 25[a] | 4.19 |
| Panda | RVK | 52.9 ± 1.8[a] | 0.95 |
| Snap Lake | HK dyke | 523 ± 6.9[b] | 2 |

[a] Rb-Sr from Creaser et al. (2004)
[b] Rb-Sr from Heaman et al. (2004)
[c] Ekati grades from Fedortchouk et al. (2010) and references therein, Snap Lake grade from Field et al. (2009)

Table 1.2 Summary of experimental studies citing partition coefficient data between apatite and media within composition of interest.

| Mineral | Crystallization Media | Experimental Conditions | Partitioning Data | Reference |
|---|---|---|---|---|
| Apatite | Basanite melt | 0.75-2.0 GPa 950-1120 °C | La, Sr, Sm, Lu | Watson and Green (1981) |
| Apatite | Basalt, basaltic andesite, andesite melt | 1.0 GPa 1250 °C | REEs, Sr[a] | Prowatke and Klemme (2006) |
| Apatite | Calcium carbonatite melt | 1.0 GPa 1250 °C | REEs, Sr[b] | Klemme and Dalpé (2003) |
| Apatite | Aqueous fluid | 1.0 GPa 1000 °C | Sr, Ce, Gd | Ayers and Watson (1993) |
| Apatite | Aqueous fluid | 2.0 GPa 1100-1500 °C | F, Cl | Brenan (1993) |

[a] Full list of elemental partitioning data: Cs, Rb, Ba, Th, U, Nb, Ta, Y and REEs
[b] Full list of elemental partitioning data: Li, Be, Cs, Rb, Ba, Th, U, Nb, Ta, Y and REEs

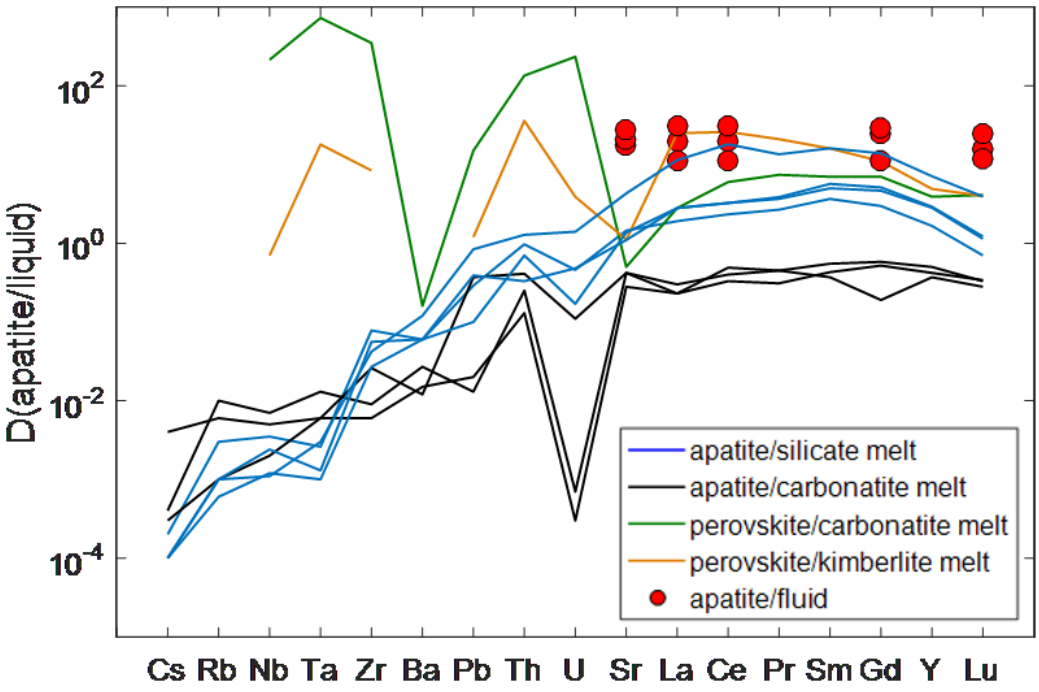


Figure 1.1 Experimental partition coefficients selected for use in this study. Aqueous fluid data from Ayers and Watson (1993), carbonatite data from Klemme and Dalpé (2003), basalt data from Prowatke and Klemme (2006), basanite data from Watson and Green (1981) and perovskite data from Beyer et al. (2013).

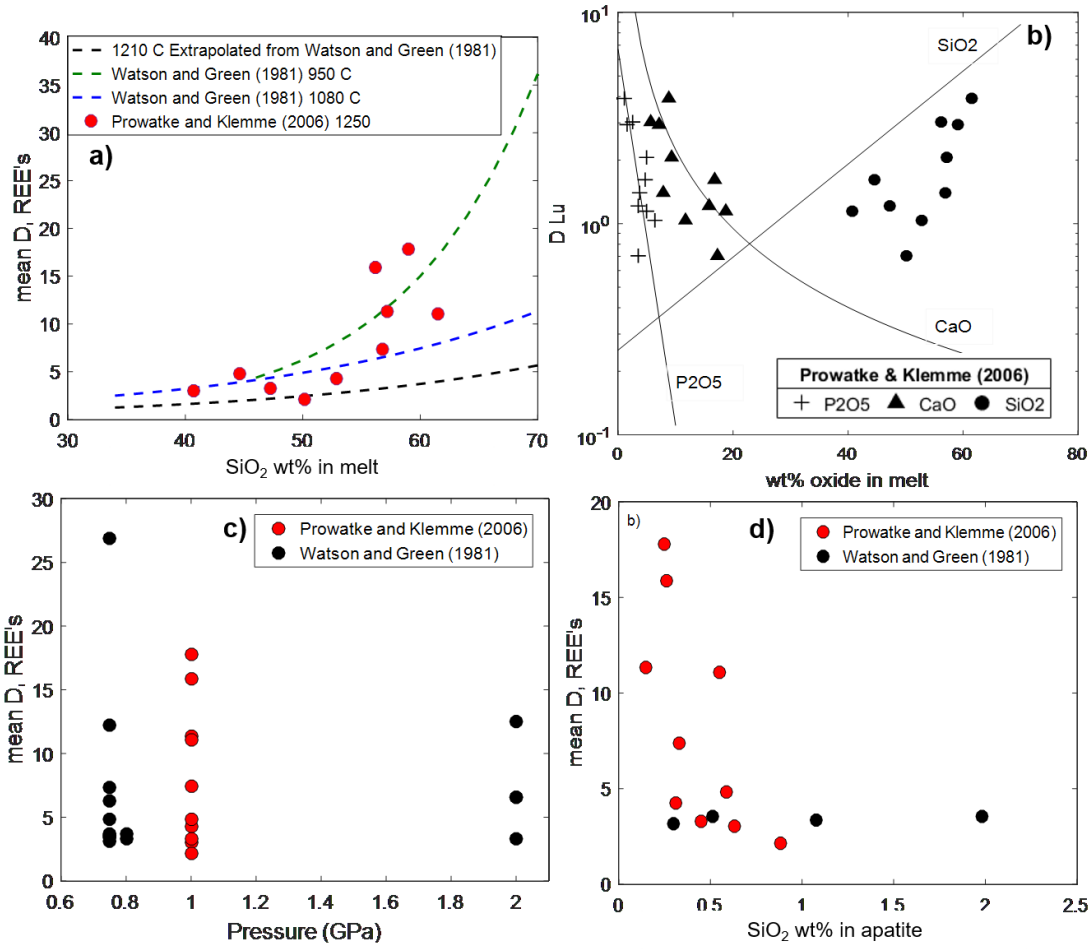


Figure 1.2 a) Isotherms defining REE partitioning behaviour based on $SiO_2$ content in the melt as defined by Watson and Green (1981) compared to data from Prowatke and Klemme (2006), b) Klemme and Dalpé (2003) defined curves for REE partition coefficient dependence on major element oxide concentrations in melt, compared to major element oxide data from Prowatke and Klemme (2006); circles $SiO_2$, triangles CaO, crosses $P_2O_5$, c) comparison of partitioning data for REEs with concentration of $SiO_2$ in apatite produced in experiments (Prowatke and Klemme 2006; Watson and Green 1981).

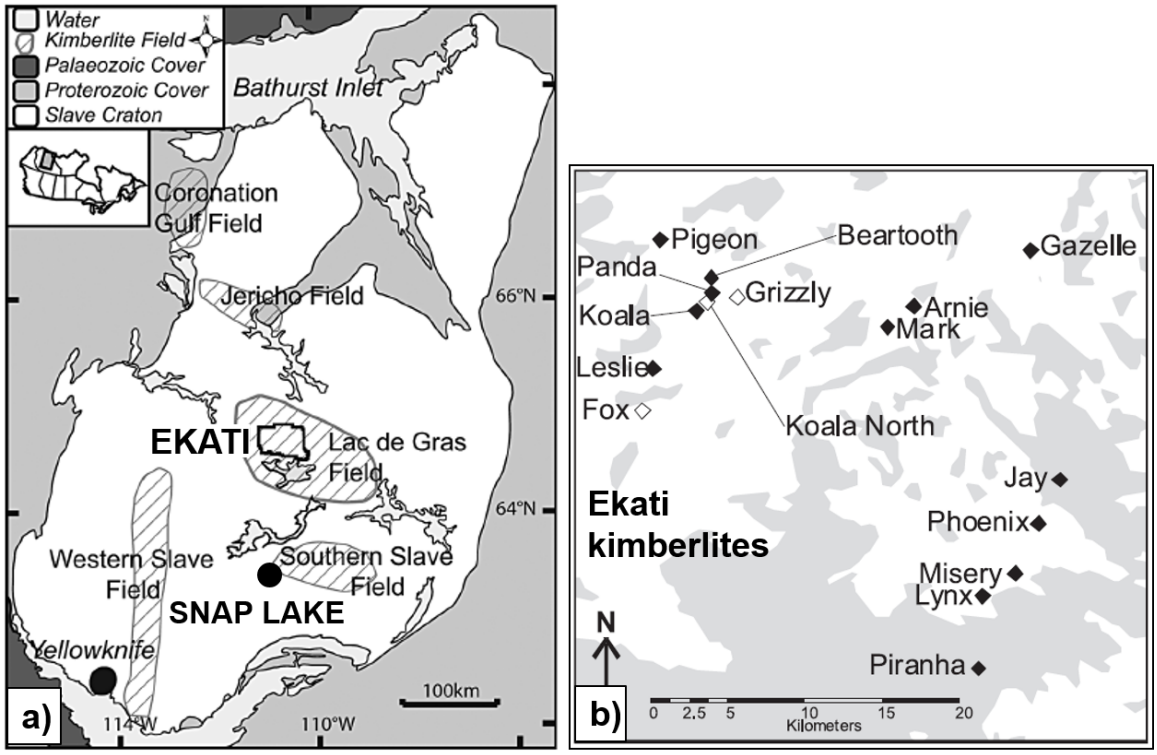


Figure 1.3 a) Map of Slave Craton with locations of Ekati and Snap Lake mines, modified after Porritt et al. (2012), b) map of Ekati property showing locations of selected kimberlite pipes, modified after Gurney et al. (2004).

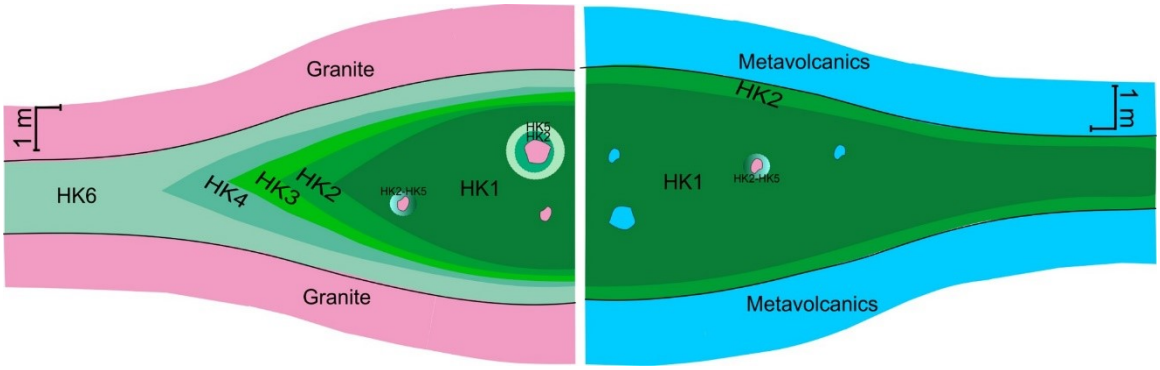


Figure 1.4 Schematic cross section of Snap Lake kimberlite dyke in contact with host rock granite and metavolcanics. Adapted from Fulop et al. (2017).

# CHAPTER 2 SAMPLES AND ANALYTICAL METHODS

## 2.1 Samples

Kimberlite samples from Ekati pipes were provided to Yana Fedortchouk by BHP Billiton Diamonds Inc. and two polished sections from each of the six selected pipes are used for the purposes of this study. Polished sections from Snap Lake kimberlite were provided by DeBeers Canada. The sections represent a cross-section through the dyke sampling from each of the kimberlite alteration zones (HK1-6). A total of 44 polished sections from all seven kimberlite bodies were examined for use in the current study. The 32 sections from Snap Lake were studied with a petrographic microscope and with a scanning electron microscope, and specific slides were selected for further examination based on presence of representative apatite textures and an even distribution of samples from each section of the dyke. Table 2.2 summarizes total number of quantitative analyses obtained in each kimberlite by both electron probe micro analyser (EMPA) and laser ablation inductively coupled plasma mass spectrometry (LA-ICPMS). A full list of samples is provided in Appendix A.

Mineral identification and study of apatite was done by back scatter electron (BSE) imaging and energy dispersive spectroscopy (EDX). A JEOL 8200 EPMA operated with 15 kV electron beam at Dalhousie University, and a TESCAN MIRA 3 LMU variable pressure Schottky field-emission scanning electron microscope (FE-SEM) operated with a 20 kV electron beam at Saint Mary's University were used to observe the occurrence and image various textures of apatite in the samples of interest.

## 2.2 Electron Microprobe

Quantitative analyses of apatite were obtained through wavelength dispersive spectroscopy (WDX) with 15 kV electron beam, 10 nA beam current and 10 μm spot size on a JEOL 8200 EPMA at Dalhousie University for apatite and biotite. Operating conditions for analyses of biotite were 15 kV, 20 nA and 10 μm spot size. Peak count times and primary elemental standards for the measured elements in both apatite and biotite are listed in Table 2.1, data reduction was performed using ZAF model. An attempt was made to analyze both euhedral (c-axis perpendicular) and elongate (c-axis parallel) sections in apatite to reduce

the effect of crystal orientation on F-analysis error (Stormer et al. 1993). To assess a possible overestimation of F content in WDX analyses, two neighbouring grains of the same apatite variety, with both hexagonal and prismatic shape, were analysed and compared. Hexagonal sections were found to have higher F content and possible F overestimation of ~10-15 % is estimated in c-axis parallel analyses with the EPMA.

### 2.3 Cathodoluminescence

Cathodoluminescence (CL) study of apatite was undertaken to reveal zoning and textures not visible with BSE imagery. CL images and spectra were obtained using a JEOL LV5900 SEM equipped with a Gatan MonoCL3 cathodoluminescence system at Acadia University. Imaging was done at 10 kV with a beam current of 0.5 nA. Spectra were collected at 20 kV with 0.5 nA beam current. Where an image of apatite was distorted by the presence of carbonate and its persistent long-wavelength luminescence, an Edmund subtractive dichroic red-block filter with a cut-off wavelength of 605 nm was inserted before the photo-multiplier tube for the imaging process and removed before the collection of spectra. This type of short-wavelength filter allows transmission of blue-UV luminescence, but limits transmissivity of luminescence at the long-wavelength end of the spectrum. Carbonate materials commonly display persistent, or "long-lived" luminescence within the orange-red spectrum, which can cause artefacts and streaking on the image seen in SEM-CL systems (Reed and Milliken 2003; Robertson and Gibson 2014).

### 2.4 Laser Ablation ICP-MS

Trace elements and REE were analyzed by LA-ICPMS done using an NWR 193 UC laser ablation system attached to an Agilent 7900 quadrupole ICP-MS. Laser energy density was maintained at 5.2 J/cm$^2$ with 5 Hz repetition rate, and the oxide production rate was monitored using the ThO/Th ratio (0.3%). NIST610 synthetic glass was used as an external standard, and was measured twice regularly between intervals of 15-20 analyses. The spot size was selected on a grain-by-grain basis depending on the grain size, presence of inclusions or cracks, and the possibility of zoning. Spot sizes ranged from 8 μm to 35 μm (mean 13 μm) depending on the size of the apatite crystal. As the relative sensitivities for different elements became somewhat dependent on the beam size at diameters <25 μm (up to about 10% relative deviation), the standard was measured each time with spot sizes

of 25 µm and 10 µm. Unknown analyses using spot size of 15 µm or less were integrated with data from standard measured with 10 µm spot size. Similarly, analyses with a spot size >15 µm were integrated with data from the standard measured with a 25 µm spot. The following ions were counted for apatite composition: $^{11}$B, $^{23}$Na, $^{25}$Mg, $^{27}$Al, $^{29}$Si, $^{31}$P, $^{39}$K, $^{44}$Ca, $^{45}$Sc, $^{49}$Ti, $^{51}$V, $^{53}$Cr, $^{55}$Mn, $^{56}$Fe, $^{75}$As, $^{85}$Rb, $^{88}$Sr, $^{89}$Y, $^{90}$Zr, $^{93}$Nb, $^{133}$Cs, $^{137}$Ba, $^{139}$La, $^{140}$Ce, $^{141}$Pr, $^{146}$Nd, $^{147}$Sm, $^{153}$Eu, $^{157}$Gd, $^{159}$Tb, $^{163}$Dy, $^{165}$Ho, $^{166}$Er, $^{169}$Tm, $^{172}$Yb, $^{175}$Lu, $^{181}$Ta, $^{208}$Pb, $^{232}$Th, $^{238}$U. Data quantification was conducted with the software SILLS (Guillong et al. 2008). As an internal standard, CaO wt% from EPMA data was used, previously obtained on the same grains.

Table 2.1 Peak count times and primary standards used for EPMA of fluorapatite and biotite

| Elements analysed | Fluorapatite | | Biotite | |
|---|---|---|---|---|
| | peak count time (s) | standard | peak count time (s) | standard |
| Ca | 20 | Durango fluorapatite | 20 | Kakanui kaersutite |
| P | 20 | Durango fluorapatite | | |
| Sr | 20 | Celestite | | |
| Si | 20 | Sanidine | 20 | Sanidine |
| Ba | 20 | Barite | | |
| K | 20 | Sanidine | 20 | Sanidine |
| Na | 40 | Jadeite | 20 | Jadeite |
| Mn | 20 | Pyrolusite | 20 | Pyrolusite |
| V | 20 | V-metal | | |
| Fe | 20 | Garnet 12442 | 20 | Garnet12442 |
| Mg | | | 20 | Kakanui kaersutite |
| Al | | | 20 | Sanidine |
| Ti | | | 20 | Kakanui kaersutite |
| Cr | | | 20 | Cr-metal |
| La | 20 | $LaPO_4$[a] | | |
| Ce | 20 | $CePO_4$[a] | | |
| Pr | 20 | REE glass[b] | | |
| Nd | 20 | REE glass[b] | | |
| Cl | 30 | Tugtupite | 30 | Tugtupite |
| F | 30, 60[c] | Durango fluorapatite | 60 | Durango fluorapatite |

[a] Synthetic oxides
[b] Ca-Al silicate glass doped with REEs (Drake and Weill 1972)
[c] Fluorine analyses were conducted with 30s or 60s count times to examine the extent of the c-axis parallel analysis problem on the selected samples at these EPMA conditions

Table 2.2 Total quantitative apatite analyses obtained for each kimberlite

| Kimberlite | | Number of slides | Number of EPMA analyses | Number of LA-ICPMS analyses |
|---|---|---|---|---|
| Koala | | 2 | 52 | 19 |
| Leslie | | 2 | 34 | 25 |
| Grizzly | | 2 | 43 | 22 |
| Beartooth | | 2 | | |
| Misery | | 2 | | |
| Panda | | 2 | 16 | 12 |
| | HK1 | 5 | 21 | 29 |
| | HK2 | 5 | 10 | 4 |
| | HK3 | 5 | 15 | 13 |
| Snap Lake | HK4 | 5 | 15 | 12 |
| | HK5 | 5 | 34 | 14 |
| | HK6 | 5 | 28 | 19 |
| | Xenolith | 2 | 16 | 5 |
| **Total** | | **44** | **284** | **174** |

# CHAPTER 3 RESULTS

## 3.1 Abundance and textures of apatite

As expected, the abundances and textures of groundmass apatite were highly variable among the selected kimberlite pipes. Apatite is abundant in the hypabyssal pipes (Leslie and Snap Lake), moderately abundant in Grizzly, present in Koala and Panda, and virtually absent in Misery and Beartooth. In this section, the differences in apatite habits and groundmass relationships are outlined in each kimberlite pipe, as summarized in Table 3.1.

### 3.1.1 Apatite from Ekati Mine Kimberlite Pipes

***Koala*** Apatite in Koala kimberlite occurs in a fine-grained silicate matrix together with phlogopite laths and large perovskite grains. Apatite grains are 50-80 μm in size and show two textures. The majority form subhedral prisms with smooth grain boundaries, in places with minor pitting or resorption; few grains show zoning in BSE imaging (Fig. 3.1a). The second, less common, texture of apatite in Koala consists of grains with irregularly-shaped edges mantled by monticellite (Fig. 3.1b). The monticellite grains enclosing apatite are subhedral or euhedral and in places display resorption along the edges. Apatite grains in this texture have patchy zoning with multiple pits and inclusions of other groundmass material, or of apatite rich in REEs. The abundant inclusions, small grain size and irregular shape of this second apatite type did not allow us to obtain quantitative analyses.

***Leslie*** Groundmass apatite is abundant in the samples from Leslie kimberlite. Euhedral prisms and laths of apatite commonly contain small monticellite inclusions (Fig. 3.1c, 3.1d). Apatite forms larger grains (30-40 μm) than in most other samples examined, though some smaller anhedral grains (5-10 μm) occur in the interstitial groundmass. Apatite is mostly evenly distributed, but in some places forms clusters. Zoning is not clear in BSE; however, pitting is present in some grains and is accompanied by discoloration surrounding the pit in BSE images. High concentration of inclusions and small grain size limited the ability to obtain quantitative analyses.

***Grizzly*** The Grizzly kimberlite has less abundant apatite than Leslie. Apatite size ranges from 5-30um. It forms anhedral grains sitting in the groundmass with oxide minerals, abundant silicate minerals and minimal carbonate minerals (Fig. 3.1e, 3.1f). Most grains are evenly distributed and have no zoning and minimal resorption. Small (5-10 μm)

hexagonal grains (oriented perpendicular to the c-axis) display concentric zoning and significant resorption around the edges (Fig 3.1f). Quantitative analyses were obtained for core and rim of zoned apatite grains where grain size permitted.

***Panda*** Apatite is abundant in samples from Panda kimberlite. Most grains are subhedral, 10-20 μm in size, with no inclusions, pitting, zoning (in BSE images) or resorption (Figs. 3.1g, 3.1h).

***Misery and Beartooth*** Groundmass apatite was found to be virtually absent in Misery and Beartooth kimberlite pipes. In Misery, a cluster of apatite laths too small (1-5 μm) for analysis was located along a fracture. In one of the Beartooth samples, two clusters of apatite were found in association with a cluster of carbonate grains. The apatite crystals were very small (<5 μm), rich in light rare earth elements (LREEs; from EDX), and appear as very bright spots in BSE images (Fig. 3.1i).

### 3.1.2 Perovskite

Perovskite is noted as being ubiquitous in the selected Ekati kimberlite pipes (Nowicki et al. 2008). Since perovskite can incorporate REEs, high field strength elements (HFSEs) and may affect partitioning of these elements into apatite, it is important to know the relative timing of apatite crystallization relative to perovskite. In this study, perovskite was observed to be most abundant in Grizzly and Leslie, with very low abundance in Koala and Panda. These observations are consistent with conclusions by Nowicki et al. (2004) who suggested that the transition from hypabyssal kimberlite (Grizzly and Leslie) to primary volcaniclastic kimberlite (VK; Koala and Panda) is accompanied by a loss of groundmass phases spinel and perovskite.

In Grizzly, perovskite is 10-30 μm, euhedral, with complex zoning. Apatite grains are discrete, with rounded grain boundaries, no inclusions and little or no zoning. Though the two are not observed in a direct relationship to each other, perovskite could be an earlier phase based on grain shape. In Leslie, perovskite is more abundant than in Koala and Panda, but less abundant than in Grizzly. Grains are smaller (10-20um) and more poorly formed (subhedral) than apatite in the groundmass and some are zoned. Apatite in Leslie regularly includes small grains of early monticellite and, in places, an oxide phase. The included oxide grains are too small to adequately distinguish perovskite or spinel. An early

perovskite phase could have overlapped with apatite crystallization, but most perovskite crystallization may have been later than apatite growth because of the euhedral shape of apatite relative to small anhedral perovskite grains.

Perovskite grains in Panda and Koala are 5-40 μm, euhedral and cubic, with no evident zoning. Apatite crystals are subhedral and discrete from perovskite grains. Additionally, it may be difficult to accurately discern the crystallization sequence because of resedimentation of kimberlite material in Panda.

Given the difficulty in definitively establishing relative timing of crystallization for apatite and perovskite in all bodies, the presence of perovskite during apatite crystallization is considered in all melt models for the Ekati kimberlites.

### 3.1.3 Apatite from Snap Lake kimberlite dyke

Apatite is very abundant in the Snap Lake kimberlite; however, it shows very different textures in the fresher zones (HK1,-2,-5) and in the more altered zones (HK3,-4,-6). HK1, HK2 and HK5 contain 3-10 % poikilitic clusters of radially oriented acicular and columnar apatite crystals (Fulop et al. 2017), called, in this study, apatite Type 1 (Figs. 3.2a, 3.2b). These abundant apatite clusters (up to 100 μm in size) are distributed throughout the groundmass (Fig. 3.2b) and contain inclusions of olivine microphenocrysts altered to serpentine. Commonly the apatite crystals concentrate in areas immediately surrounding macrocrysts.

Apatite grains are evenly distributed within each of HK1 and HK2, although they are less abundant in HK2. The grain clusters are much smaller in HK2 than the large acicular groupings found in HK1. Apatite crystals are unevenly distributed in HK5. Abundant apatite is found in HK5 samples with large phlogopite microphenocryst laths, and occurs as radial clusters. HK5 samples without phlogopite laths have fewer apatite grains in smaller groupings, similar to grains found in HK2.

Another, less common, variety of apatite in these lithofacies, Type 2, is confined to carbonate veins that fill the fractures in olivine macrocrysts (Figs. 3.2c, 3.2d). Type 2 apatite forms subhedral grains (up to 100 μm) enclosed in these olivine-hosted carbonate veins in the same samples where apatite Type 1 is observed in the groundmass.

Apatite is less common in the more altered facies, HK3, HK4 and HK6. It occurs as euhedral to subhedral equant prismatic and hexagonal grains in the groundmass (Type 3; Figs. 3.2e, 3.2f). Type 3 apatite commonly has small inclusions or fractures and its size varies from 3-4 μm to 50-100 μm; largest grains occur in the samples with abundant groundmass carbonate (e.g. 2125, 3211). The Type 3 apatite grains found sparingly in HK5 are subhedral, commonly have inclusions, and can be clearly distinguished from groundmass apatite Type 1 by their small size and non-poikilitic texture. Apatite Type 3 grains are most abundant in HK6, and commonly are a major component of the groundmass in this zone.

One sample from the most altered zone (#4611) contains rounded subhedral prisms of apatite (here called Type 4) with size up to 500 μm (avg. 200 μm; Fig. 3.2g,h,i). This apatite forms abundant grains in a vein of hydrous silicate, oxide and carbonate minerals that cuts through kimberlite material (Fig. 3.2g) and produces a reaction zone in the adjacent kimberlite groundmass. These apatite grains are fractured. They show small pits of irregular shape and uneven distribution in the grain, possibly controlled by fracturing.

### 3.1.4 Apatite from crustal xenoliths

Crustal xenoliths found in several of the studied samples include apatite crystals inherited from the surrounding country rock (Fig. 3.3). Xenocrystic apatite grains are large (30-200 μm) and subhedral. These grains were analysed with WDX and LA-ICPMS for comparison with groundmass apatite grains. Representative compositions of xenocrystic apatite grains from Ekati (Leslie kimberlite) and Snap Lake (HK6) are given in Appendix C, and are plotted with all groundmass apatite compositions for comparison.

## 3.2 Cathodoluminescence study of apatite

Cathodoluminescence study of apatite from all kimberlite pipes was undertaken to reveal zoning not apparent with BSE imagery. As well, this method allows for the collection of spectra, indicating the wavelength of luminescence, which can vary for apatite with different amounts and proportions of activator (some LREEs, Mn) and quencher (e.g. Fe, As) elements. Complete collected CL spectra are provided in Appendix B. Correlation of all CL peaks to activators was based on Kempe and Gotze (2002) and Mitchell et al. (1997).

This endeavour was highly successful, revealing remarkable zoning in most of the samples examined (Fig. 3.4).

### 3.2.1 Apatite from Ekati Mine kimberlite pipes

CL of two apatite grains from Koala revealed some internal structure (Fig. B-1), though the grains were generally unremarkable under CL. Spectra were collected in two zones. The first spectrum of a dark grey zone, A, revealed peaks at 360nm ($Ce^{3+}$) and 800nm ($Sm^{3+}$). The second spectrum of a bright spot within the grain, B, revealed similar peaks of similar intensity to those in spectrum A. One peak is shifted from 360 nm closer to 400 nm. This is more likely an $Eu^{2+}$ peak.

All 4 apatite grains from Leslie studied in CL showed significant luminescence, and revealed complex patchy zoning (Fig 3.4b, Fig B-3) with at least 3 zones in the larger grains. The centres of the grains luminesce less brightly than the rims of the grains. Collected spectra of all three zones reveal significant peaks in the 350 nm and 760 nm regions, likely corresponding to $Ce^{3+}$ and $Dy^{3+}$, respectively. All three zones have a potential minor peak at 600 nm ($Sm^{3+}$). The intensity of all peaks is highest in zone C, which also shows increased $Ce^{3+}$ contribution relative to $Dy^{3+}$.

A single grain examined from Grizzly with CL showed minimal zoning. However, there was a very bright, thin rim surrounding the grain, possibly a late overgrowth on the grain edge (Fig. B-2). Two spectra were collected. Spectrum A, near the centre of the grain, has several peaks with activations by $Ce^{3+}$ (360 nm), $Dy^{3+}$ (480 nm, 570 nm, 760 nm), $Tb^{3+}$ (550 nm) and $Sm^{3+}$ (600 nm, 650 nm, 710 nm). The second spectrum has similar peaks, with slightly lower intensity.

Apatite grains from Panda showed complex oscillatory zoning in CL (Fig. 3.4a), with consistent very fine darker and lighter bands. Due to the small size of the zones, <1 μm, no spectra were collected on these grains.

### 3.2.2 Apatite from Snap Lake kimberlite

None of the Snap Lake apatite grains showed zoning in BSE images; however, CL study revealed complex zoning, especially in Types 1, 2 and 3. Type 1 apatite from Snap lake shows marked stepped zoning under CL (Fig. 3.4c, Fig. B-4). The grain zoning shows a striped pattern in some areas and rounded features in others. The darker zones appear to

represent the cores of the grains, with brighter zones occupying the outer edges. The pattern of stripes and circular features could be expressions of different grain orientations. Where the grain is cut parallel to the c-axis, the zoned grains appear as rods under CL. Grains cut perpendicular to the c-axis show a pseudo-hexagonal profile with the dark core, and brighter rim. These two patterns are clustered as densely pack grains culminating in the irregular, in some cases radial interstitial pattern displayed by the Type 1 apatite texture of Snap Lake. Spectra collected in the dark (A) and lighter (B) zones of apatite Type 1 reveal similar activators for luminescence: $Ce^{3+}$ (360 nm) and $Dy^{3+}$ (760 nm), with lower intensity in spectrum B.

Type 2 grains, possibly cogenetic with Type 1 grains, show a similar zoning pattern in CL to the Type 1 texture (Fig 3.4d, Fig. B-5). The euhedral grains display a dark core, with a slightly brighter rim. Two notable differences exist between the two apatite textures. The type 2 apatite rims appear to be less bright than the rims of Type 1 apatite grains. As well, a third generation of apatite surrounding the edges of Type 2 apatite grains. This third zone seems to be an overgrowth, and is discontinuous around the grain edge. Spectra from Type 2 apatite are very much like those from Type 1 apatite. Activators $Ce^{3+}$ (360 nm) and $Dy^{3+}$ (760 nm) are accompanied by a small peak at 600 nm, indicating $Sm^{3+}$ activation. In Type 2 apatite, the difference in intensity between core and rim is less pronounced than in Type 1; however, $Dy^{3+}$ is a more significant contributor to luminescence.

The third type of Snap Lake apatite, euhedral groundmass apatite, shows complex zoning in CL (Fig 3.4f, Fig. B-6). The dark core is mantled by a brighter oscillatory rim. The very outer edge of the apatite grain shows an atoll structure with a resorbed zone consisting of small oxides and a thin outermost rim of apatite. Two spectra were gathered, one in the dark core (A), and one in a lighter concentric rim (B). The two spectra have significant $Dy^{3+}$ activation, with minor peaks of $Ce^{3+}$ (360 nm), $Eu^{2+}$ (400 nm) and $Sm^{3+}$ (600 nm, 650 nm). The rim spectrum has a higher intensity, the $Ce^{3+}$ peak is more pronounced than in spectrum A.

Type 4 apatite from Snap Lake did not show significant zoning or internal structures in CL. On the largest grain, some small irregular zones were seen near the previously mentioned irregular dissolution pits (Fig. B-7). These zones were luminescing much brighter than the

surrounding grain, or any other grains of this type. Three spectra were collected on the large grain. Spectrum A, collected near the rim in a slightly brighter zone, shows a major peak at 565 nm, with intensity counts above 5000. This corresponds to luminescence activation by $Mn^{2+}$, which, when present, overlaps several other peaks in the vicinity, such as $Dy^{3+}$ and $Sm^{3+}$. Smaller peaks at regular intensities (≤1500 counts) are seen for $Ce^{3+}$ (360 nm), $Dy^{3+}$ (480 nm, 760 nm) and $Sm^{3+}$ (600 nm). Spectra B and C show more regular intensities, without the major $Mn^{2+}$ peak. There is significant activation by $Ce^{3+}$ (360 nm), $Dy^{3+}$ (480 nm, 570 nm, 760 nm), $Tb^{3+}$ (550 nm) and $Sm^{3+}$ (600 nm, 650 nm, 710 nm). Spectrum B, in the irregular bright zones shows more activation by LREEs and $Dy^{3+}$, and less by $Tb^{3+}$. Spectrum C has lower activation by the LREEs and $Dy^{3+}$, and more by $Tb^{3+}$.

### 3.3 Composition of apatite

Complete quantitative analyses from this study are provided in Appendix C. Average compositions of grains from the selected samples are given in Tables 3.2 and 3.3. Characteristics as mentioned in the text are outlined in Figs 3.5-3.9.

#### 3.3.1 Apatite from Ekati Mine kimberlite pipes

Concentration of major and minor elements including halogens (F, Cl) reveal significant differences in apatite composition from different kimberlite pipes (Table 3.2, Fig 3.6). Most of the studied apatite in Ekati kimberlite is fluorapatite (>0.5 apfu F) and has almost no Cl (Fig 3.5a). Panda is the only kimberlite with hydroxyapatite, up to 0.66 apfu OH (calculated assuming 1 total anion in the halogen site). Leslie and a group of Grizzly apatite grains have 0.52-0.75 apfu F, whereas all Koala, the rest of Grizzly and apatite from crustal xenoliths have >0.78 apfu F (Fig 3.5a). Also, apatite grains with the highest F concentration show increase in Cl (max 0.05 apfu). Thus, based on the halogen site-occupancy, apatite can be divided into three groups: hydroxyapatite (Panda), fluor-hydroxyapatite (Leslie and some Grizzly samples), and fluorapatite (Koala, the rest of Grizzly grains and all crustal xenocrysts).

Concentration of Sr and LREE (Σ La, Ce, Pr, Nd) in apatite, obtained by EMP analysis, also vary between the kimberlite pipes. Both Sr and LREE are low in apatite from Koala and crustal xenoliths (less than 0.02 apfu Sr and 0.03 apfu LREEs) and are highest in apatite grains from Leslie, where they reach up to 0.2 apfu Sr and 0.1 apfu LREEs (Fig 3.6a).

Grizzly apatite grains, again, form two compositional groups: apatite with higher F plot together with Koala in low Sr and LREE field, whereas apatite crystals with lower F form a trend towards the high Sr and LREE field of Leslie apatite grains (Fig 3.6c). Panda apatite grains have similarly high LREE to the Leslie apatite, but noticeably lower Sr (0.05 apfu compared to avg. 0.14 apfu in Leslie; Fig 3.6a).

Core and rim analyses were made, where grain size was large enough, to examine changes in apatite composition with growth. Representative core-rim pairs are given in Appendix C and analyses are plotted in Fig. 3.7. Except for Grizzly, all studied apatite from kimberlite samples have the same composition of core and rim, plotting relatively close in terms of Sr, LREE and F. Leslie rims are slightly depleted in Sr relative to the cores. In Grizzly, the rims plot close to apatite from Leslie, whereas the cores plot close to apatite grains from Koala.

Trace element concentrations determined from LA-ICPMS are plotted in Fig 3.8, normalized to Cl-chondritic values from McDonough and Sun (1995). To discriminate kimberlitic apatite from inherited crustal apatite xenocrysts, 3 apatite grains were analysed from xenoliths found in Leslie kimberlite and plotted their average for comparison in Fig. 3.8. REE plots (Fig. 3.8a-d) show flat REE patterns (low $[Ce/Yb]_{CN}$) and marked negative Eu anomaly of xenocrystic apatite (from Leslie) which corresponds to apatite typical of granitoid derivation (Belousova et al. 2002). Groundmass apatite grains from Koala and most grains from Grizzly show a flat REE pattern (low $[Ce/Yb]_{CN}$), with slight enrichment in light and heavy REEs relative to the xenocrystic reference, as well as a smaller Eu anomaly. Contrastingly, Leslie, Panda and two grains of Grizzly groundmass apatite have a steep negative REE slope, with no Eu anomaly. While the concentration of LREE is similar in Panda and Leslie apatite grains, middle rare earth elements (MREEs) and heavy rare earth elements (HREE), particularly, are more enriched in Panda.

Spider diagrams (Fig 3.8e-h) reveal distinct differences, particularly in Sr, Ba, Th/U and Y. Apatite grains from Leslie and Panda have the most enrichment in Sr, Ba and Th, and depletion in Y compared to xenocrystic apatite and the other compositional group formed by Koala and majority of Grizzly grains. Concentrations of Pb and HFSE's (Nb, Zr) are varied, but not distinctly different in either compositional group. The exception is Koala,

where apatite grains consistently show depletion in Nb relative to apatite crystals from other kimberlite samples, and xenocrystic apatite. This behaviour is mirrored in some analyses from Grizzly. Particularly interesting is the Th/U ratio in apatite grains from different kimberlite samples. Apatite from Koala, Grizzly and xenocrystic grains have Th<U, while in Panda, Leslie and two outliers from Grizzly, Th>U.

Overall, major and trace element analyses of apatite grains from the studied pipes reveals two distinct compositional groups: (1) Leslie, Panda and select grains from Grizzly (two highlighted in red on Grizzly trace element plots), and (2) Koala, majority of Grizzly grains and xenocrystic apatite crystals.

### 3.3.2 Apatite from Snap Lake kimberlite

All apatite varieties from Snap Lake are fluorapatite with negligible concentrations of Cl (Table 3.2, Fig 3.6). The representative xenocryst sample and apatite of Type 4 are almost pure fluorapatite end-member (>0.95 apfu F; Fig 3.5b). Types 1 and 2 apatite have similar composition (0.5-0.7 apfu F). Type 3 apatite approaches the hydroxyapatite field (Fig 3.5b), with a range of 0.45-0.6 apfu F.

As shown in Fig. 3.6b, Types 1 and 2 have the highest Sr content (up to 0.13 apfu), which is similar to Sr content of apatite in Leslie, but much lower LREEs (Σ La, Ce, Pr, Nd; <0.03 apfu). Type 3 apatite, with the highest LREEs in Snap lake, has moderate Sr content, similar to the composition of apatite from Panda, with slightly lower LREEs than Panda. Type 4 and apatite from crustal xenoliths has both low Sr and low LREEs, which is like samples from Koala and Ekati xenocrystic apatite.

Snap Lake apatite grains do not show significant variance in core-rim analyses (Fig. 3.7). Rims of Types 1, 2 and 3 grains are slightly enriched in F. Additionally, Type 3 rims are depleted in Sr relative to the cores.

The REE and spider diagrams of Snap Lake apatite types, Fig 3.9a-d, with inherited crustal apatite plotted for comparison, show negative REE slopes for all samples (intermediate-high $[Ce/Yb]_{CN}$) with no Eu anomaly. The concentrations of trace elements between the different apatite types is generally similar, with Type 3 being slightly enriched in all REEs relative to the other types. Type 1 apatite forms two groups in the REE diagram. The group with lower REEs is from grains found in a single sample from HK5.

Spider diagrams (Fig 3.9e-h) show variations between different types and within individual apatite types, that are less pronounced than in the Ekati kimberlite pipes. All groundmass apatite in Snap Lake has similar enrichment of Sr, Ba and depletion of Y relative to the crustal xenocrysts, like Leslie and Panda apatite crystals. Large ion lithophile elements (LILEs) can be enriched or the same as in crustal xenocrysts. Type 3 apatite from Snap Lake has the highest concentration of HSFE's. Th and U concentrations are markedly different in the different apatite types. While the ratio of the two elements is variable within the types, Type 1 (and some of Type 2 apatite grains) are depleted in both elements relative to the xenocrystic reference. Some grains from Type 2 and apatite from Leslie have Th>>U.

### 3.4 Leslie Xenocryst

Three generations of apatite occur in a single xenocrystic grain from Leslie (Fig 3.10), where the fractures in the original crustal apatite are healed with a later apatite, and then overgrown by a newly formed apatite rim. This grain could be extremely useful for tracking several generations of apatite growth during kimberlite crystallization, as well as changes in composition. For this reason, a track-analysis of the grain was performed through the different growth sections with seven spots of interest. These spots were measured for quantitative composition with both WDS and LA-ICPMS. A full complement of the analyses is provided in Appendix C, CL data and spectra for this grain are provided in Appendix B.

Fig 3.10 shows very similar composition of the fracture-infilling and rim apatite occurrences, with higher Sr, Ba, Th, HFSE's, LREEs and lower Y, HREEs than the host crustal apatite. Major and trace element compositions for the analysed spots are given in Table 4. CL of this grain and healed fractures (Fig. B-8) show activation by $Ce^{3+}$, $Dy^{3+}$ and minor peaks of activation by $Sm^{3+}$.

### 3.5 Apatite-biotite thermometry

WDX analyses of xenocrystic apatite-biotite pairs carried in the kimberlite magma were collected for the halogens and major elements, with a presumption that the halogen distribution would be reset between the two minerals during residence time in the kimberlite magma. Data was collected from apatite and biotite grains located in xenocrysts

within the kimberlite magma. Apatite commonly occurs as inclusions within the xenocrystic biotite, as shown in Fig 3.11, and both were analysed for interchange of F and OH.

An apatite-biotite geothermometer using F partitioning was initially presented by Stormer and Carmichael (1971), and was later revised by Zhu and Sverjensky (1992). Here, this geothermometer is applied to try and obtain some data for the temperatures of erupting kimberlite melts. The thermometer comprises a set of three equations based on the thermodynamic reaction:

$$0.5KMg_3[AlSi_3O_{10}](F)_2 + Ca_5[PO_4]_3OH = 0.5KMg_3[AlSi_3O_{10}](OH)_2 + Ca_5[PO_4]_3F \quad (4)$$

representing the exchange between fluorphlogopite, hydroxyapatite, phlogopite and fluorapatite. First, the equilibrium constant for this exchange is defined as:

$$K_{D,F}^{Ap/Bt} = \left(\frac{X_F}{X_{OH}}\right)^{Ap} \Big/ \left(\frac{X_F}{X_{OH}}\right)^{Bt} \quad (5)$$

Second, to account for the effects of octahedral-site substitution ($Fe^{2+}$-Mg) on F-OH partitioning in biotite, they define a mole fraction value $X_{Fe}$ as:

$$X_{Fe} = \frac{Fe + Al^{VI}}{Fe + Mg + Al^{VI}} \quad (6)$$

where octahedral Al ($Al^{VI}$) has the same influence as $Fe^{2+}$ on the octahedral site size. This accounts for the effects of Mg-$Fe^{2+}$ substitution in biotite on the thermometer. Finally, using thermodynamic constants established by Zhu and Sverjensky (1991) for the above mineral endmembers, the geothermometer is given as:

$$T(°C) = \frac{8852 - 0.024P(bars) + 5000X_{Fe}}{1.987lnK_{D,F}^{Ap/Bt} + 3.3666} - 273.15 \quad (7)$$

Results from the geothermometer for the selected kimberlite bodies in this study are presented in Table 3.5. Pressure ($P$) was assumed at 1 bar for all calculations. Analytical error from F and Cl analyses was propagated into two standard deviations of $\ln K_{D,F}$ using the equation:

$$\sigma^2_{\ln K_{D,F}^{Ap/Bt}} = \left(\frac{\sigma_{X_F^{Bt}}(1-X_{Cl})}{X_F(1-X_F-X_{Cl})}\right)^2_{Bt} + \left(\frac{\sigma_{X_{Cl}^{Bt}}}{(1-X_F-X_{Cl})}\right)^2_{Bt} + \left(\frac{\sigma_{X_F^{Ap}}(1-X_{Cl})}{X_F(1-X_F-X_{Cl})}\right)^2_{Ap} + \left(\frac{\sigma_{X_{Cl}^{Ap}}}{X_F(1-X_F-X_{Cl})}\right)^2_{Ap} \quad (8)$$

as presented in (Zhu and Sverjensky 1992), where σ is one standard deviation. Error in $\ln K_{D,F}$ drastically increase towards the high F endmember of apatite, and very slightly increases towards higher F contents in biotite (Fig. 3.12).

The results of the geothermometer indicate temperatures of 300-500 °C for the Ekati kimberlite samples and 400-480 °C for the Snap Lake kimberlite (Table 3.5). All the calculated temperatures from biotite-apatite pairs in the studied kimberlite samples are significantly below what is expected for kimberlite magmas, including those calculated by Zhu and Sverjensky (1992) for the Bellsbank kimberlite (986 C; Hervig and Smith 1981). This result suggests that the residence time in the magma of these xenoliths was not sufficient to reset the distribution of halogens between these two phases. This is the case for pairs from both volcaniclastic and hypabyssal kimberlite facies. In addition, it is possible that the source rock for these xenoliths underwent some low-T hydrothermal alteration, resulting in the low temperatures calculated here.

Table 3.1 Summary of apatite occurrence in the selected kimberlite samples

| **Kimberlite** | **Abundance** | **Size (µm)** | **Habit** | **Zoning** |
|---|---|---|---|---|
| Leslie (HK) | abundant | 5-60 | euhedral | patchy |
| Grizzly (HK) | intermediate | < 10 | subhedral | diffuse |
| Panda (KPK, RVK) | intermediate | 20-100 | subhedral | oscillatory |
| Beartooth (RVK) | v. low | | | |
| Misery (KPK) | v. low | | | |
| Koala (KPK) | intermediate | 10-150 | anhedral | diffuse |
| Snap Lake (HK1,-2,-5) | 3-10% modal | 10-100 | acicular (1), vein hosted (2) | diffuse |
| Snap Lake (HK3,-4,-6) | <3% modal | 20-50 | euhedral (3) | oscillatory |

Table 3.2 Representative composition of apatite from Ekati and Snap Lake kimberlite pipes.

| | Koala | | Leslie | | Grizzly | | Panda | | SL Type 1 | | SL Type 2 | | SL Type 3 | |
|---|---|---|---|---|---|---|---|---|---|---|---|---|---|---|
| | n= 12 | | n= 22 | | n= 20 | | n= 9 | | n= 18 | | n= 26 | | n= 42 | |
| | Mean | 1σ | Mean | 1σ | Mean | 1σ | Mean | 1σ | Mean | 1σ | Mean | 1σ | Mean | 1σ |
| *Major elements wt% (WDS)* | | | | | | | | | | | | | | |
| **F** | 3.64 | *0.41* | 2.13 | *0.25* | 3.28 | *0.44* | 1.56 | *0.08* | 2.35 | *0.17* | 2.47 | *0.15* | 2.03 | *0.75* |
| **$Na_2O$** | 0.08 | *0.05* | 0.15 | *0.10* | 0.11 | *0.13* | 0.17 | *0.04* | 0.13 | *0.12* | 0.14 | *0.07* | 0.66 | *0.42* |
| **CaO** | 55.77 | *0.61* | 50.58 | *1.00* | 55.25 | *1.55* | 52.96 | *0.68* | 53.95 | *0.57* | 53.27 | *0.90* | 52.65 | *1.20* |
| **$P_2O_5$** | 41.37 | *0.39* | 38.83 | *0.92* | 39.76 | *1.64* | 35.22 | *0.54* | 40.00 | *0.56* | 38.92 | *0.88* | 36.22 | *1.72* |
| **FeO** | 0.15 | *0.08* | 0.21 | *0.06* | 0.25 | *0.14* | 0.24 | *0.05* | 0.17 | *0.14* | 0.15 | *0.08* | 0.17 | *0.08* |
| **$SiO_2$** | 0.05 | *0.06* | 1.00 | *0.45* | 0.39 | *0.80* | 2.72 | *0.14* | 0.39 | *0.29* | 0.81 | *0.58* | 1.94 | *0.38* |
| **BaO** | 0.00 | *0.00* | 0.00 | *0.00* | 0.01 | *0.02* | 0.00 | *0.00* | 0.03 | *0.06* | 0.03 | *0.03* | 0.00 | *0.00* |
| **Cl** | 0.05 | *0.03* | 0.01 | *0.01* | 0.10 | *0.13* | 0.03 | *0.01* | 0.00 | *0.01* | 0.01 | *0.01* | 0.04 | *0.05* |
| **$Ce_2O_3$** | 0.07 | *0.09* | 1.25 | *0.17* | 0.12 | *0.21* | 1.07 | *0.14* | 0.11 | *0.11* | 0.15 | *0.12* | 0.53 | *0.17* |
| **$La_2O_3$** | 0.03 | *0.04* | 0.91 | *0.13* | 0.09 | *0.17* | 0.84 | *0.11* | 0.08 | *0.09* | 0.12 | *0.12* | 0.35 | *0.12* |
| **SrO** | 0.00 | *0.01* | 2.82 | *0.42* | 0.16 | *0.42* | 0.67 | *0.09* | 2.03 | *0.30* | 1.96 | *0.23* | 0.87 | *0.12* |
| **$Pr_2O_3$** | 0.05 | *0.07* | 0.09 | *0.08* | 0.04 | *0.06* | 0.09 | *0.09* | 0.04 | *0.04* | 0.04 | *0.04* | 0.07 | *0.08* |
| **$V_2O_3$** | 0.00 | *0.01* | 0.00 | *0.00* | 0.00 | *0.00* | 0.00 | *0.00* | 0.01 | *0.02* | 0.01 | *0.01* | 0.00 | *0.00* |
| **$K_2O$** | 0.06 | *0.03* | 0.05 | *0.02* | 0.07 | *0.04* | 0.07 | *0.04* | 0.03 | *0.01* | 0.04 | *0.02* | 0.09 | *0.05* |
| **$Nd_2O_3$** | 0.10 | *0.10* | 0.22 | *0.07* | 0.07 | *0.06* | 0.18 | *0.07* | 0.07 | *0.07* | 0.07 | *0.07* | 0.17 | *0.11* |
| **MnO** | 0.04 | *0.02* | 0.01 | *0.01* | 0.03 | *0.02* | 0.02 | *0.02* | 0.01 | *0.01* | 0.01 | *0.01* | 0.02 | *0.02* |
| **Total** | **99.91** | ***0.74*** | **97.36** | ***1.50*** | **98.34** | ***2.03*** | **95.18** | ***0.65*** | **98.43** | ***0.80*** | **97.15** | ***1.29*** | **94.94** | ***1.93*** |
| **X(Fap)** | 0.96 | *0.11* | 0.59 | *0.07* | 0.83 | *0.21* | 0.42 | *0.02* | 0.62 | *0.05* | 0.66 | *0.04* | 0.55 | *0.21* |
| **X(Cap)** | 0.01 | *0.00* | 0.00 | *0.00* | 0.01 | *0.02* | 0.00 | *0.00* | 0.00 | *0.00* | 0.00 | *0.00* | 0.01 | *0.01* |
| **X(Oap)** | 0.04 | *0.11* | 0.41 | *0.07* | 0.16 | *0.21* | 0.57 | *0.02* | 0.38 | *0.05* | 0.33 | *0.04* | 0.45 | *0.22* |

Table 3.3 Representative trace element composition of apatite from Ekati kimberlite pipes, l.o.d. limits of detection.

| | Koala | | | Leslie | | | Grizzly | | | Grizzly (kimberlitic) | | | Panda | | |
|---|---|---|---|---|---|---|---|---|---|---|---|---|---|---|---|
| | n= 12 | | | n= 22 | | | n= 18 | | | n= 2 | | | n= 9 | | |
| | Mean | 1σ | l.o.d. | Mean | 1σ | l.o.d. | Mean | 1σ | l.o.d. | Mean | 1σ | l.o.d. | Mean | 1σ | l.o.d. |
| *Trace elements ppm (LA-ICPMS)* | | | | | | | | | | | | | | | |
| **Na** | 406.1 | *243.4* | 26.454 | 745.9 | *498.9* | 30.007 | 406.6 | *327.8* | 25.996 | 2918.1 | *1055.0* | 65.894 | 1300.2 | *939.9* | 54.163 |
| **Si** | 3722.8 | *7229.7* | 778.724 | 14421.2 | *19019.8* | 890.225 | 8926.9 | *18525.3* | 824.511 | 33247.1 | *26900.7* | 2109.143 | 16794.5 | *5806.8* | 1863.707 |
| **V** | 11.4 | *5.6* | 0.401 | 214.1 | *26.7* | 0.489 | 48.0 | *46.8* | 0.401 | 349.5 | *34.4* | 0.968 | 309.7 | *78.6* | 0.954 |
| **Fe** | 758.5 | *2175.0* | 18.716 | 2402.6 | *3319.8* | 22.852 | 1966.4 | *5154.9* | 21.362 | 12948.7 | *14370.1* | 56.842 | 5232.3 | *8607.4* | 47.808 |
| **As** | 39.0 | *41.5* | 3.105 | 18.4 | *3.2* | 3.766 | 45.4 | *37.7* | 3.260 | 12.8 | *4.4* | 7.924 | 18.4 | *3.1* | 8.781 |
| **Rb** | 5.2 | *8.4* | 0.524 | 2.8 | *2.9* | 0.637 | 17.3 | *35.8* | 0.549 | 66.1 | *67.9* | 1.325 | 10.5 | *8.1* | 1.299 |
| **Sr** | 406.7 | *50.6* | 0.130 | 24007.0 | *3253.4* | 0.171 | 1672.3 | *2033.5* | 0.147 | 13030.3 | *282.9* | 0.406 | 6516.4 | *680.2* | 0.440 |
| **Y** | 442.7 | *201.3* | 0.052 | 9.3 | *3.7* | 0.101 | 866.8 | *532.3* | 0.093 | 14.4 | *1.5* | 0.281 | 33.6 | *33.5* | 0.271 |
| **Zr** | 1.4 | *2.7* | 0.121 | 3.9 | *3.5* | 0.190 | 3.7 | *8.6* | 0.185 | 17.9 | *17.5* | 0.284 | 17.0 | *4.3* | 0.625 |
| **Nb** | 0.6 | *1.4* | 0.059 | 18.8 | *25.7* | 0.101 | 18.3 | *28.7* | 0.090 | 100.5 | *105.5* | 0.215 | 62.1 | *87.9* | 0.329 |
| **Cs** | n.d. | *n.d.* | 0.277 | n.d. | *n.d.* | 0.318 | n.d. | *n.d.* | 0.279 | n.d. | *n.d.* | 0.657 | n.d. | *n.d.* | 0.667 |
| **Ba** | 14.2 | *36.7* | 0.492 | 890.0 | *270.7* | 0.760 | 139.3 | *182.4* | 0.658 | 2126.3 | *548.5* | 1.921 | 1961.8 | *3704.0* | 1.876 |
| **La** | 211.0 | *251.7* | 0.046 | 7188.8 | *694.2* | 0.079 | 532.6 | *684.4* | 0.061 | 4554.2 | *18.2* | 0.146 | 6315.3 | *1668.0* | 0.256 |
| **Ce** | 711.0 | *781.8* | 0.045 | 9634.9 | *856.3* | 0.082 | 972.5 | *934.7* | 0.065 | 6017.6 | *519.3* | 0.206 | 8600.6 | *2400.2* | 0.219 |
| **Pr** | 125.2 | *109.2* | 0.058 | 862.7 | *86.4* | 0.067 | 133.3 | *97.1* | 0.056 | 549.8 | *94.4* | 0.152 | 704.3 | *182.9* | 0.176 |
| **Nd** | 694.0 | *445.6* | 0.236 | 2224.8 | *267.2* | 0.410 | 655.5 | *366.0* | 0.356 | 1517.0 | *255.1* | 0.942 | 1918.6 | *501.2* | 0.941 |
| **Sm** | 176.1 | *74.8* | 0.321 | 112.7 | *20.1* | 0.502 | 183.2 | *97.6* | 0.400 | 103.0 | *15.9* | 0.816 | 131.7 | *35.1* | 1.381 |
| **Eu** | 23.6 | *8.7* | 0.069 | 19.1 | *3.7* | 0.138 | 37.1 | *20.3* | 0.104 | 18.8 | *3.8* | 0.237 | 28.1 | *6.6* | 0.342 |
| **Gd** | 153.3 | *60.5* | 0.293 | 32.7 | *5.9* | 0.545 | 194.5 | *99.2* | 0.453 | 32.6 | *6.7* | 0.885 | 52.6 | *13.5* | 1.202 |
| **Yb** | 31.3 | *14.7* | 0.216 | 0.4 | *0.3* | 0.363 | 73.4 | *54.0* | 0.265 | n.d. | *n.d.* | 0.797 | 3.1 | *4.2* | 1.003 |
| **Lu** | 4.6 | *2.0* | 0.052 | 0.1 | *0.0* | 0.073 | 11.0 | *8.1* | 0.060 | n.d. | *n.d.* | 0.169 | 1.0 | *1.5* | 0.195 |
| **Ta** | 0.1 | *0.0* | 0.045 | 0.7 | *0.5* | 0.081 | 0.7 | *1.0* | 0.066 | 1.3 | *1.2* | 0.141 | 2.1 | *2.2* | 0.220 |
| **Pb** | 8.0 | *4.9* | 0.218 | 2.5 | *1.8* | 0.317 | 15.3 | *10.1* | 0.248 | 8.9 | *8.9* | 0.585 | 77.4 | *151.0* | 0.706 |
| **Th** | 16.8 | *15.8* | 0.062 | 158.9 | *33.1* | 0.101 | 62.3 | *63.2* | 0.068 | 227.6 | *51.3* | 0.192 | 99.7 | *24.0* | 0.265 |
| **U** | 26.0 | *11.3* | 0.051 | 0.7 | *0.6* | 0.082 | 42.4 | *30.2* | 0.068 | 4.1 | *4.2* | 0.148 | 15.1 | *2.9* | 0.211 |

Table 3.4 Representative trace element composition of apatite from Snap Lake kimberlite dyke, l.o.d. limits of detection.

| | Snap Lake Type 1 | | | Snap Lake Type 2 | | | Snap Lake Type 3 | | |
|---|---|---|---|---|---|---|---|---|---|
| | n= 18 | | | n= 26 | | | n= 42 | | |
| | Mean | *1σ* | l.o.d. | Mean | *1σ* | l.o.d. | Mean | *1σ* | l.o.d. |
| *Trace elements ppm (LA-ICPMS)* | | | | | | | | | |
| **Na** | 736.2 | *408.5* | 44.3 | 771.3 | *378.6* | 37.9 | 4184.4 | *2676.0* | 43.8 |
| **Si** | 20382.7 | *56036.1* | 1697.5 | 8596.4 | *9000.2* | 1408.0 | 33803.8 | *83747.2* | 1890.9 |
| **V** | 181.8 | *40.3* | 0.7 | 171.4 | *38.0* | 0.6 | 168.8 | *111.6* | 0.7 |
| **Fe** | 3193.7 | *8778.8* | 33.8 | 1180.9 | *1728.1* | 27.0 | 8397.1 | *25378.8* | 43.9 |
| **As** | 13.1 | *2.5* | 5.6 | 12.4 | *2.4* | 4.5 | 17.4 | *6.6* | 6.2 |
| **Rb** | n.d. | *n.d.* | 0.9 | 27.6 | *19.7* | 0.8 | 7.4 | *13.7* | 0.9 |
| **Sr** | 18347.3 | *2219.5* | 0.2 | 17160.2 | *2659.2* | 0.2 | 8149.8 | *758.7* | 0.2 |
| **Y** | 76.9 | *39.7* | 0.1 | 107.6 | *12.7* | 0.1 | 129.2 | *48.6* | 0.1 |
| **Zr** | 6.8 | *6.3* | 0.3 | 12.8 | *7.4* | 0.2 | 209.5 | *92.1* | 0.2 |
| **Nb** | 1.8 | *2.2* | 0.1 | 3.1 | *2.4* | 0.1 | 62.9 | *139.2* | 0.1 |
| **Cs** | n.d. | *n.d.* | 0.4 | 0.8 | *0.5* | 0.4 | 1.6 | *3.4* | 0.4 |
| **Ba** | 613.6 | *177.6* | 0.9 | 752.7 | *368.0* | 0.8 | 292.2 | *220.1* | 1.0 |
| **La** | 807.0 | *574.0* | 0.1 | 1109.1 | *609.8* | 0.1 | 3135.8 | *644.4* | 0.1 |
| **Ce** | 946.8 | *596.4* | 0.1 | 1488.9 | *601.1* | 0.1 | 4576.2 | *1011.4* | 0.1 |
| **Pr** | 93.4 | *54.6* | 0.1 | 155.1 | *50.8* | 0.1 | 434.5 | *103.1* | 0.1 |
| **Nd** | 341.3 | *188.5* | 0.5 | 569.5 | *155.8* | 0.4 | 1426.7 | *365.2* | 0.5 |
| **Sm** | 65.7 | *35.0* | 0.6 | 101.6 | *18.7* | 0.5 | 191.5 | *56.0* | 0.7 |
| **Eu** | 19.3 | *9.8* | 0.2 | 28.6 | *3.9* | 0.1 | 48.7 | *15.0* | 0.2 |
| **Gd** | 55.6 | *28.4* | 0.6 | 80.9 | *9.5* | 0.6 | 119.8 | *40.6* | 0.6 |
| **Yb** | 1.6 | *0.9* | 0.4 | 2.3 | *0.7* | 0.4 | 4.2 | *2.6* | 0.5 |
| **Lu** | 0.2 | *0.1* | 0.1 | 0.2 | *0.1* | 0.1 | 0.4 | *0.2* | 0.1 |
| **Ta** | 0.3 | *0.3* | 0.1 | 0.2 | *0.2* | 0.1 | 3.5 | *13.8* | 0.1 |
| **Pb** | 2.7 | *1.1* | 0.4 | 4.5 | *2.9* | 0.3 | 20.4 | *70.2* | 0.5 |
| **Th** | 3.8 | *3.6* | 0.1 | 48.4 | *66.1* | 0.1 | 62.0 | *58.4* | 0.1 |
| **U** | 2.0 | *1.2* | 0.1 | 3.2 | *0.9* | 0.1 | 19.2 | *14.0* | 0.1 |

Table 3.5 Apatite-biotite thermometry of xenoliths from kimberlite, thermometer from Zhu and Sverjensky (1992).

| | Biotite | | | | | | | Apatite | | | $K_{D,F}$ | $\ln K_{D,F}$ | $2\sigma_{\ln K(D,F)}$ | T °C | ± |
|---|---|---|---|---|---|---|---|---|---|---|---|---|---|---|---|
| | X(Fbi) | X(Cbi) | X(Obi) | Fe | Mg | $Al^{VI}$ | $X_{Fe}$ | X(Fap) | X(Cap) | X(Oap) | | | | | |
| **Koala** | 0.066 | 0.008 | 1.926 | 0.980 | 2.672 | 0.000 | 0.268 | 0.964 | 0.012 | 0.024 | 1163.58 | 7.06 | 5.37 | 313 | 577 |
| **Koala** | 0.069 | 0.006 | 1.925 | 0.953 | 2.646 | 0.000 | 0.265 | 0.823 | 0.075 | 0.101 | 226.18 | 5.42 | 0.27 | 447 | 27 |
| **Koala** | 0.072 | 0.006 | 1.923 | 0.947 | 2.648 | 0.000 | 0.263 | 0.915 | 0.007 | 0.078 | 314.02 | 5.75 | 0.52 | 414 | 48 |
| **Koala** | 0.015 | 0.002 | 1.983 | 0.934 | 3.240 | 0.000 | 0.224 | 0.836 | 0.003 | 0.160 | 700.35 | 6.55 | 0.13 | 335 | 9 |
| **Koala** | 0.052 | 0.002 | 1.945 | 1.142 | 3.142 | 0.000 | 0.267 | 0.896 | 0.001 | 0.103 | 323.85 | 5.78 | 0.31 | 413 | 28 |
| **Koala** | 0.092 | 0.002 | 1.906 | 0.994 | 2.777 | 0.000 | 0.264 | 0.908 | 0.005 | 0.087 | 217.17 | 5.38 | 0.42 | 450 | 43 |
| **Snap Lake HK6** | 0.108 | 0.006 | 1.887 | 1.109 | 2.716 | 0.000 | 0.290 | 0.911 | 0.000 | 0.089 | 178.81 | 5.19 | 0.41 | 480 | 45 |
| **Snap Lake HK6** | 0.095 | 0.004 | 1.901 | 1.422 | 1.852 | 0.000 | 0.434 | 0.944 | 0.003 | 0.053 | 353.27 | 5.87 | 1.12 | 461 | 111 |
| **Snap Lake HK6** | 0.115 | 0.003 | 1.882 | 1.413 | 1.767 | 0.000 | 0.444 | 0.973 | 0.002 | 0.025 | 639.71 | 6.46 | 5.13 | 410 | 710 |
| **Beartooth** | 0.019 | 0.002 | 1.979 | 0.717 | 2.371 | 0.000 | 0.232 | 0.907 | 0.008 | 0.085 | 1118.50 | 7.02 | 0.44 | 305 | 29 |
| **Beartooth** | 0.018 | 0.002 | 1.980 | 0.635 | 2.478 | 0.000 | 0.204 | 0.951 | 0.008 | 0.041 | 2589.72 | 7.86 | 1.85 | 247 | 105 |
| **Beartooth** | 0.022 | 0.001 | 1.977 | 0.742 | 2.320 | 0.000 | 0.242 | 0.907 | 0.013 | 0.081 | 988.21 | 6.90 | 0.48 | 316 | 33 |
| **Beartooth** | 0.027 | 0.004 | 1.969 | 0.900 | 2.085 | 0.000 | 0.302 | 0.803 | 0.010 | 0.187 | 306.63 | 5.73 | 0.09 | 430 | 9 |
| **Grizzly** | 0.068 | 0.010 | 1.922 | 0.976 | 2.642 | 0.000 | 0.270 | 0.943 | 0.004 | 0.053 | 505.58 | 6.23 | 1.14 | 375 | 95 |
| **Grizzly** | 0.051 | 0.008 | 1.941 | 1.015 | 2.486 | 0.000 | 0.290 | 0.857 | 0.003 | 0.139 | 233.55 | 5.45 | 0.17 | 452 | 17 |
| **Grizzly** | 0.064 | 0.007 | 1.930 | 1.026 | 2.550 | 0.000 | 0.287 | 0.779 | 0.006 | 0.216 | 109.73 | 4.70 | 0.07 | 537 | 9 |
| **Grizzly** | 0.040 | 0.015 | 1.945 | 0.946 | 2.583 | 0.000 | 0.268 | 0.778 | 0.004 | 0.218 | 174.00 | 5.16 | 0.07 | 475 | 8 |

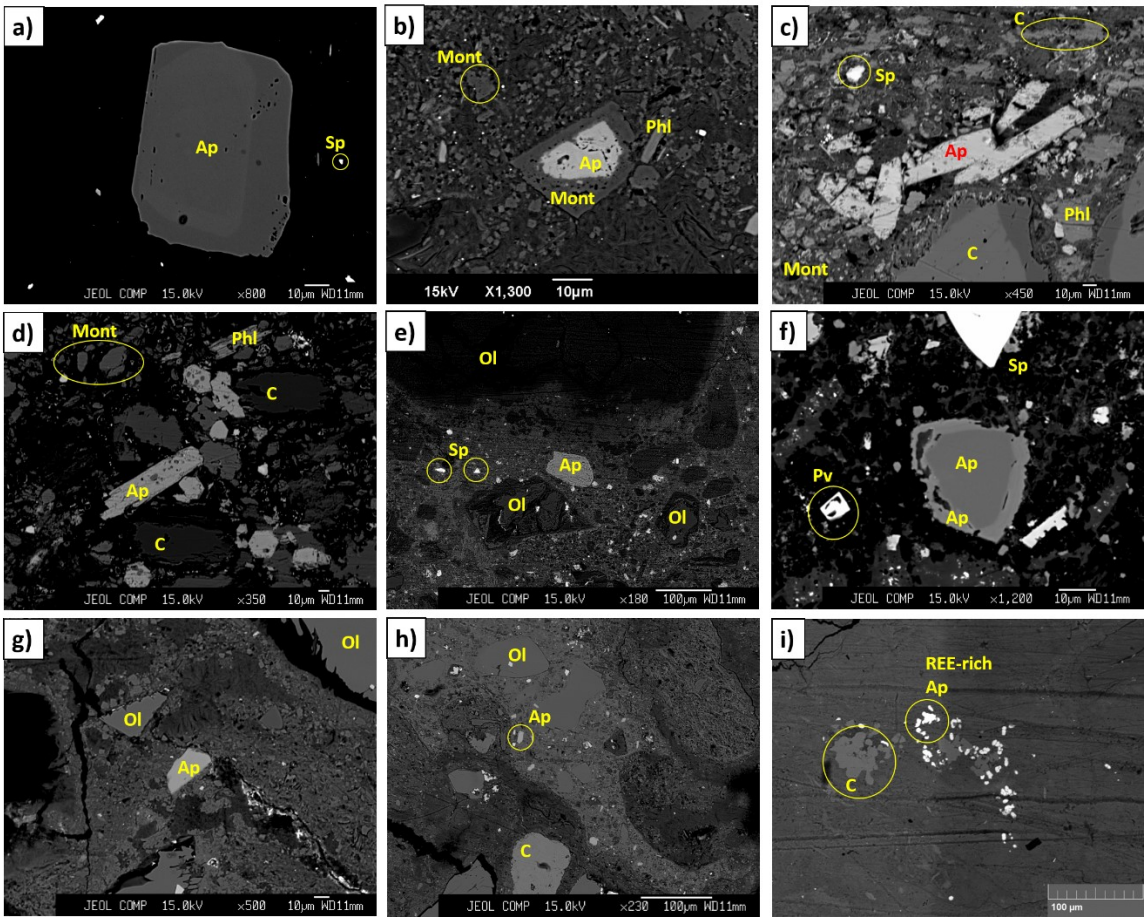


Figure 3.1 BSE images of apatite grains from Ekati kimberlite pipes, a,b) Koala, c,d) Leslie, e,f) Grizzly, g,h) Panda, and i) Beartooth. Ap – apatite, Sp – spinel, Mont – monticellite, Phl – phlogopite, C – carbonate, Ol – olivine, Pv – perovskite.

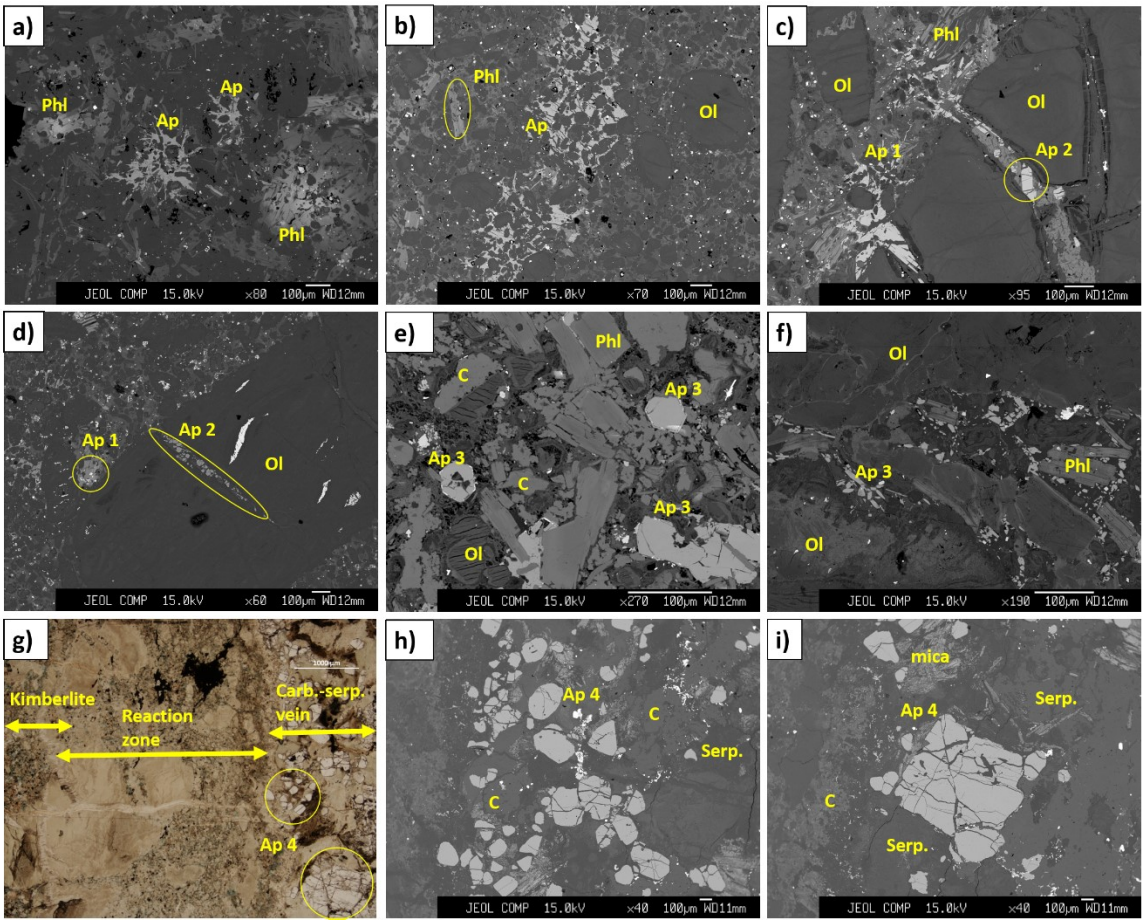


Figure 3.2 BSE images of apatite grains from Snap Lake, a) groundmass apatite Type 1 (HK5), b) groundmass apatite Type 1 (HK1), c) groundmass apatite Type 2 (HK2), d) groundmass apatite type 2 (HK1), e) groundmass apatite Type 3 (HK4), f) groundmass apatite Type 3 (HK6), g) plain-polarized transmitted light microscopy image of sample 4611 showing large vein with apatite Type 4, and h,i) BSE image of apatite Type 4 in carbonate-serpentine vein from sample 4611. Ap – apatite, Phl – phlogopite, Ol – olivine (completely serpentinized in Snap Lake), C – carbonate, Serp – serpentine.

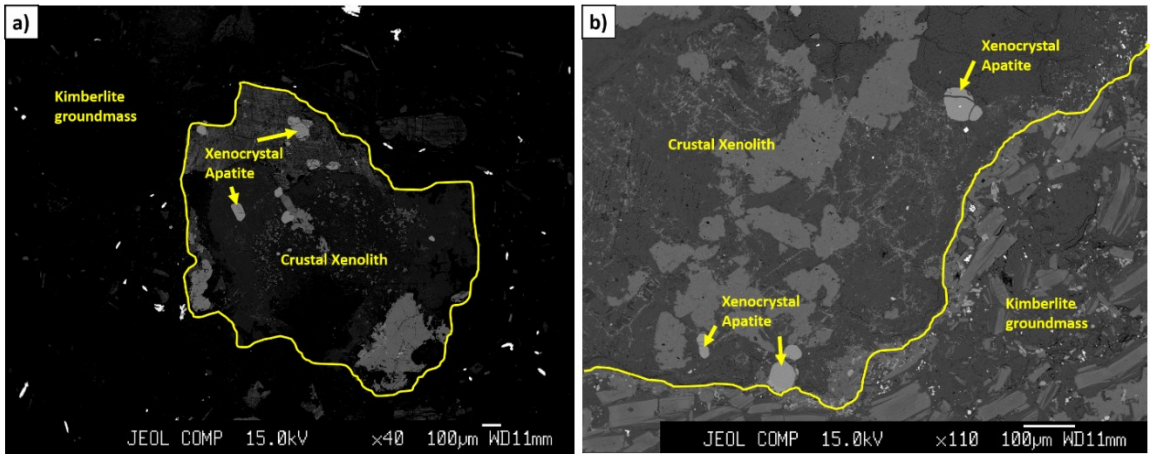


Figure 3.3 BSE images of apatite xenocrystic grains contained in crustal xenoliths from a) Koala, and b) Snap Lake.

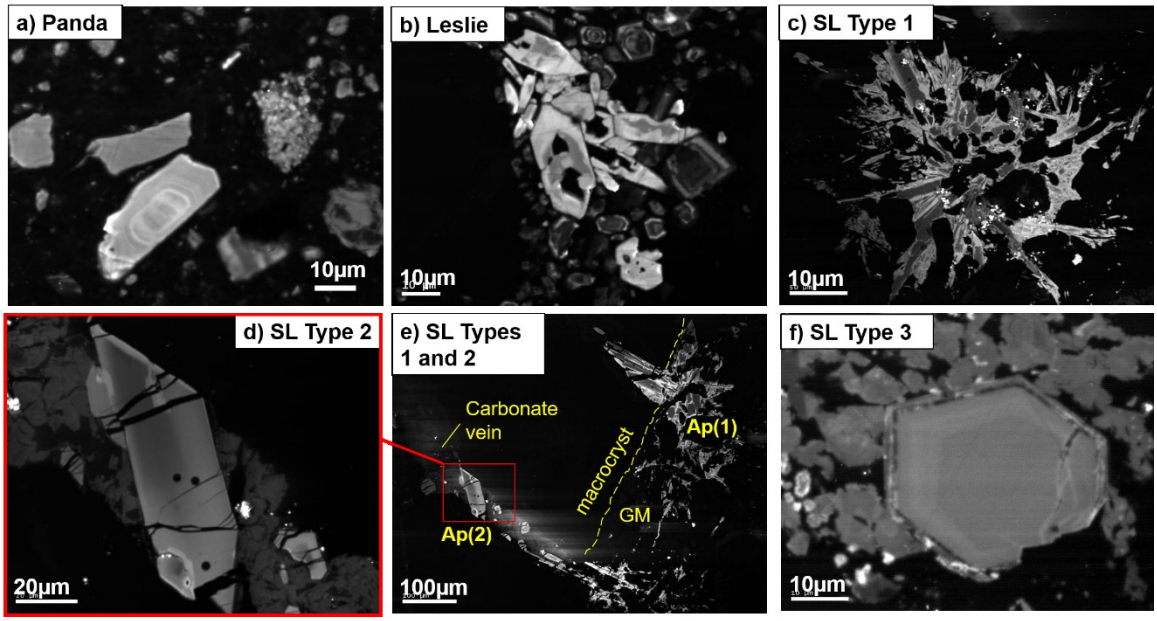


Figure 3.4 CL images of apatite grains from a) Panda, b) Leslie, c) Snap Lake Type 1 apatite, d) Snap Lake Type 2 apatite (blown up from e), e) Snap Lake Type 2 apatite sitting in a carbonate vein which cuts an olivine (serpentinized) macrocryst, and Type 1 apatite sitting in the kimberlite groundmass, f) Snap Lake Type 3 apatite. Complete CL spectra collected for the selected kimberlite samples provided in Appendix B.

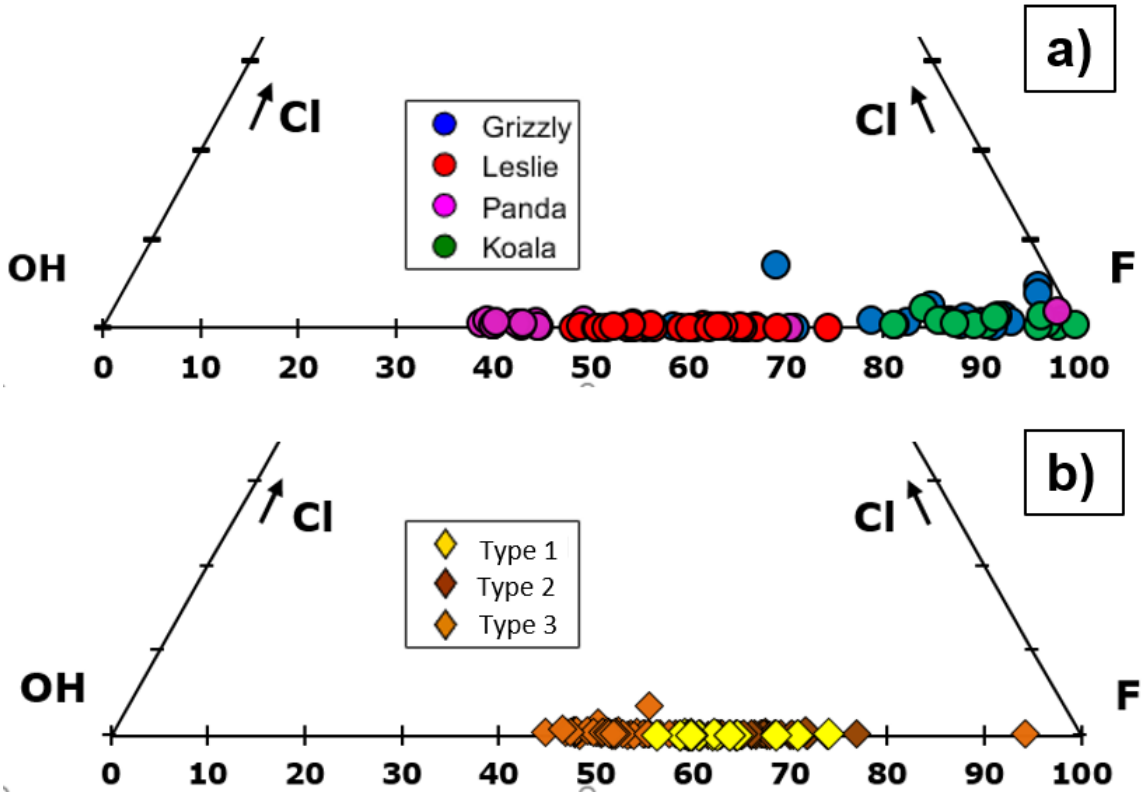


Figure 3.5 Halogen site occupancy in apatite grains from a) Ekati kimberlite pipes, b) Snap Lake kimberlite.

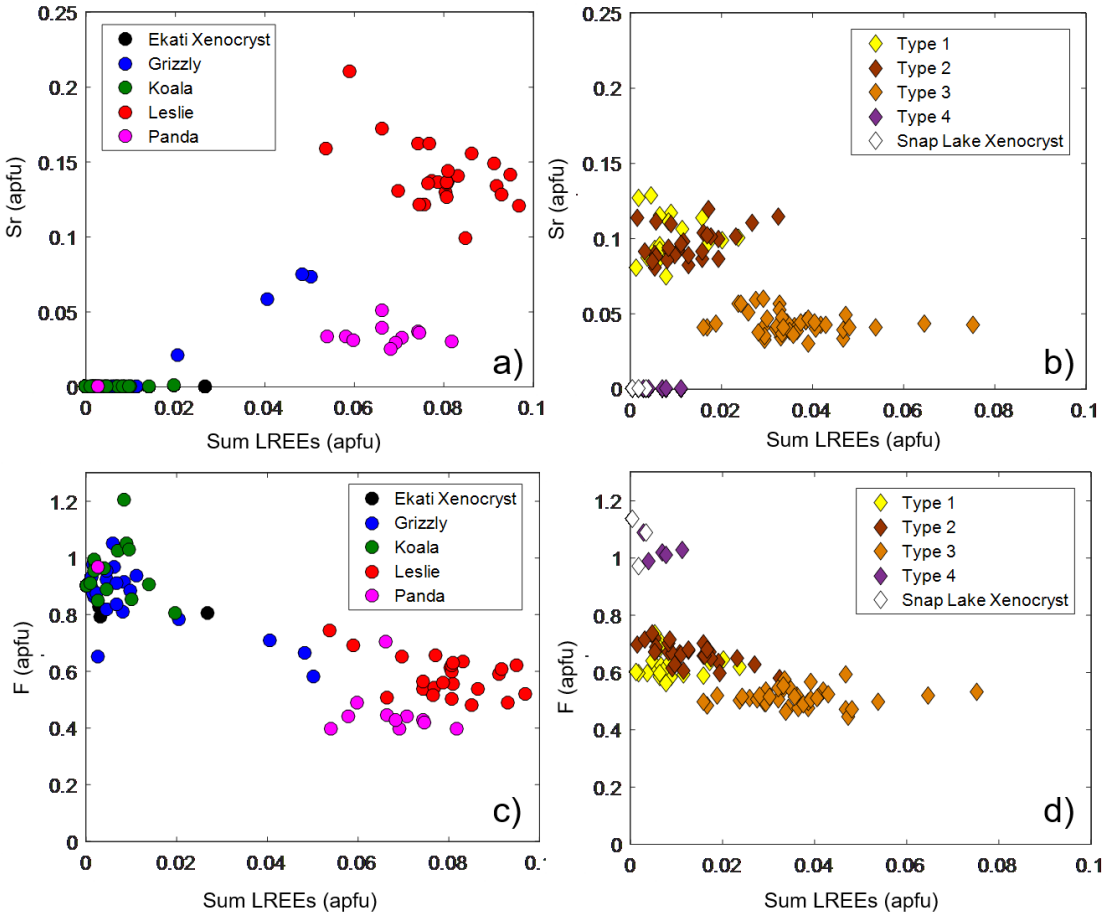


Figure 3.6 Compositions from EPMA analyses of apatite grains from the selected kimberlite pipes.

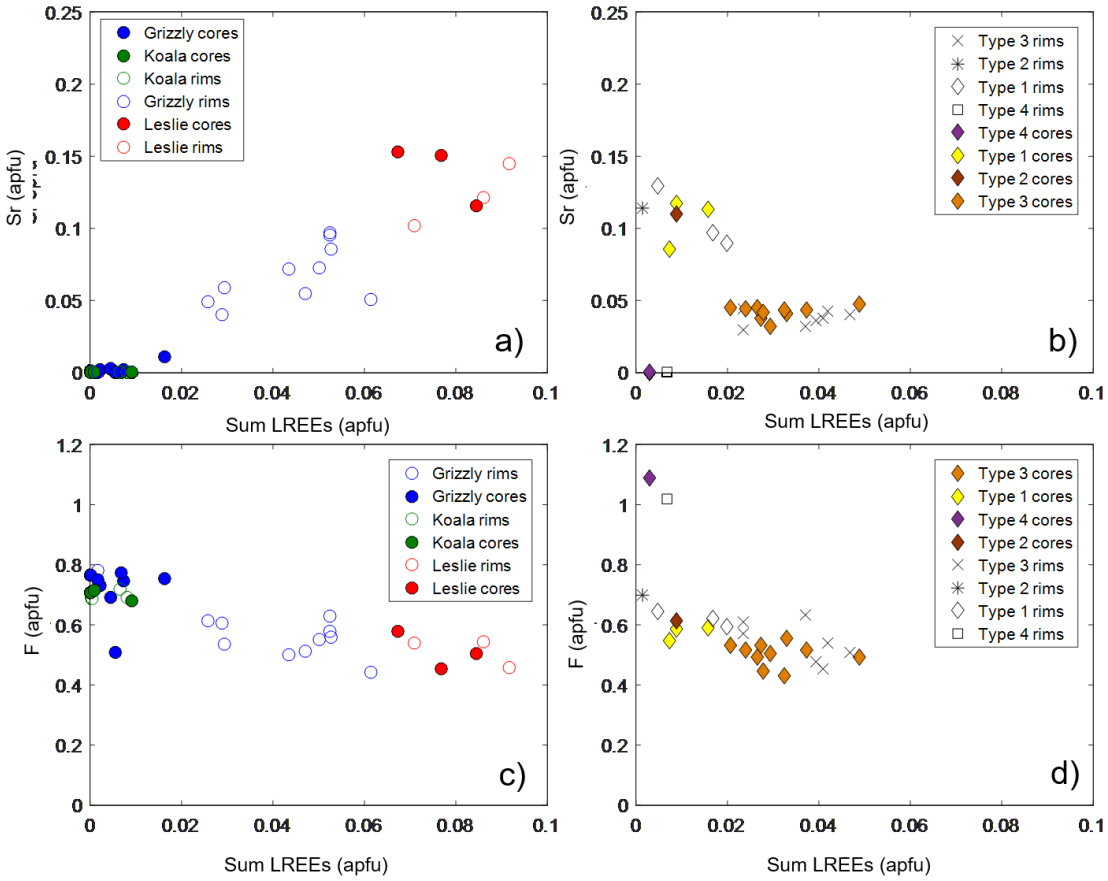


Figure 3.7 Composition from EPMA analyses of core-rim pairs of apatite from the selected kimberlite pipes. Full major element analyses of core-rim pairs are provided in supplementary data (Appendix C).

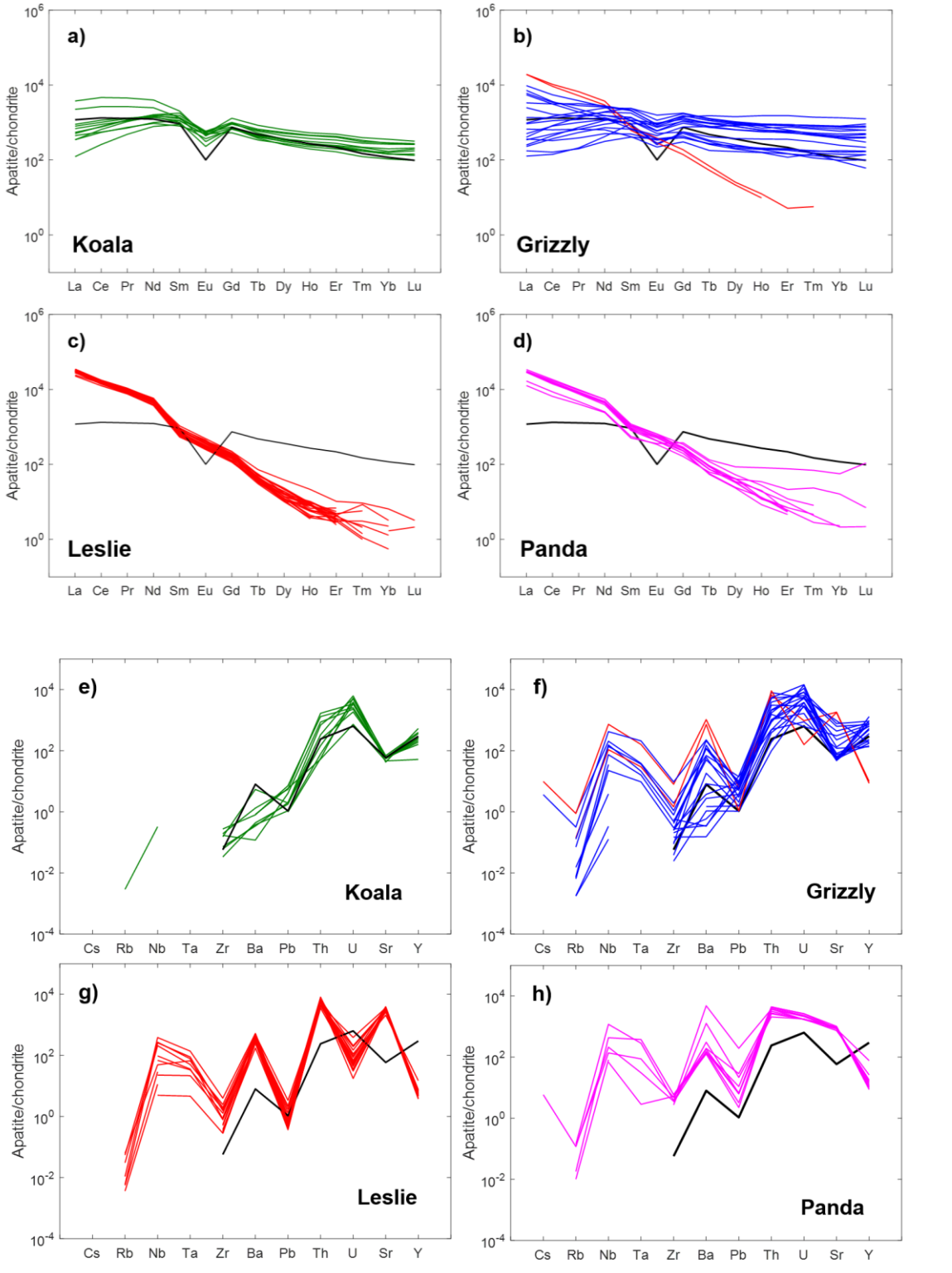


Figure 3.8 REE and spider diagrams of apatite from Ekati kimberlite pipes from LA-ICPMS. Composition of apatite from crustal xenolith is plotted as black line for comparison.

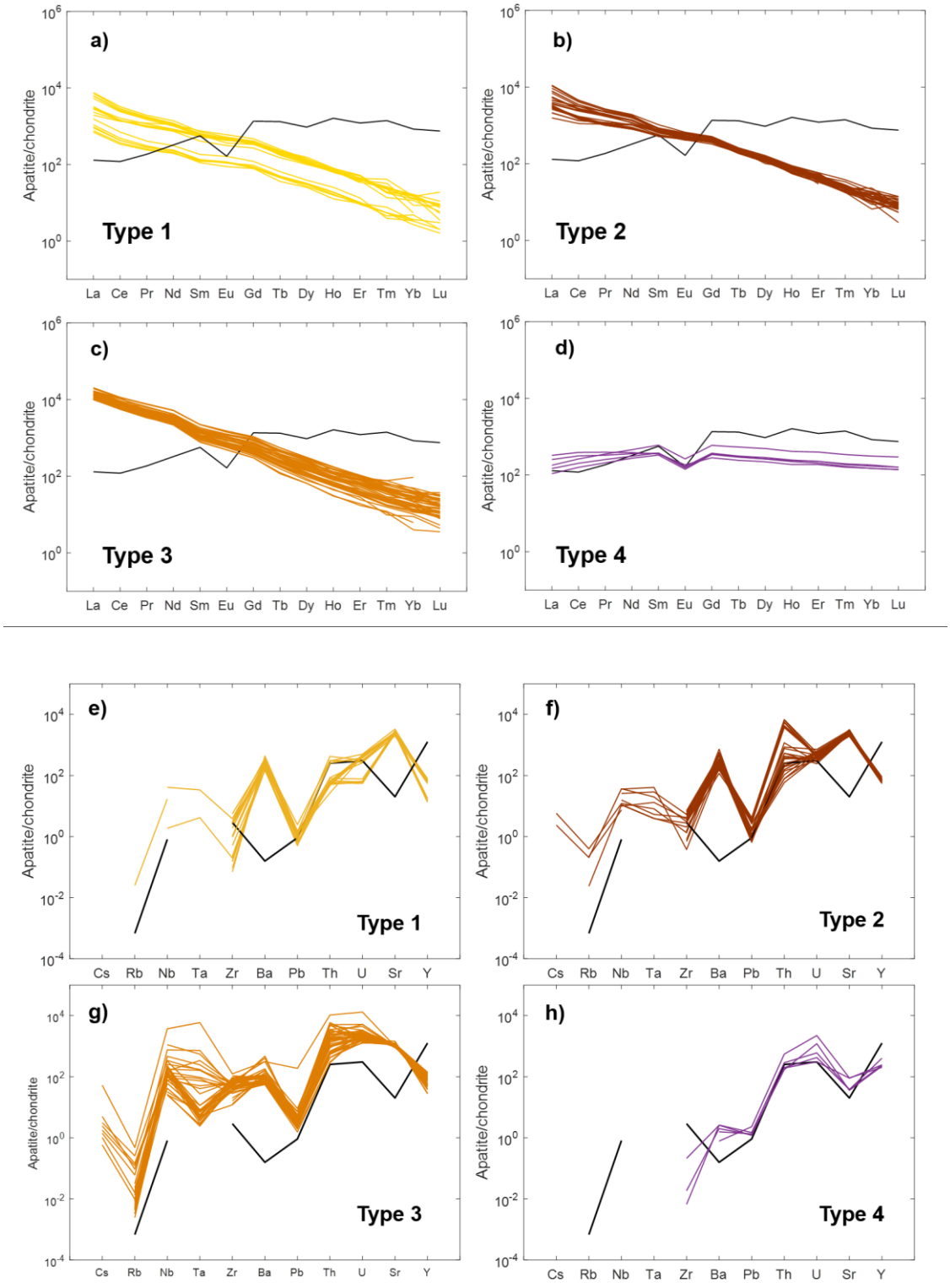


Figure 3.9 REE and spider diagrams of apatite grains from Snap Lake kimberlite from LA-ICPMS, separated into four textural types (see text for further details). Composition of apatite from crustal xenolith is plotted as black line for comparison.

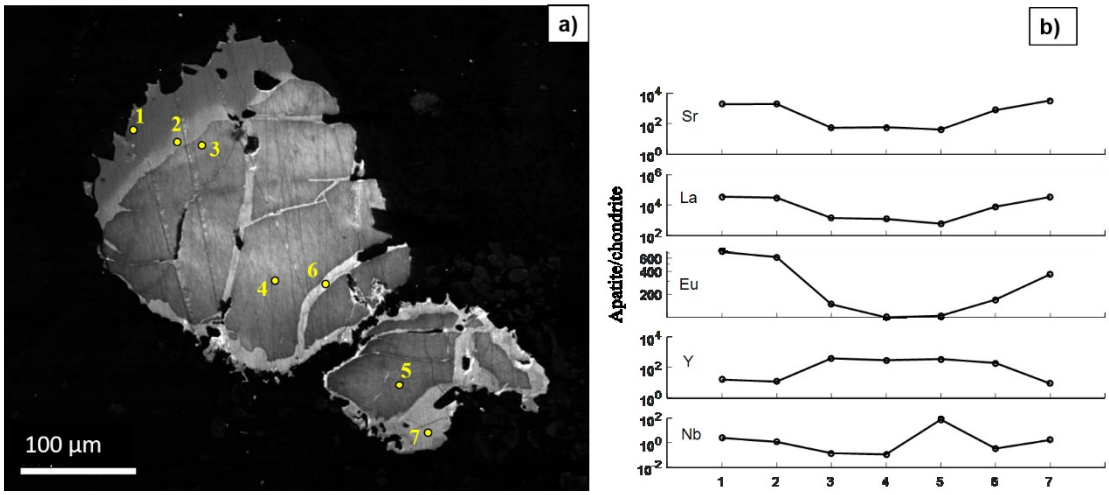


Figure 3.10 Apatite xenocryst from Leslie kimberlite with several stages of overgrowth and annealing by multiple generations of apatite growth, a) CL image of xenocrystic apatite with spot locations for quantitative analyses, CL spectra provided in Appendix B, and b) elemental changes through a track of the Leslie xenocryst (spots indicated on CL image), full major and trace element analyses of track spots are provided in supplementary data (Appendix C).

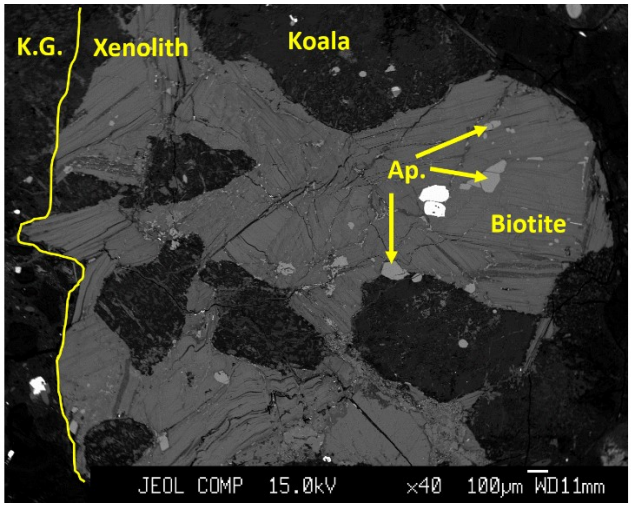


Figure 3.11 BSE image of a xenolith in Koala kimberlite with large biotite grains including subhedral apatite. Apatite and biotite grains analyzed for geothermometer. K.G. – kimberlite groundmass, Ap. - apatite.

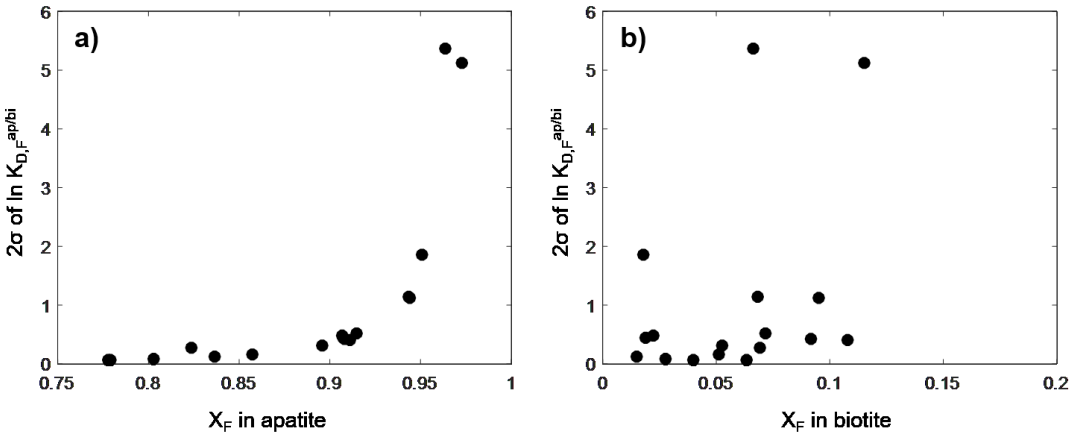


Figure 3.12 Two standard deviations (2σ) error of ln $K_{D,F}$ calculated for apatite-biotite thermometer compared to proportions of endmember F in (a) apatite, and (b) biotite.

# CHAPTER 4 DISCUSSION

## 4.1 Discriminating kimberlitic apatite

### 4.1.1 Geochemical signatures of kimberlite-derived apatite

Apatite is a resistate detrital mineral used for exploration of economic igneous bodies. Common in kimberlite groundmass, apatite has the potential to serve as an indicator for potentially diamond-bearing kimberlite bodies during exploration. It is therefore desirable to isolate geochemical signatures of apatite, not only that which crystallized from kimberlite magma, but also crustal apatite entrained in kimberlite magmas.

Apatite grains from this study represent both kimberlite-derived apatite (Leslie, Panda, Snap Lake and two grains from Grizzly) and apatite inherited from crustal rocks (the rest of Grizzly and Koala grains). REE diagrams (Fig 3.8, 3.9) provide a robust way to discriminate kimberlitic and inherited apatite in the studied samples. In comparison with an apatite xenocryst from a kimberlite-hosted crustal xenolith, kimberlitic apatite grains can be easily identified based on the steep negative REE slope, absence of Eu and Ce anomalies, and contents of other indicator elements (high Sr, Ba, low Y, Th/U>1; Fig 3.8, 3.9).

### 4.1.2 Comparison of kimberlite-derived apatite with apatite from other ultra mafic and alkaline rocks

Isolating kimberlitic apatite compositions from apatite crystallized from other sources is an initial step in establishing it as a possible indicator for diamond exploration. Compositions of apatite from various ultra mafic and alkaline sources has been widely reported in the literature, including two major “database” type works constructed by Belousova et al. (2002) and Mao et al. (2016). There are fewer data, however, for kimberlite-derived apatite.

Fig. 4.1 compares REE and discrimination diagrams for apatite from this study and those from other ultramafic and alkaline sources, including larvikite (Belousova et al. 2002), lherzolite (O'Reilly and Griffin 2000), clinopyroxenite (Mao et al. 2016), carbonatite (Belousova et al. 2002; Dawson and Hinton 2003; Mao et al. 2016) and a hypabyssal kimberlite dyke (Jos kimberlite, Somerset Island, Nunavuut, Canada; Malarkey et al. 2010). The REE compositions of apatite from carbonatite and the Jos kimberlite are

remarkably similar to that of Snap Lake Type 3 apatite. The distinct depletion of HREEs in Leslie kimberlitic apatite grains appears to be unique. The alkaline- and ultramafic-sourced apatite have comparable concentrations of REEs to Type 3 apatite; however, the samples show a slightly positive Ce anomaly, not present in kimberlitic apatite. Additionally, apatite from larvikite has a marked negative Eu anomaly, due to fractionation of plagioclase.

In Fig. 4.1a and b, data from this study are compared with apatite compositional fields reported by Belousova et al. (2002). They examined apatite grains from a wide range of source rocks and defined fields to best discriminate apatite crystallized in different environments, using Sr, Y, $(Ce/Yb)_{CN}$ and REEs. Data from this study is plotted over their fields. The result is that apatite grains from Snap Lake (Types 1, 2 and 3) plot largely within the field defined for lherzolitic apatite, and Type 3 overlaps slightly with the carbonatitic field. Apatite grains from the Ekati kimberlite pipes, however, plot outside any of the fields defined by Belousova et al. (2002). The compositions of apatite from Leslie, Panda and Grizzly are notably different from apatite grains reported in the literature due to their high Sr, high LREE, and low HREE contents.

The combined high Sr (>1 wt%) and high REE (>1.5 wt%) contents, along with the high $(Ce/Yb)_{CN}$ (>1000) seen in Ekati apatite grains are compositions unique to kimberlite-derived apatite, and can potentially be used to identify kimberlite-sourced detrital apatite.

### 4.1.3 Geochemical changes in crustal apatite carried by kimberlite melt

The main changes in the composition of crustal apatite during entrainment in kimberlite magma can also be assessed using grains from Grizzly and Kola. Both kimberlite melts, though imbibing abundant apatite crystals, crystallized minimal apatite directly from the melt. The flat REE patterns and distinct Eu anomaly (Fig. 3.8) confirm the crustal origin of these grains. However, the range of analysed apatite grains from Koala and Grizzly show variation in the chemical composition (Fig. 3.8), possibly due to the reaction of apatite with kimberlite magma. Particularly for apatite grains from Grizzly, which show significant resorption (Fig. 3.1f), the chemical differences are marked. Both Grizzly and Koala apatite show enrichment in LREEs and significant reduction of the negative Eu anomaly (Fig. 3.8) compared to the reference xenocryst analysis. Grizzly also has an increased Sr and Ba,

more reflective of a kimberlite-derived apatite composition, though Y is consistent with xenocrystic apatite abundances.

Grizzly apatite show a range of compositions between crustal (similar to Koala) and kimberlitic (similar to Leslie; Fig. 3.7) and consist of a rounded resorbed core, surrounded by an overgrown rim, also with a resorbed surface (Fig 3.1f). The separate analysis of cores and rims with WDS showed that the rims approach a kimberlite composition similar to Leslie (Fig. 3.7) and the cores are virtually identical in composition to Koala apatite, which have been determined to be inherited from crustal rock. These marked compositional distinctions, and the sharp contact between the core and rim in Grizzly apatite, suggest that this pattern is not a result of diffusion, but an overgrowth of kimberlitic apatite. The small size of Grizzly apatite (avg. 10um) precluded the separation of core and rim during LA-ICPMS analyses, which have resulted in the observed compositional range of mixed core-rim compositions of REE and spider diagrams. In addition, some natural variation in xenocrystic apatite composition contribute to the variation. On the contrary, the SEM and CL images of Koala apatite (Fig. 3.1a) and consistent composition of apatite indicates that all analysed grains of apatite from Koala are crustal and have no kimberlite-overgrowth rim.

The apatite xenocryst from Leslie kimberlite which showed multiple generations of apatite growth reveals some interesting geochemical features with the track-spot analysis (Fig. 3.10). The outward edges of the xenocryst grain (spot 3) do not show major diffusional or zoning changes from analyses at the core of the grain, except perhaps a slight increase in La and Eu concentrations.

### 4.1.4 Diffusion of trace elements in apatite

Comparison of the composition of Koala grains enclosed within xenoliths and those in direct contact with the kimberlite (Fig. 4.3c) appear to show that interaction with kimberlite magma decreased concentrations of Th, LREEs and Pb. The data also show increases in LILE's (K, Rb, Ba) and HFSE's (Nb, Ti). Considering diffusion rates of trace elements into apatite, and their respective mechanisms for incorporation into the apatite, isovalent substitution of a major component of the apatite structure should have the fastest diffusion rates e.g. Sr-Ca substitution (Cherniak 2000). Elements which require coupled substitution,

such as REEs have been shown to be rate limited by their charge-paired couple, i.e. Si or Na, which are slower moving in the apatite crystal lattice (Cherniak 2000; Tepper and Kuehner 1999). This suggests that if xenocrystic apatite grains are to be affected by kimberlite melt interaction, the largest change should occur in Sr concentrations.

In fact, when grains from Koala in contact and not in contact with the kimberlite melt are compared (Fig. 4.3c), there is virtually no difference in the Sr concentrations of these grains, possibly indicating that there was little or no diffusion of trace elements between the kimberlite magma and the inherited crustal apatite crystals. The differences in REEs, Pb and LIL's, therefore, are more likely explained by natural variation in the sampling of the xenocrysts, and natural variation in the composition of the xenocryst host rock.

### 4.1.5 Potential of detrital apatite for kimberlite exploration

Based on the comparison of kimberlite-derived apatite in this study with apatite from other sources, it is suggested that kimberlitic apatite can be distinguished from apatite from other rock types. As shown in section 4.1.2, kimberlite-derived apatite grains can be compositionally very similar to apatite grains from lherzolites and carbonatites. However, of the Ekati kimberlite samples studied here, Leslie and Grizzly have produced unique compositions of apatite not replicated by other ultramafic or alkaline sources. It is unclear whether this result is caused by a feature of the Ekati group kimberlite, or if specific processes in the history of each kimberlite has produced this unique apatite composition.

The best geochemical indicator to distinguish kimberlitic from carbonatitic apatite is lower Y, and slightly higher Sr. Kimberlite-derived apatite can be compositionally very similar to apatite sourced from lherzolite. This overlap should be considered when employing the discrimination fields presented by Belousova et al. (2002).

## 4.2 Origin of apatite in Ekati and Snap Lake kimberlite pipes

In this section, differences in habit and composition of kimberlitic apatite are discussed. Additionally, the implications of variation in crystal morphology, zoning and CL are explored in terms of the crystallization conditions of apatite. Lastly, an evaluation of the differences in composition of apatite between kimberlite bodies is conducted, and an assessment of how composition could be indicative of crystallization media (e.g. melt vs. fluid crystallization).

### 4.2.1 Features of apatite crystallization

Previous experimental studied have shown a relationship between the crystal habit of apatite and the degree of undercooling (Wyllie et al. 1962). Apatite forms small equant crystals in the presence of a fluid at low degrees of undercooling (crystallization of a melt below the true temperature threshold of the mineral). It becomes more acicular at high degrees of undercooling, which can result from rapid cooling (Höche et al. 2001) or from exsolution of a fluid phase from the melt.

Panda, Leslie and Snap Lake's Type 3 apatite crystals forms equant, euhedral to subhedral sub-hexagonal or prismatic. This habit suggests crystallization from a melt at low degrees of undercooling. The slight increase in the elongation along the c-axes of some lath-like crystals in Leslie could correspond to an increase in the cooling rate or an increase in apatite saturation during the crystallization (Höche et al. 2001). Conversely, the acicular radial aggregates of Types 1 and 2 apatite from Snap Lake suggests diffusion-controlled growth, a result of high degrees of undercooling or supersaturation.

Apatite from Panda kimberlite and Type 3 from Snap Lake kimberlite share many similarities. They show complex oscillatory zoning in CL images, likely related to REE variations and have very similar geochemical features, such as high LREEs, low Sr and lower proportion of F. This suggests similar growth mechanism and conditions for Panda and Snap Lake Type 3 apatite. Fine compositional oscillations are a product of local growth rate and concentration variations. This indicates slow crystallization under static, low supersaturation conditions (Allègre et al. 1981; Tepper and Kuehner 1999) On the contrary, Leslie apatite shows patchy zoning with sharp boundaries and irregular zones, generally spanning from core to rim. Euhedral shape and patchy textures could indicate overgrowth crystallization from a high-temperature fluid. Grizzly has anhedral, equant apatite grains, whose edges show resorption. The apatite crystals also have distinct zoning with rounded resorbed cores of xenocrystic composition surrounded by a rim of kimberlitic composition. This texture points to multiple stages of growth and resorption of apatite, suggesting oscillation above and below apatite saturation in the kimberlite melt.

Apatite Types 1 and 2 from the fresh parts of the Snap Lake dyke occur as radial clusters of anhedral acicular crystals, indicative of a high degree of undercooling and possibly

crystallization in the presence of a fluid (Wyllie et al. 1962). CL images show clear core-rim zoning in these apatite grains, with dark core and bright rim possibly indicating a rapid change in the composition of the apatite-precipitating fluid.

### 4.2.2 Variation in the composition of kimberlite-derived apatite

***REEs*** Kimberlitic apatite from Leslie, Panda, Grizzly and Type 3 Snap Lake apatite show very steep negative REE slopes similar to the REE slopes of the host kimberlite magma. However, the four kimberlite pipes show notable variations in the REE pattern, especially the concentration of HREEs. This may be due to the differences in the bulk rock concentration of these elements, or due to fractionation during kimberlite crystallization. Comparison of REE slope of apatite to those of the bulk kimberlite (Fig. 4.2d) shows that larger HREE-depletion of apatite from Leslie, Panda and Grizzly can be explained by the more HREE depleted bulk rock compositions (Nowicki et al. 2004). In Snap Lake, the three apatite types and bulk rock analyses (provided by DeBeers Canada) do not show similar HREE flattening to the Ekati kimberlites.

***Other trace elements*** Other elemental signatures can help to isolate variations in crystallization conditions for kimberlite-derived apatite grains. The Th/U ratio in apatite (Fig. 4.3b) shows a large variation between coherent Grizzly and Leslie bodies with Th>>U, Panda with Th>U, and xenocrystic apatite including Koala, where U<Th (Fig. 3.8). Th and U behave similarly in reducing conditions during magmatic fractionation but Th can be much less soluble than U in aqueous and carbonate-rich fluids. Keppler and Wyllie (1990) showed that high-temperature fluids strongly incorporate U, but not Th; however this partitioning is highly dependent on fluid salinity (availability of complexing ions) and on oxygen fugacity (Bali et al. 2011) . The high Th/U in Leslie and Grizzly apatite grains could imply fluid separation prior to crystallization of apatite (or crystallization from a high-T fluid, which retained most of the U). Oxygen fugacity ($fO_2$) could also exert a control on the partitioning of U into apatite, where $U^{6+}$ is significantly less compatible than $U^{4+}$. However, comparison Th/U ratio to the ratios of other element pairs sensitive to the oxidation state (e.g. Sc-V; Mallmann and O'Neill 2009) shows no correlation. Thus, U depletion due to the fluid separation is the preferred explanation.

### 4.2.3 Origin of apatite

Based on the data presented above, it is suggested that kimberlite-derived apatite crystallization was similar within each of the three identified compositional groups (1) Leslie and Grizzly kimberlitic apatite, (2) Snap Lake Types 1 and 2, and (3) Snap Lake Type 3 and Panda apatite.

Due to the acicular, supersaturated texture of Type 1 apatite in Snap Lake, along with the occurrence of Type 2 grains in carbonate veins, these grains likely crystallized from a deuteric kimberlite fluid. The resultant chemical signature is high in Sr and low in LREEs (Fig. 4.3a) with a moderate REE slope and low concentrations of Th and U (Fig. 4.3b).

Apatite grains from Panda kimberlite and of Type 3 in Snap Lake show signs of crystallizing from a melt. Prismatic grains and oscillatory zoning indicate magmatic crystal growth, yielding a composition low in Sr and high in LREEs, with moderate and similar concentrations of Th and U (Fig. 4.3).

Leslie and Grizzly grains both have unique textural features and an unusual composition combining high Sr, high LREEs and Th/U>100. Due to the overgrowth textures and unusual composition of Leslie apatite, these grains could have a more complex history involving influence of both magmatic and fluid-mediated growth. Enrichment in both Sr and LREEs (Fig. 4.3), as well as the loss of U to a fluid could indicate a two-stage growth process, since Sr and LREEs should behave differently in the presence of a fluid. The composition of kimberlitic apatite grains from Grizzly tends to plot somewhere in between the compositions of Leslie and Panda apatite. While this could be dilution of the analyses due to small grain size and the abundance of xenocrystic apatite in Grizzly, it must be considered also that the melt could have been near fluid saturation, producing compositions of apatite slightly different from either a fluid or a melt.

### 4.3 Substitution mechanisms in kimberlitic apatite

REE and other trace elements substitute into two octahedral sites occupied by Ca. The charge balance between $REE^{3+}$ and $Ca^{2+}$ can be compensated by several mechanisms:

$$REE^{3+} + Na^{+} = 2Ca^{2+} \quad (1)$$

$$REE^{3+} + SiO_4^{4-} = Ca^{2+} + PO_4^{3-} \quad (2)$$

$$2REE^{3+} + [v] = 3Ca^{2+} \quad (3)$$

Where [v] represents a vacancy in the crystal lattice. Fig. 4.2a examines these three possible mechanisms for kimberlite-derived apatite samples of this study. The slope -1 corresponds to substitution relationship mechanism (2) (Rønsbo 1989). Slopes progressing towards -1/2 represent an increase in the importance of mechanism (1) involving $Na^+$, with mechanism (3) residing at -2/3. Most of Snap Lake apatites and Leslie apatite follows -1/2 trend, suggesting substitution mechanism (1). More OH-rich apatite from Panda follows a slightly steeper slope representing a mix of mechanisms (1) and (2). This is possibly in accordance with experiments (Fleet et al. 2000a, b) which suggest that hydroxyapatite preferentially accommodates REE's by mechanism (2), while fluorapatite combines mechanisms (1) and (2). Fig. 4.2b examines a relationship between F and Na in kimberlitic apatite; however, none of the kimberlitic apatite samples show a marked correlation of F and Na. This could suggest that a monovalent cation is substituting to charge balance REEs in the apatite structure with mechanism (1), possibly $Li^+$ (not measured in this study; Pan and Fleet 2002).

Several other substitution mechanisms (Pan and Fleet 2002) could have affected the composition of these kimberlite-derived apatite grains such as:

$$REE^{3+} + S^{2-} = Ca^{2+} + F^- \quad (9)$$

$$SO_4{}^{4-} + SiO_4{}^{4-} = 2PO_4{}^{3-} \quad (10)$$

Incorporation of either of these sulfur anions would affect the apparent mechanisms of coupled substitution for REEs into the apatite structure. Sulfur was not analysed in this study. This and other potential rare substitutions are a possible subject for future inquiry in kimberlitic apatite (Sb, Ag, $CO_3$ etc.).

## 4.4 Modelling kimberlite composition during apatite crystallization

### 4.4.1 Nernst-style partitioning models

Trace element content in the studied apatite and their partition coefficients from the literature are used to model the composition of kimberlitic melt during apatite crystallization. Applied are $D^{apatite/melt}$ for carbonatitic melt (run BS25;Klemme and Dalpé 2003), silicate melt (run 71a; Prowatke and Klemme 2006), and for perovskite $D^{perovskite/melt}$ for carbonatitic and kimberlitic melts (runs PC520 and PC513, respectively; Beyer et al. 2013). When comparing these hypothetical melts with bulk rock data for the selected

kimberlite pipes, appropriate proportions of macrocrystal olivine of mantle origin were subtracted from the kimberlite compositions, using estimates from Nowicki et al. (2008) for the Ekati kimberlite bodies and Fulop et al. (2017) for Snap Lake. This assumes a minimal effect of subsolidus alteration; likely a valid assumption for the exceptionally fresh kimberlite from Ekati, while Snap Lake could be more affected. As D values for apatite are different in silicate and carbonate melts, the modeled trace element patterns are different for carbonatitic and silicate melts crystallizing apatite with compositions corresponding to this study (Fig. 4.4).

Both "silicate" and "carbonatitic" models show relatively similar patterns to the whole rock concentrations of the studied elements (Fig. 4.4), but concentrations in "carbonatitic" model are higher due to the lower D. Calculations suggest that to achieve the observed concentrations of REE's in apatite, the grains would need to crystallize from lower proportions of residual silicate melt (10-30%) than residual carbonate melt (1-10%). Few discrepancies of the "silicate melt" model include slightly higher Nb and Rb and slightly lower Zr than in the bulk rock. Anomalously low estimates for $D_{Cs}$ and $D_U$ as presented in experimental studies (Klemme and Dalpé 2003; Prowatke and Klemme 2006) present issues for the modelling and are not shown in Fig. 4.4. The possible explanations for further observed discrepancies between the modelled silicate melt and the whole rock concentrations include: (1) the likely differences of D in the used silicate models and in the more mafic kimberlite melt, (2) a possible effect of fluid separation and subsequent melt depletion in trace elements, (3) crystallization of apatite from a magmatic fluid as opposed to the kimberlite melt, and (4) other minerals in the kimberlite groundmass taking which took trace elements.

The proportions of residual melt at the time of the apatite crystallization to best reproduce element concentrations using the "silicate melt" model are: 15-30 wt% for Leslie, 10-20 wt% for Grizzly, 5-10 wt% for Panda, 10-20 wt% for Snap Lake Type 3 and 30-80 wt% for Snap Lake Types 1 and 2. Respectively for "carbonatitic melt" models, these estimates are 2-5 wt% for Leslie, 2 wt% for Grizzly, 1wt% for Panda, 10-20 wt% for Snap Lake Types 1 and 2, and 1-3 wt% for Snap Lake Type 3.

The applied D's experimentally determined for apatite equilibrated with much more silica-rich melts than kimberlitic (Prowatke and Klemme 2006), and therefore are not ideally applicable for a kimberlite system. However, low $SiO_2$ (and likely higher volatiles) would decrease melt polymerization and therefore decrease $D_{REE}$ into apatite (Ryerson and Hess 1978), which would give even further discrepancies between these silicate models and the bulk rock. In addition, if Leslie and Snap Lake Type 1 and 2 apatite grains crystallized from a fluid, as shown by their textures and elemental concentrations, the partition coefficients would be higher, and show distinctly different patterns (Ayers and Watson 1993).

Volatile loss during the eruption, after the apatite crystallization could extract certain elements (e.g. Pb, Cs, LILE's) from the bulk rock composition compared to the elements that prefer the melt such as REEs, HFSE's (Zajacz et al. 2008). There is no notable decoupling in these samples; however, Leslie, Grizzly and Snap Lake Type 1 apatites are slightly depleted in Pb, possibly indicating depletion by a fluid.

Based on the constructed models, and comparison of elements less likely to be affected by fluid loss or other phases (e.g. La, Rb, Zr, Th), the models for carbonatitic melt more closely fit Panda and Snap Lake Type 3 apatite. Leslie and Grizzly show a more imperfect fit with the carbonate melt models, however, as previously mentioned, the likelihood of free-fluid involvement in apatite crystallization could significantly obscure the modeled melt compositions.

The uncertainties of this method include: (1) use of partition coefficients for apatite in the "silicate melt" model, which were derived from melts with a different composition than kimberlite, (2) the unknown effect of temperature on D's, (3) the effect of substitution mechanisms in apatite impacting the crystal chemical controls (i.e. halogen species, Si content). Additionally, this method assumes that all the considered elements obey Henry's law with uptake into the apatite structure. This is of concern with respect to Sr, where the concentrations reach almost 3 wt% Sr in Leslie apatite grains, and Henry's law behaviour has not been confirmed at these concentrations. The only other trace elements of appreciable concentrations in apatite grains from this study are REEs. Watson and Green

(1981) verified Henrian behaviour for REE contents up to several weight percent in apatite, a reasonable comparison for kimberlitic apatite presented here (max 2.5 wt%).

### 4.4.2 Perovskite models

Though Armstrong et al. (2004) cited perovskite crystallization prior to apatite crystallization in Ekati pipes, a different conclusion is suggested here for both Leslie. The large size and euhedral habit of apatite in Leslie kimberlite, as well as the small inclusions of monticellite, indicate early crystallization of apatite. In Grizzly, perovskite grains are large and well formed, while apatite seems to have crystallized late in the kimberlite evolution, having a brief residence time nucleating on the edges of xenocrystic apatite grains. In this case, data from this study agree with Armstrong et al. (2004) that perovskite was likely crystallizing before apatite, however, there is no significant depletion of HFSE's in apatite from Grizzly. Additionally, apatite may not have been crystallizing from the kimberlite melt, as the crystal composition suggests a fluid presence during crystallization (high Sr, depletion in U; discussed in section 4.2.3). Given the resedimentation textures in Panda kimberlite, it is difficult to explicitly define a crystallization sequence for groundmass minerals in this case. However, considering the concentrations of HFSE's in apatite from Panda (Fig. 3.8), there is no significant depletion which might indicate prior crystallization of perovskite.

Looking to the melt models, the low concentrations of REEs predicted by the perovskite model in Leslie is consistent with textural observations that apatite was likely crystallizing earlier, if not concurrently with perovskite. Additionally, the silicate melt model for perovskite in Leslie shows decoupling of U and Th opposite to what was observed in apatite compositions. Though the partition coefficients for U and Th into perovskite are not distinctly different (Fig. 1.1), the contrary behaviour of these elements in the Leslie melt system is unexpected. The models for crystallization of perovskite in Panda and Grizzly agrees well for silicate melt crystallization of the two minerals.

## 4.5 Comparison of apatite data with current models for eruption

Here, all the presented apatite data for each kimberlite is put into context of the existing evolution and eruption models for the kimberlite pipes, as discussed in section 1.4. Data from this study generally supports the models of eruption for hypabyssal kimberlite,

however, there are some inconsistencies with the crystallization of apatite in Panda and the eruption model for volcaniclastic kimberlite.

Samples from Leslie and Grizzly kimberlite pipes show a large Th/U ratio, which is interpreted as being a result of fluid separation. Separation and loss of fluid in coherent kimberlite facies would agree with data from previous studies, and explain the low U in apatite. Additionally, abrupt changes in crystallization conditions, as suggested by the textures for Leslie apatite grains, could be support for fluid exsolution from the kimberlite melt. This scenario is also a possibility for Grizzly apatite grains, because of the alternating growth-resorption patterns and similar Sr/La partitioning, whose ratios are consistent with a silicate melt, though in drastically enriched concentrations. This interpretation is similar to the conclusions developed for apatite Types 1 and 2 from Snap Lake; in which case clear textures of a fluid-crystallized apatite is consistent with enriched concentrations of Sr, and alteration by a deuteric kimberlite fluid.

Interpretations of apatite textures from Panda are generally inconsistent with the proposed model. The residence time required by the oscillatory zoning seen in the grains is inconsistent with a rapid eruption in the presence abundant volatile phases. Crystallization of these apatite grains could have occurred in discreet segregations of magma, unaffected by the free-fluid phase, however, the kimberlite is thought to have erupted very quickly, leaving little time for static development of complex zoning. The melt models for Panda, as well as the textural observations, show a consistency with apatite crystallization from a melt. It is possible that apatite grains in Panda kimberlite were crystallizing before fluid exsolution.

Crystallization of apatite from a melt indicates that the melt has reached apatite saturation. The variation in occurrence of apatite in the selected kimberlite pipes suggests that some melts reached apatite saturation (e.g. Leslie, Panda, Snap Lake), while others (Koala, Misery, Beartooth, Grizzly) did not.

The major compositional controls on apatite saturation in melt systems are concentrations of $P_2O_5$, CaO, and $SiO_2$. Experiments show that apatite crystallization begins at lower T, higher $P_2O_5$, higher $SiO_2$ and lower CaO contents, with no notable effects of pressure (Green and Watson 1982; Tollari et al. 2008; Watson 1980). Thus, dissolution of crustal

apatite is enhanced in high-T, carbonate-rich melts, while $CO_2$ degassing and assimilation of crustal xenoliths would promote apatite saturation. The experimental results on apatite saturation in silicic systems of Watson (1980) and Tollari et al. (2008) are compared here with bulk rock kimberlite data from four Ekati pipes, as presented in Nowicki et al. (2008) and from Snap Lake (data provided by DeBeers Canada). It should be noted that the units are not directly comparable because the bulk rock measurements should include existing apatite grains sitting in the kimberlite groundmass. This assumes that all phosphorous in the kimberlite is hosted in apatite.

Available bulk rock data for the selected samples is presented Figure 4.5 comparing phosphorous data with Ca contents, and contamination index, which is considered as a proxy for Si content, because of its indication for crustal contamination. The contamination index evaluates the proportion of crustal contamination or weathering of a kimberlite, with higher contamination indices (generally >1) indicating a contaminated kimberlite. Presented in Clement (1982), this index is calculated as:

$$C.I. = \frac{SiO_2 + Al_2O_3 + Na_2O}{MgO + 2K_2O} \qquad (11)$$

The result, for the pipes studied here, is a higher contamination index for the volcaniclastic kimberlite, Panda, Misery and Koala, as well as the most altered facies of Snap Lake. This cannot readily explain the occurrence of kimberlitic apatite in the Ekati kimberlite samples, though could be a result of limited sample selection.

Misery and Koala melts could have achieved conditions to crystallize apatite from the melt (high Si, low Ca); however, the bulk rock does seem very low in phosphorous in both these pipes. Potentially, insufficient $P_2O_5$ in the melt was the limiting factor for crystallizing apatite. Additionally, fractional crystallization could have eventually increased the concentration of $P_2O_5$ in the residual melt. If, in a rapid eruption setting, there was very little fractional crystallization before the melt reached the surface, $P_2O_5$ concentrations in the residual melt may not have reached sufficient levels to precipitate apatite in the melt. It is clear, however, that apatite was not a liquidus phase in the volcaniclastic kimberlite, excepting Panda. In Koala, apatite may not have been far from a liquidus phase, since the

xenocrystic apatite grains do not show significant signs of resorption by the kimberlite magma.

The apatite grains seen in Grizzly kimberlite pose an interesting question for the conditions of apatite saturation in this melt. The grains have unique texture and composition, with rounded cores of xenocrystic apatite, and rims of kimberlitic apatite. Both generations of apatite, however, show evidence of resorption. This suggests that apatite was wavering above and below the saturation line. Apatite was a non-saturating phase during incorporation of the xenocrysts, and therefore began to resorb the grains at the boundaries. Exsolution of a free-fluid phase caused the crystallization of Sr- and LREE-rich apatite from the fluid, nucleating on the xenocrystic grains. Physical separation of the fluid from the magma, as suggested by the model, put apatite in contact with the dry melt, again triggering resorption of the crystallized apatite.

The behaviour of apatite in the Snap Lake kimberlite also suggests unusual behaviour of apatite saturation in the dyke system. Though both sections of the kimberlite (fresh facies HK1, HK2, HK5, and altered facies HK3, HK4, HK6) show a range of phosphorous contents in the bulk rock (Fig. 4.5), only the more altered facies appear to have crystallized apatite from the kimberlite melt (Type 3). Types 1 and 2 apatite are consistent with apatite crystallized from a fluid, which supports a model of hydrothermal alteration by deuteric kimberlite fluids. Type 3 apatite, however, shows signs of a magmatic origin in the altered zones of Snap Lake where the C.I. is higher than that of the fresher facies. An increase in the silica content in these zones by incorporation of significant proportions of crustal xenocrysts could have pushed the magma into saturation of apatite, triggering magmatic crystallization.

Because of the similarities of SL Type 3 and Panda apatite grains (as discussed in section 4.2), a similar mechanism is suggested for triggering the crystallization of a magmatic apatite phase. The contamination index for Panda is higher than that of the other apatite-bearing kimberlite bodies from Ekati (Leslie and Grizzly), and is again similar to SL Type 3. It is possible that significant incorporation of crustal xenocrysts caused local increases in $SiO_2$ contents of the melt. This could have pushed the magma in Panda into the field of apatite saturation, crystallizing the observed grains. This kind of extensive contamination

at depth would also have aided voluminous decarbonational degassing, in accordance with the model proposed by Stone and Luth (2016), causing rapid ascent of the volatile-rich magma and volcaniclastic eruption.

When comparing all the studied volcaniclastic kimberlite pipes, it is unclear why the kimberlitic apatite occurs in Panda, but not the others. However, this study is limited in sample number, and the volcaniclastic bodies are individually very complex. Additionally, there is no frame of reference for where within the pipes the samples were taken. Considering the multiphase nature and complexity of facies in each kimberlite, a more representative overview of apatite occurrence is required to properly assess the phosphorous and fluid history of these kimberlite pipes.

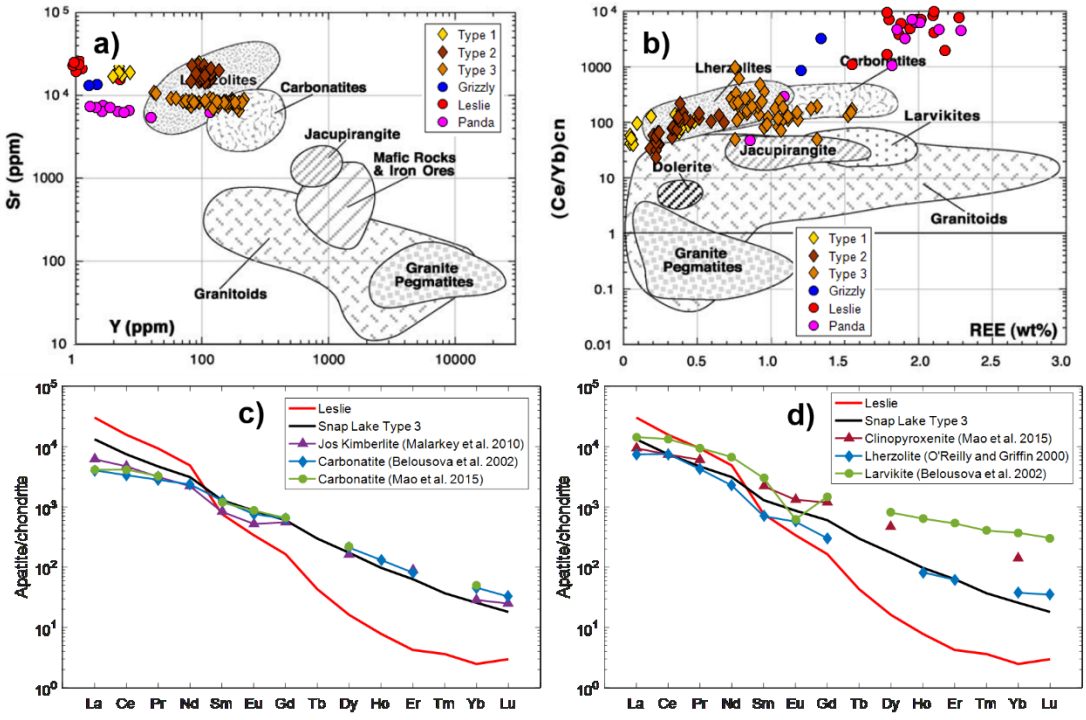


Figure 4.1 Comparison of kimberlitic apatite (this study) with fields defined for apatite compositions from Belousova et al. (2002). Comparison of REE slopes with apatite from other ultramafic and alkaline sources.

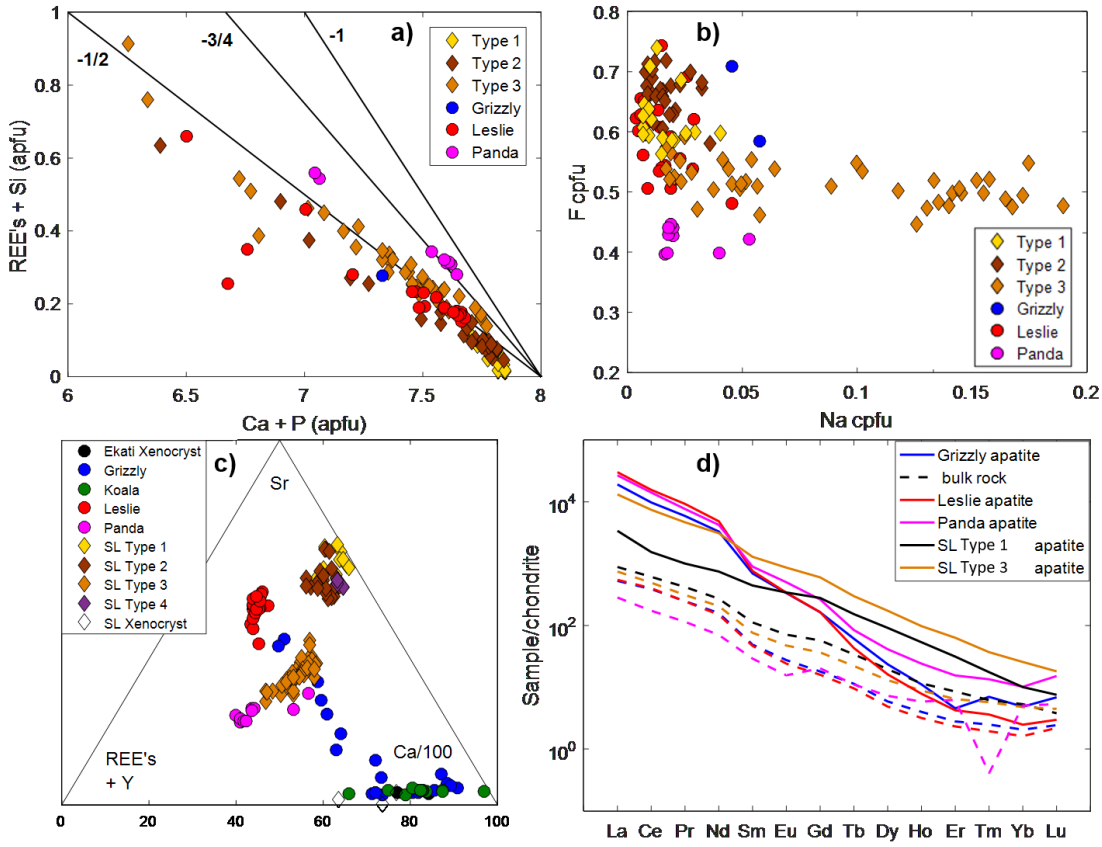


Figure 4.2 Trace element composition of apatite from selected kimberlite pipes. a) investigation of charge-coupled substitution mechanisms for $REE^{3+}$ incorporation into kimberlitic apatite, (Si+REEs) vs. (Ca+P) in apatite, black lines through the point (8,0) have the slopes -1, -3/4 and -1/2, where the line -1 represents substitution $REE^{3+} + Si^{4+} = Ca^{2+} + P^{5+}$, b) F vs. Na in kimberlitic apatite, investigating control of halogen species on preferential substitution mechanism for REEs, c) ternary diagram representing occupation of the octahedral site in apatite, d) comparison of HREE depletion with relative HREE depletion in bulk rock kimberlite.

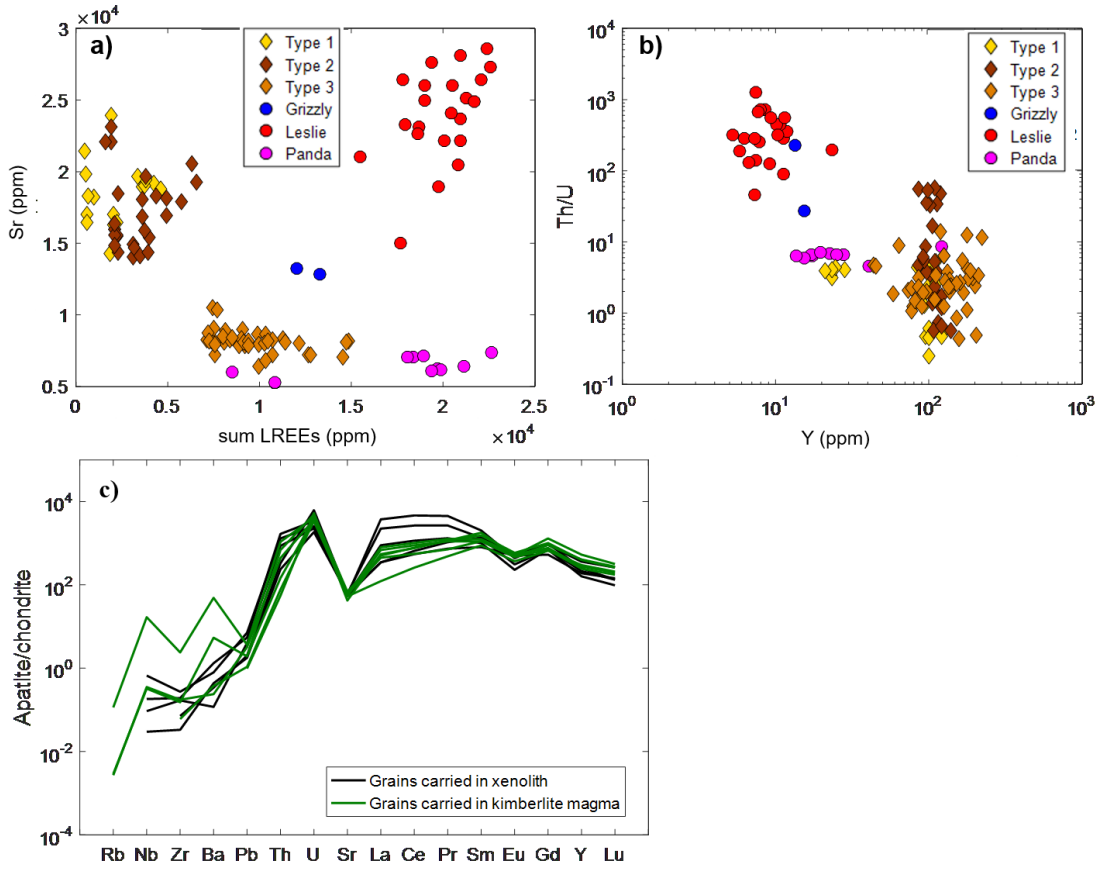


Figure 4.3 Major and trace element composition of apatite, a) Sr vs. LREEs in apatite interpreted as kimberlite-derived, showing anomalously high REEs and Sr in Leslie and Grizzly apatite grains, b) Th/U vs. Y in kimberlite-derived apatite, showing anomalously high Th/U in Leslie and Grizzly apatite grains, c) trace element analyses of apatite grains from Koala, comparison of grains sitting in xenoliths with grains in contact with kimberlite magma.

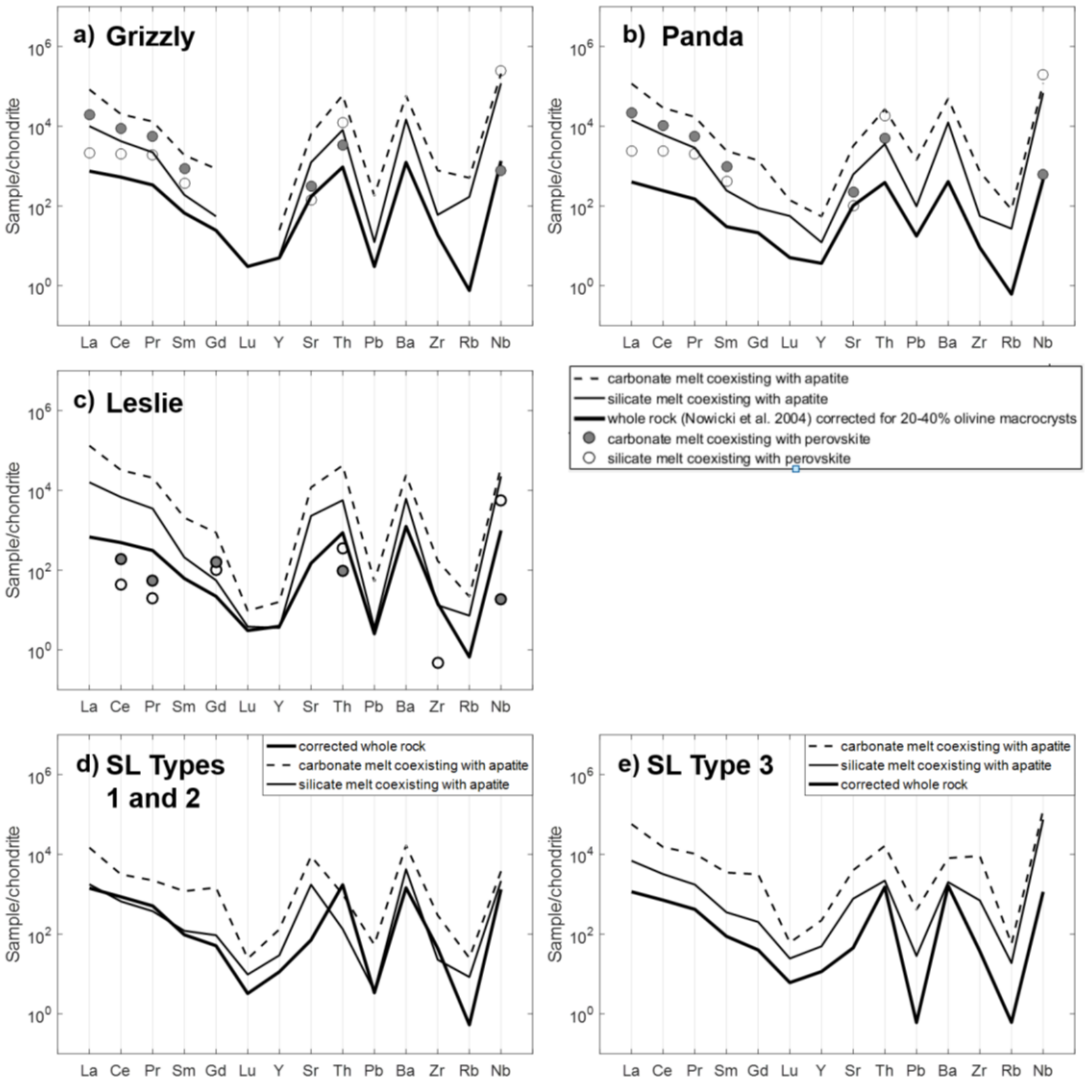


Figure 4.4 Hypothetical melts calculated from natural apatite compositions (this study), apatite partition coefficients (Klemme and Dalpé 2003; Prowatke and Klemme 2006), natural perovskite compositions (Canil and Bellis 2007; Kressall 2015), and perovskite partition coefficients (Beyer et al. 2013). Leslie and Grizzly kimberlite bulk rock concentrations are corrected for 20% macrocrystal olivine concentrations, Panda for 40%, Snap Lake Types 1 and 2 for 25% macrocrysts, Snap Lake Type 3 for 20% macrocrysts.

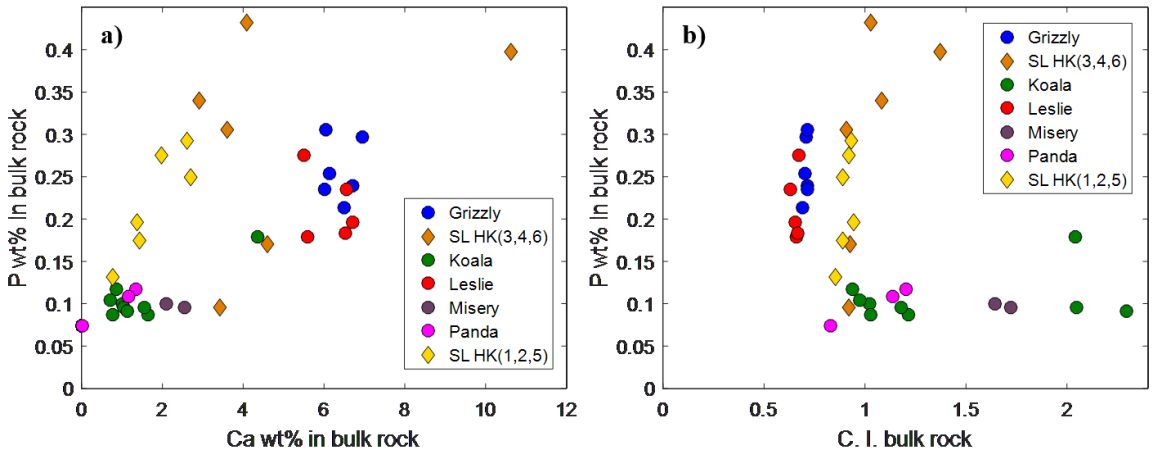


Figure 4.5 Bulk rock compositions of the selected kimberlite pipes a) P vs. Ca, b) P vs. C. I. (contamination index, as described by equation 11).

# CHAPTER 5 CONCLUSIONS

## 5.1 Conclusions

1) The occurrence of groundmass apatite is diverse and varied in kimberlite pipes from the Ekati Diamond Mine and the Snap Lake kimberlite dyke. Apatite has a wide variation in abundance, textures, zoning and composition in the studied pipes. Most kimberlitic apatite studied here is hydroxy-fluorapatite with high contents of Sr and REEs (up to 3 wt% each) and simple to complex zoning patterns.
2) Kimberlitic apatite can be distinguished from apatite of other alkaline and ultramafic sources for exploration. Apatite grains from Snap Lake kimberlite, however, overlap significantly and slightly with the fields for lherzolitic and carbonatitic apatite, respectively. However, kimberlite-derived apatite grains from the Ekati Diamond Mine pipes plot distinctly outside the fields defined by Belousova et al. (2002) for discerning apatite petrogenesis. This result opens the possibility of using apatite in drift material or sediment sampling as a kimberlite indicator mineral, provided the mineral separation methods account for typical kimberlitic-apatite size.
3) Trace element histories, as recorded in groundmass apatite reasonably support models for kimberlite eruption and evolution. In the case of Leslie, Snap Lake and possibly Grizzly, the grains seem to preserve evidence of fluid exsolution, in apatite textures, and in the Sr-rich compositions. The compositional and textural similarities of apatite grains from the altered zones of Snap Lake and Panda are remarkable, and similar crystallization conditions are suggested in carbonate-rich melt for these two populations of apatite. Koala, Misery and Beartooth kimberlite melts appear not to have reached apatite-saturation.

## 5.2 Future directions

Given the complexity and diversity of kimberlite systems, the sample number used for this study of the Ekati pipes was very small. A more comprehensive set of observations through the range of different facies in each kimberlite should be undertaken, to obtain a more comprehensive understanding of the occurrence and variability of apatite in kimberlite groundmass. Particularly for the kimberlite bodies which seem to have multiple stages of

eruption and crater infill, such as Panda, Misery and Koala, changes through the different stages of kimberlite crater development could be significant.

Little empirical information exists about the behaviour of trace elements between apatite and kimberlitic melts. To more effectively model the distribution of REEs, Sr and other indicators during kimberlite groundmass crystallization, experiments should be conducted for a range of possible kimberlitic compositions to test the behaviour of REEs and Sr in the presence of apatite.

For further development of this project, it would be interesting to more extensively model the fractionation of trace elements in multiple stages; with fluid separation before apatite crystallization, fluid separation after crystallization, and the inclusion of perovskite in the fractionation trends. In this way, more close models could be developed to match the resultant compositions observed in the bulk rock with those obtained from the hypothetical melts.

Lastly, more research is needed to investigate the full range of apatite compositions and substitutions in kimberlite systems. Given the complex and unique nature of kimberlite melts, it is expected that the resultant apatite species are equally varied and complex. While this study only accounted for the most common types of substitution in apatite during this study, there exists a diverse spectrum of minerals within the apatite supergroup, and their occurrence in relation to kimberlite could be more widely explored.

## References


Abersteiner, A., Kamenetsky, V.S., Kamenetsky, M., Goemann, K., Ehrig, K., and Rodemann, T. 2017. Significance of halogens (F, Cl) in kimberlite melts: Insights from mineralogy and melt inclusions in the Roger pipe (Ekati, Canada). Chemical Geology Available from http://dx.doi.org/10.1016/j.chemgeo.2017.06.008.

Allègre, C.J., Provost, A., and Jaupart, C. 1981. Oscillatory zoning: a pathological case of crystal growth. Nature **294**: 223-228.

Armstrong, J.P., Wilson, M., Barnett, R.L., Nowicki, T., and Kjarsgaard, B.A. 2004. Mineralogy of primary carbonate-bearing hypabyssal kimberlite, Lac de Gras, Slave Province, Northwest Territories, Canada. Lithos **76**: 415-433.

Ayers, J.C., and Watson, E.B. 1993. Apatite/fluid partitioning of rare-earth elements and strontium: Experimental results at 1.0 GPa and $1000^0$ C and application to models of fluid-rock interaction. Chemical Geology **110**: 299-314.

Bali, E., Audétat, A., and Keppler, H. 2011. The mobility of U and Th in subduction zone fluids: an indicator of oxygen fugacity and fluid salinity. Contributions to Mineralogy and Petrology **161**: 597-613.

Belousova, E.A., Griffin, W.L., O'Reilly, S.Y., and Fisher, N.I. 2002. Apatite as an indicator mineral for mineral exploration: trace-element compositions and their relationship to host rock type. Journal of Geochemical Exploration **76**: 45-69.

Berg, G.W., and Carlson, J.A. 1998. The Leslie kimberlite pipe of Lac de Gras, Northwest Territorries, Canada: evidence for near surface hypabyssal emplacement. *In* Extended Abstracts 7th International Kimberlite Conference, Cape Town. pp. 81-83.

Beyer, C., Berndt, J., Tappe, S., and Klemme, S. 2013. Trace element partitioning between perovskite and kimberlite to carbonatite melt: New experimental constraints. Chemical Geology **363**(132-139).

Boyce, J.W., Tomlinson, S.M., McCubbin, F.M., Greenwood, J.P., and Treiman, A.H. 2014. The lunar apatite paradox. Science **344**: 400-402.

Brenan, J.M. 1993. Partitioning of fluorine and chlorine between apatite and aqueous fluids at high pressure and temperature: implications for the F and Cl content of high P-T fluids. Earth and Planetary Science Letters **117**: 251-263.

Canil, D., and Bellis, A.J. 2007. Ferric iron in CaTiO3 perovskite as an oxygen barometer for kimberlite magmas II: applications. Journal of Petrology **48**: 231-252.

Cherniak, D.J. 2000. Rare earth element diffusion in apatite. Geochemica et Cosmochimica Acta **64**: 3871-3885.

Clement, C.R. 1982. A comparative geological study of some major kimberlite pipes in the Northern Cape and Orange Free State. University of Capetown.

Creaser, R.A., Grütter, H.S., Carlson, J., and Crawford, B. 2004. Macrocrystal phlogopite Rb-Sr dates for the Ekati property kimberlites, Slave Province, Canada: evidence for multiple intrusive episodes in the Paleocene and Eocene. Lithos **76**: 399-414.

Dawson, J.B., and Hinton, R.W. 2003. Trace-element content and partitioning in calcite, dolomite and apatite in carbonatite, Phalaborwa, South Africa. Mineralogical Magazine **67**: 921-930.

Drake, M.J., and Weill, D.F. 1972. New rare earth element standards for electron microprobe analysis. Chemical Geology **10**: 179-181.

Fedortchouk, Y., and Canil, D. 2004. Intensive variables in kimberlite magmas, Lac de Gras, Canada and implications for diamond survival. Journal of Petrology **45**: 1725-1745.

Fedortchouk, Y., Canil, D., and Carlson, J. 2005. Dissolution forms in Lac de Gras diamonds and their relationship to the temperature and redox state of kimberlite magma. Contributions to Mineralogy and Petrology **150**: 54-69.

Fedortchouk, Y., Matveev, S., and Carlson, J.A. 2010. $H_2O$ and $CO_2$ in kimberlitic fluid as recorded by diamonds and olivines in several Ekati Diamond Mine kimberlites, Northwest Territories, Canada. Earth and Planetary Science Letters **289**: 549-559.

Field, M., Gernon, T.M., Mock, A., Walters, A., Sparks, R.S.J., and Jerram, D.A. 2009. Variations of olivine abundance and grain size in the Snap Lake kimberlite intrusion, Northwest Territories, Canada: A possible proxy for diamonds. Lithos **1125**: 23-35.

Fleet, M.E., Liu, X., and Pan, Y. 2000a. Rare-earth elements in cloroapatite $[Ca_{10}(PO_4)_6Cl_2]$: Uptake, site preference, and degradation of monoclinic structure. Am Mineral **85**: 1437-1466.

Fleet, M.E., Liu, X., and Pan, Y. 2000b. Site preference of rare earth elements in hydroxyapatite $[Ca_{10}(PO_4)_6(OH)_2]$. J Solid State Chem **149**: 391-398.

Fleet, M.E., and Pan, Y. 1997. Rare earth elements in apatite: Uptake from $H_2O$-bearing phosphate-fluoride melts and the role of volatile components. Geochemica et Cosmochimica Acta **61**(22): 4745-4760.

Fulop, A., Kopylova, M.G., Ellemers, P., and Squibb, C. 2017. Geology of the Snap Lake kimberlite dyke, Northwest Territories, Canada, and its metasomatic interaction with grantie. *In* Long Abstracts 11th International Kimberlite Conference, Gaborone.

Gernon, T.M., Field, M., and Sparks, R.S.J. 2012. Geology of the Snap Lake kimberlite intrusion, Northwest Territories, Canada: field observations and their interpretation. Journal of the Geological Society, London **169**: 1-16.

Green, T.H., and Watson, E.B. 1982. Crystallization of apatite in natural magmas under high pressure, hydrous conditions, with particular reference to 'orogenic' rock series. Contributions to Mineralogy and Petrology **79**: 96-105.

Guillong, M., Meier, D.L., Allan, M.M., Heinrich, C.A., and Yardley, B.W.E. 2008. SILLS: a MATLAB-based program for the reduction of laser ablation ICP-MS data of homogenous materials and inclusions. *In* Laser ablation ICP-MS in the earth sciences: current practices and outstanding issues. *Edited by* P. Sylvester. Mineralogical Association of Canada Short Course Series, Vancouver, BC. pp. 328-333.

Gurney, J.J., Hildebrand, R.S., Carlson, J., Fedortchouk, Y., and Dyck, D. 2004. The morphological characteristics of diamonds from the Ekati property, Northwest Territories, Canada. Lithos **77**: 21-38.

Heaman, L.M., Kjarsgaard, B.A., and Creaser, R.A. 2004. The temporal evolution of North American kimberlites. Lithos **76**: 377-397.

Hervig, R.L., and Smith, J.V. 1981. Dolomite-apatite inclusion in chrome-diopside crystal, Bellsbank kimberlite, South Africa. American Mineralogist **66**: 346-349.

Hetman, C.M., Scott Smith, B.H., Paul, J.L., and Winter, F. 2004. Geology of the Gahcho Kué kimberlite pipes, NWT, Canada: root to diatreme magmatic transition zones. Lithos **76**: 51-74.

Höche, T., Moisescu, C., Avramov, I., and Rüssel, C. 2001. Microstructure of $SiO_2$-$Al_2O_3$-CaO-$P_2O_5$-$K_2O$-F- glass ceramics. 1. Needlelike versus isometric morphology of apatite crystals. Chemistry of Materials **13**: 1312-1319.

Hughes, J.M., Cameron, M., and Crowley, K.D. 1989. Structural variations in natural F, OH, and Cl apatites. American Mineralogist **74**: 870-876.

Hughes, J.M., and Rakovan, J. 2002. The crystal structure of apatite, $Ca_5(PO_4)_3(F,OH,Cl)$. Reviews in Mineralogy and Geochemistry **48**(1): 1-12.

Kempe, U., and Gotze, J. 2002. Cathodoluminescence (CL) behaviour and crystal chemistry of apatite from rare-metal deposits. Mineralogical Magazine **66**(1): 151-172.

Keppler, H., and Wyllie, P.J. 1990. Role of fluids in transport and fractionation of uranium and thorium in magmatic processes. Nature **348**: 531-533.

Klemme, S., and Dalpé, C. 2003. Trace-element partitioning between apatite and carbonatite melt. American Mineralogist **88**: 639-646.

Kopylova, M.G., Matveev, S., and Raudsepp, M. 2007. Searching for parental kimberlite melt. Geochemica et Cosmochimica Acta **71**: 3616-3629.

Kopylova, M.G., and Mogg, T. 2010. Mineralogy of the Snap Lake kimberlite, Northwest Territories, Canada, and compositions of phlogopite as records of it's crystallization. The Canadian Mineralogist **48**: 549-570.

Korzhinskiy, M.A. 1981. Apatite solid solutions as indicators of the fugacity of $HCl^0$ and $HF^0$ in hydrothermal fluids. Geokhimiya **5**: 689-706.

Kressall, R. 2015. Perovskite EPMA data for Ekati kimberlites. Unpublished data.

Kusebauch, C., John, T., Whitehouse, M.J., and Engvik, A.K. 2015a. Apatite as probe for the halogen composition of metamorphic fluids (Bamble Sector, SE Norway). Contributions to Mineralogy and Petrology **170**: 1-20.

Kusebauch, C., John, T., Whitehouse, M.J., Klemme, S., and Putnis, A. 2015b. Distribution of halogens between fluid and apatite during fluid-mediated replacement processes. Geochemica et Cosmochimica Acta **170**: 225-246.

Larson, E.E., and Amini, M.H. 1981. Fission-track dating of the Green Mountain kimberlite diatreme, near Boulder, Colorado. The Mountain Geologist **18**(1): 19-22.

Malarkey, J., Pearson, D.G., Kjarsgaard, B.A., Davidson, J.P., Nowell, G.M., Ottley, C.J., and Stammer, J. 2010. From source to crust: Tracing magmatic evolution in a kimberlite and a melilitite using microsample geochemistry. Earth and Planetary Science Letters **299**: 80-90.

Mallmann, G., and O'Neill, H.S.C. 2009. The crystal/melt partitioning of V during mantle melting as a function of oxygen fugacity compared with some other elements (Al, P, Ca, Sc, Ti, Cr, Fe, Ga, Y, Zr and Nb). Journal of Petrology **50**: 1765-1794.

Mao, M., Rukhlov, A.S., Rowins, S.M., Spence, J., and Coogan, L.A. 2016. Apatite trace element compositions: a robust new tool for mineral exploration. Economic Geology **111**: 1187-1222.

McDonough, W.F., and Sun, S.-s. 1995. The composition of the Earth. Chemical Geology **120**: 223-253.

Mitchell, R.H. 2004. Experimental studies At 5-12 GPa of the Ondermatjie hypabyssal kimberlite. Lithos **76**: 551-564.

Mitchell, R.H., Xiong, J., Mariano, A.N., and Fleet, M.E. 1997. Rare-earth-element-activated cathodoluminescence in apatite. The Canadian Mineralogist **35**: 979-998.

Moussallam, Y., Morizet, Y., and Gaillard, F. 2016. $H_2O$-$CO_2$ solubility in low $SiO_2$-melts and the unique mode of kimberlite degassing and emplacement. Earth and Planetary Science Letters **447**: 151-160.

Moussallam, Y., Morizet, Y., Massuyeau, M., Laumonier, M., and Gaillard, F. 2015. $CO_2$ solubility in kimberlite melts. Chemical Geology **418**: 198-205.

Nowicki, T., Crawford, B., Dyck, D., Carlson, J., McElroy, R., Oshust, P., and Helmstaedt, H. 2004. The geology of kimberlite pipes of the Ekati property, Northwest Territories, Canada. Lithos **76**: 1-27.

Nowicki, T., Porritt, L., Crawfor, B., and Kjarsgaard, B. 2008. Geochemical trends in kimberlites of the Ekati property, Northwest Territories, Canada: Insights on volcanic and resedimentation processes. Journal of Volcanology and Geothermal Research **174**: 117-127.

O'Reilly, S.Y., and Griffin, W.L. 2000. Apatite in the mantle: implications for metasomatic processes and high heat production in Phanerozoic mantle. Lithos **53**: 217-232.

Pan, Y., and Fleet, M.E. 2002. Compositions of the apatite-group minerals: substitution mechanisms and controlling factors. Reviews in Mineralogy and Geochemistry **48**(1): 13-49.

Piccoli, P.M., and Candela, P.A. 1994. Apatite in felsic rocks: a model for the estimation of initial halogen concentrations in the Bishop Tuff (Long Valley) and tuolumne intrusive suite (Sierra Nevada Batholith) magmas. American Journal of Science **294**: 92-135.

Piccoli, P.M., and Candela, P.A. 2002. Apatite in Igneous Systems. Reviews in Mineralogy and Geochemistry **48**: 255-292.

Porritt, L., Cas, R.A.F., Schaeffer, B., and McKnight, S.W. 2012. Textural analysis of strongly altered kimberlite: examples from the Ekati Diamond Mine, Northwest Territories, Canada. The Canadian Mineralogist **50**: 625-641.

Price, S.E., Russell, J.K., and Kopylova, M.G. 2000. Primitive magma from the Jericho pipe, N.W.T., Canada: constraints on primary kimberlite melt chemistry. Journal of Petrology **41**(6): 789-808.

Prowatke, S., and Klemme, S. 2006. Trace element partitioning between apatite and silicate melts. Geochemica et Cosmochimica Acta **70**: 4513-4527.

Reed, R.M., and Milliken, K.L. 2003. How to overcome imaging problems associated with carbonate minerals on SEM-based cathodoluminescence systems. Journal of Sedimentary Research **73**: 328-332.

Robertson, M.D., and Gibson, S.J. 2014. The calibration, optimization and avoidance of artifacts of a cathodoluminescene system. *In* Cathodoluminescence and its application to geoscience. *Edited by* I.M. Coulson. Mineralogical Association of Canada Short Course series, Fredericton, NB. pp. 11-27.

Rønsbo, J.G. 1989. Coupled substitutions involving REEs and Na and Si in apatites in alkaline rocks from the Ilimaussaq intrusion, South Greenland, and the petrological implications. Am Mineral **74**: 896-901.

Russell, J.K., Porritt, L.A., Lavallée, Y., and Dingwell, D.B. 2012. Kimberlite ascent by assimilation-fuelled buoyancy. Nature **481**: 352-356.

Ryerson, F.J., and Hess, P.C. 1978. Implications of liquid-liuid distribution coefficients to mineral-liquid partitioning. Geochemica et Cosmochimica Acta **42**: 921-932.

Scott Smith, B.H., Nowicki, T.E., Russell, J.K., Webb, K.J., Mitchell, R.H., Hetman, C.M., Harder, M., Skinner, E.M.W., and Robey, J.A. 2013. Kimberlite terminology and classification. *In* 10th International Kimberlite Conference. *Edited by* D.G. Pearson and H.S. Grütter and J.W. Harris and B.A. Kjarsgaard and H. O'Brien and N.V.C. Rao and S. Sparks. Springer, New Dehli.

Sparks, R.S.J., Brooker, R.A., Field, M., Kavanagh, J., Schumacher, J.C., Walter, M.J., and White, J. 2009. The nature of erupting kimberlite melts. Lithos **1125**: 429-438.

Stone, R.S., and Luth, R.W. 2016. Orthopyroxene survival in deep carbonatite melts: implications for kimberlites. Contributions to Mineralogy and Petrology **171**.

Stormer, J.C., and Carmichael, I.S.E. 1971. Fluorine-hydroxyl exchange in apatite and biotite: a potential igneous geothermometer. Contributions to Mineralogy and Petrology **31**: 121-131.

Stormer, J.C., Jr., Pierson, M.L., and Tacker, R.C. 1993. Variation of F and Cl X-ray intensity due to anisotropic diffusion in apatite during electron microprobe analysis. American Mineralogist **78**: 641-648.

Tepper, J.H., and Kuehner, S.M. 1999. Complex zoning in apatite from the Idaho batholith: A record of magma mixing and intracrystalline trace element diffusion. American Mineralogist **84**(581-595).

Tollari, N., Baker, D.R., and Barnes, S.-J. 2008. Experimental effects of pressure and fluorine on apatite saturation in mafic magmas, with reference to layered intrusions and massif anorthosites. Contributions to Mineralogy and Petrology **156**: 161-175.

Votyakov, S.L., Ilupin, I.P., Krasnobayev, A.A., Krokhalev, V.Y., and Chernyshev, Y.V. 1989. ESR and luminescence of Siberian kimberlite zircon and apatite. Geochemistry International **26**: 5-8.

Watson, E.B. 1976. Two-liquid partition coefficients: experimental data and geochemical implications. Contributions to Mineralogy and Petrology **56**: 119-134.

Watson, E.B. 1980. Apatite and phosphorus in mantle source regions: and experimental study of apatite/melt equilibria at pressures to 25 kbar. Earth and Planetary Science Letters **51**: 322-335.

Watson, E.B., and Green, T.H. 1981. Apatite/liquid partition coefficients for the rare earth elements and strontium. Earth and Planetary Science Letters **56**: 405-421.

Webster, J.D., and Piccoli, P.M. 2015. Magmatic apatite: a powerful, yet deceptive, mineral. Elements **11**(3): 177-182.

White, J.L., Sparks, R.S.J., Bailey, K., Barnett, W.P., Field, M., and Windsor, L. 2012. Kimberlite sills and dykes associated with the Wesselton kimberlite pipe, Kimberley, South Africa. South African Journal of Geology **115.1**: 1-32.

Wyllie, P.J., Cox, K.G., and Biggar, G.M. 1962. The habit of apatite in synthetic systems and igneous rocks. Journal of Petrology **3**: 238-243.

Zajacz, Z., Halter, W.E., Pettke, T., and Guillong, M. 2008. Determination of fluid/melt partition coefficients by LA-ICPMS analysis of co-existing fluid and silicate melt

inclusions: controls on element partitioning. Geochemica et Cosmochimica Acta **72**: 2169-2197.

Zhang, Z., Fedortchouk, Y., and Hanley, J.J. 2015. Evolution of diamond resorption in a silicic aqueous fluid at 1-3 GPa: application to kimberlite emplacement and mantle metasomatism. Lithos **227**: 179-193.

Zhu, C., and Sverjensky, D.A. 1991. Partitioning of F-Cl-OH between minerals and hydrothermal fluids. Geochemica et Cosmochimica Acta **55**: 1837-1858.

Zhu, C., and Sverjensky, D.A. 1992. F-Cl-OH partitioning between biotite and apatite. Geochemica et Cosmochimica Acta **56**: 3435-3467.

# Appendix A List of Samples

Table A-1 List of samples and methods applied for Ekati Diamond Mine kimberlite pipes.

| Kimberlite | Sample ID | SEM | WDS | CL | LA-ICPMS |
|---|---|---|---|---|---|
| **Koala** | K1 | x | x | | x |
| | K2 | x | x | x | x |
| **Misery** | M1 | x | | | |
| | M2 | x | | | |
| **Beartooth** | B1 | x | | x | |
| | B2 | x | | | |
| **Panda** | P1 | x | x | x | x |
| | P2 | x | x | | x |
| **Leslie** | L1 | x | x | x | x |
| | L2 | x | x | x | x |
| **Grizzly** | G1 | x | x | | x |
| | G2 | x | x | x | x |

Table A-2 List of samples and methods applied for Snap Lake kimberlite.

| Kimberlite | | Sample ID | SEM | WDS | CL | LA-ICPMS |
|---|---|---|---|---|---|---|
| **Snap Lake** | **HK1** | 511 | x | x | | x |
| | | 211 | x | | | |
| | | 7311 | x | x | | x |
| | | 311 | x | | | |
| | | 9411 | x | x | x | x |
| | **HK2** | 2166 | x | | | |
| | | 611 | x | | | |
| | | 9111 | x | | | |
| | | 2111 | x | x | x | x |
| | | 2168 | x | | | |
| | **HK3** | 2123 | x | x | | x |
| | | 2145 | | | | |
| | | 7811 | x | x | | x |
| | | 3511 | | | | |
| | | 3711 | | | | |
| | **HK4** | 811 | | | | |
| | | 2125 | x | x | x | x |
| | | 8512 | x | x | | x |
| | | 3911 | | | | |
| | | 1511 | | | | |
| | **HK5** | 9711 | x | x | x | x |
| | | 911 | x | | | |
| | | 9911 | x | | | |
| | | 6511 | x | x | | |
| | | 9811 | x | x | | x |
| | **HK6** | 611 | x | | | |
| | | 2172 | x | | | |
| | | 3211 | x | x | | x |
| | | 6911 | x | x | x | x |
| | | 1934 | x | | | |
| | **Xenolith** | 8011 | x | x | | |
| | | 4611 | x | x | x | x |

## Appendix B Cathodoluminescence images and spectra

CL images and spectra collected of apatite from the selected kimberlites. Yellow squares outline location of spectrum, yellow letters denote spectrum label. Identification of peaks based on Kempe and Götze (2002) and Mitchell et al. (1997).

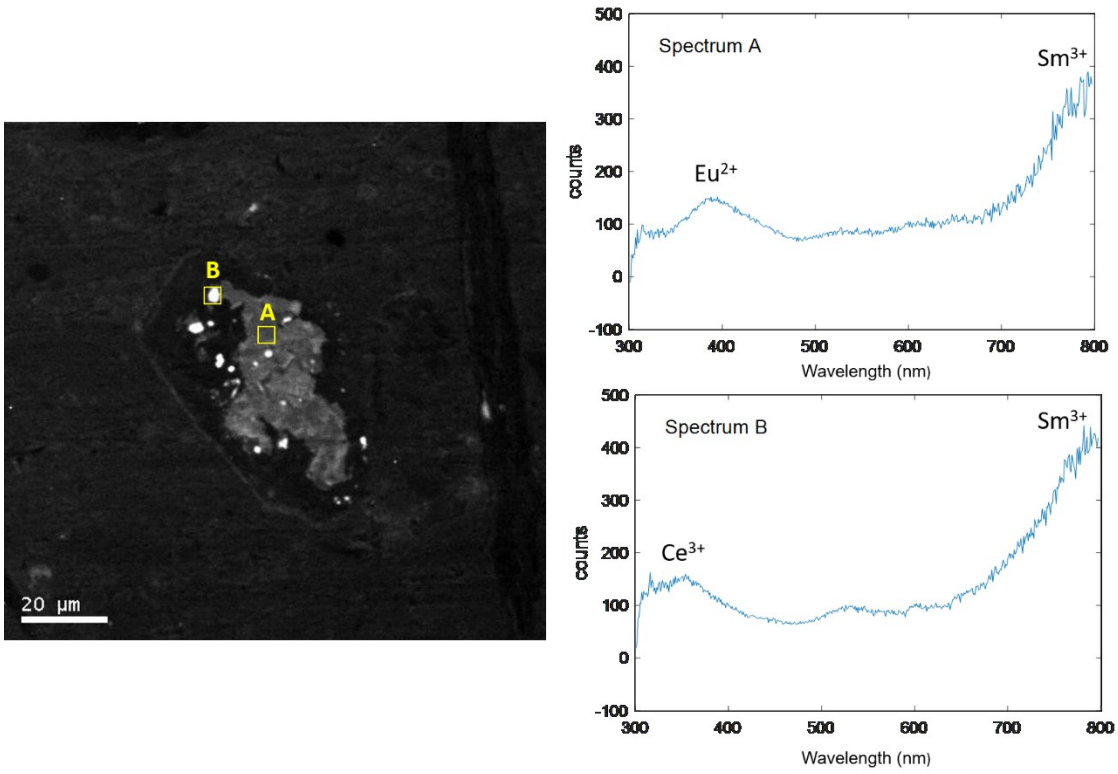


Figure B-1 CL spectra of apatite grain from Koala

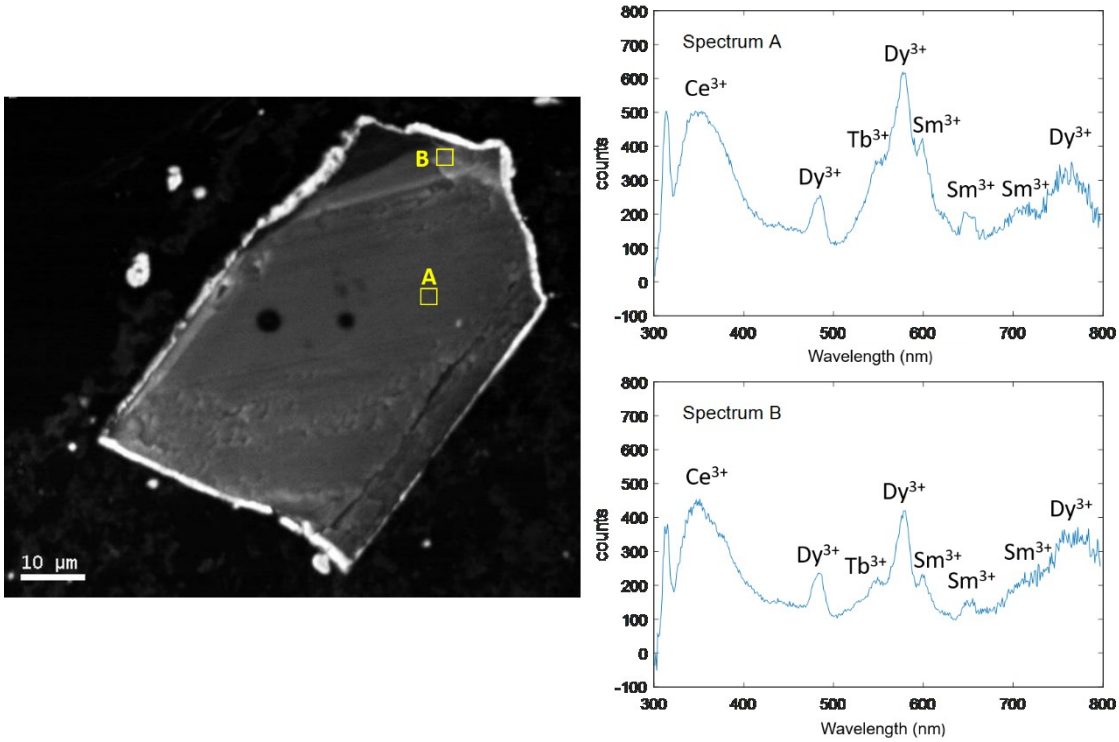


Figure B-2 CL spectra of apatite grain from Grizzly

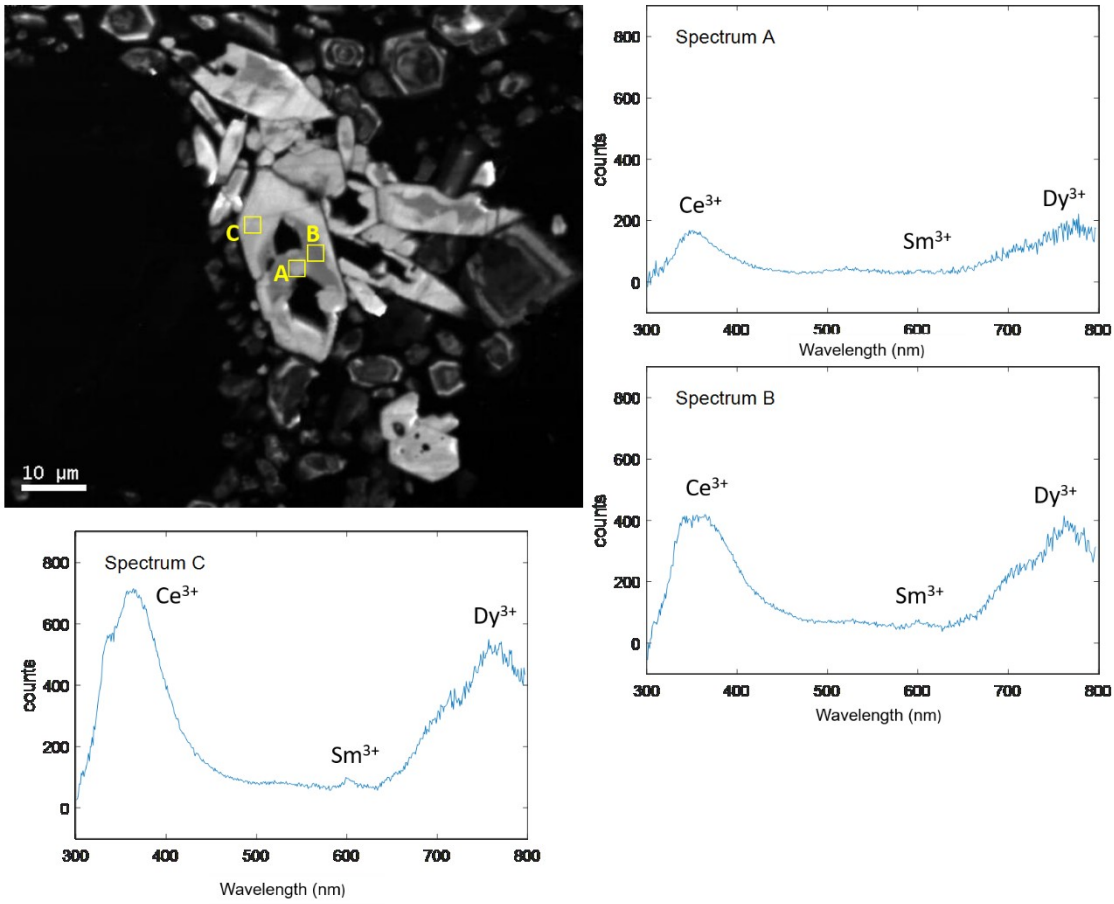


Figure B-3 CL spectra of apatite grains from Leslie

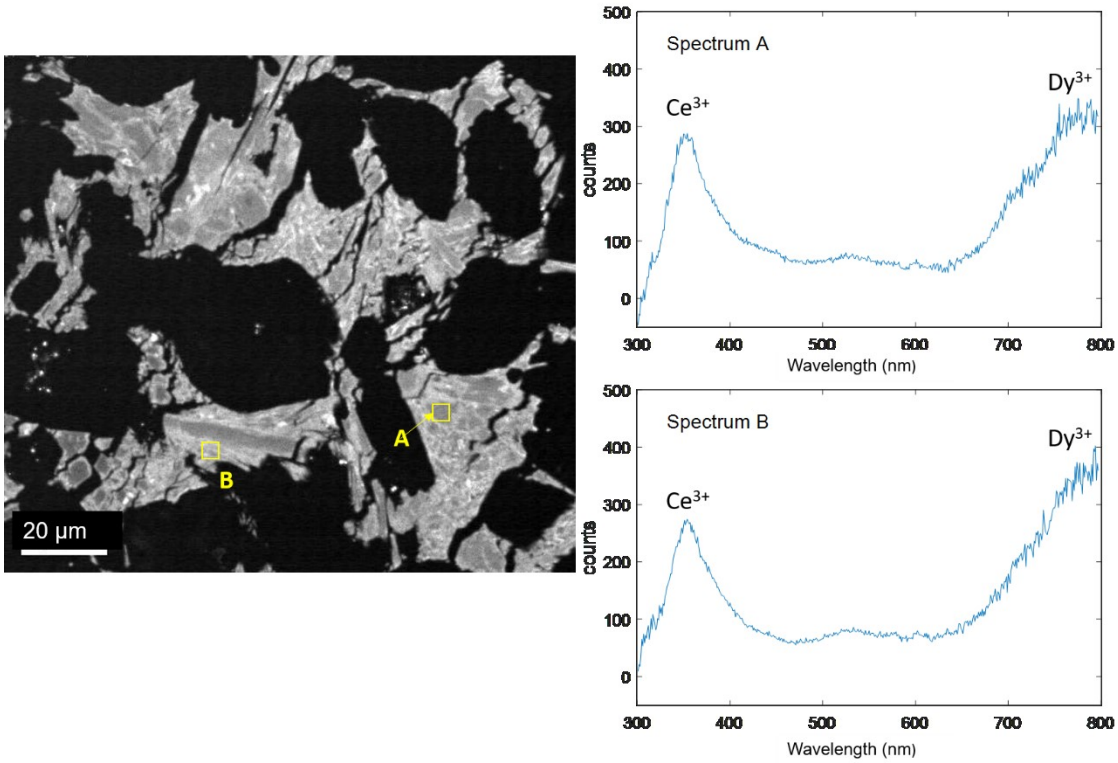


Figure B-4 CL spectra of apatite grain from Snap Lake; Type 1.

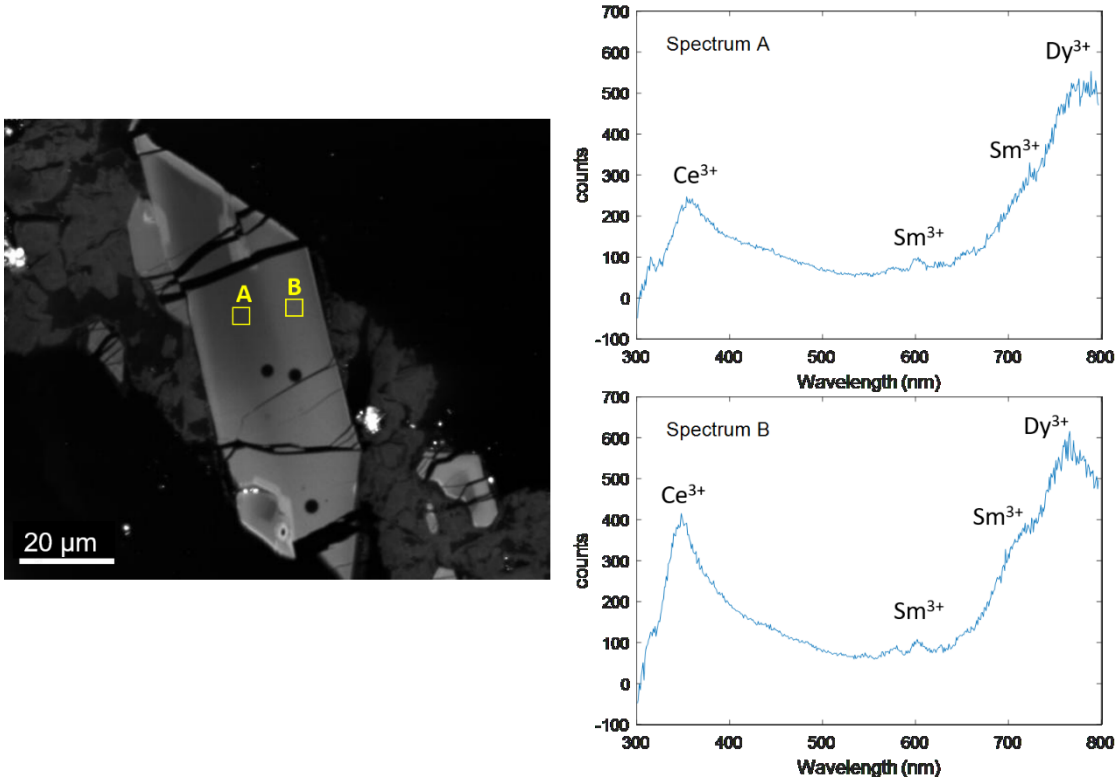


Figure B-5 CL spectra of apatite grain from Snap Lake; Type 2.

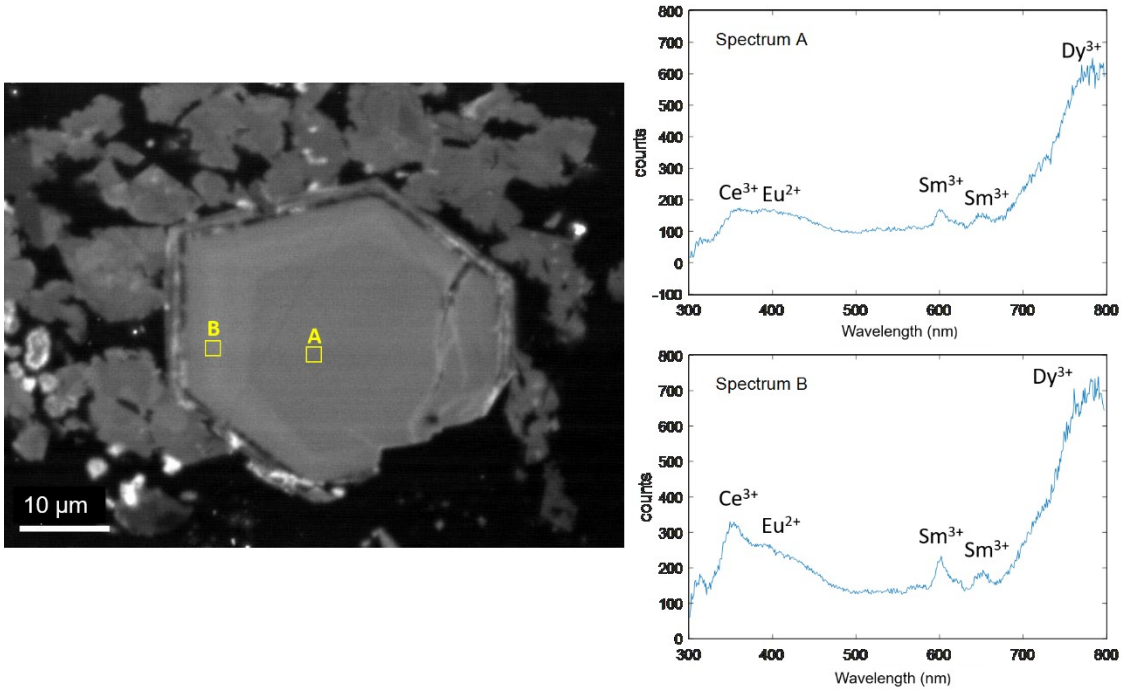


Figure B-6 CL spectra of apatite grain from Snap Lake; Type 3.

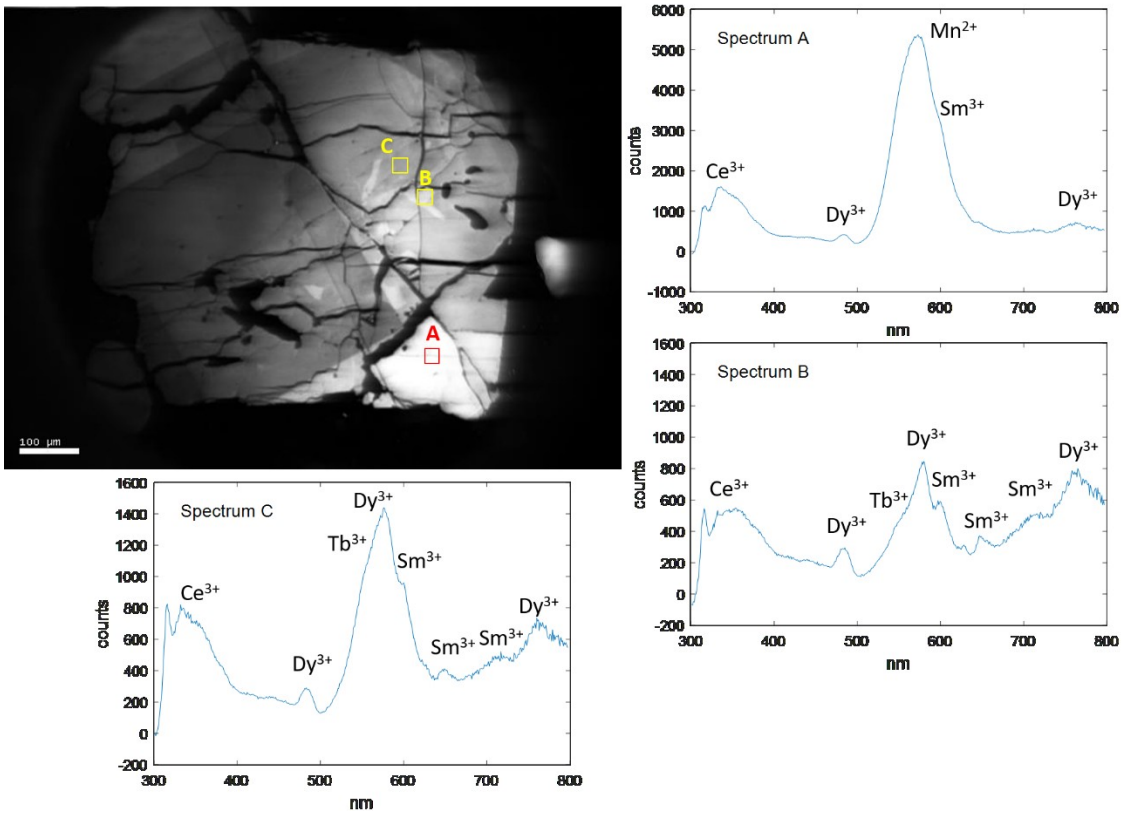


Figure B-7 CL spectra of apatite from Snap Lake HK6; Type 4.

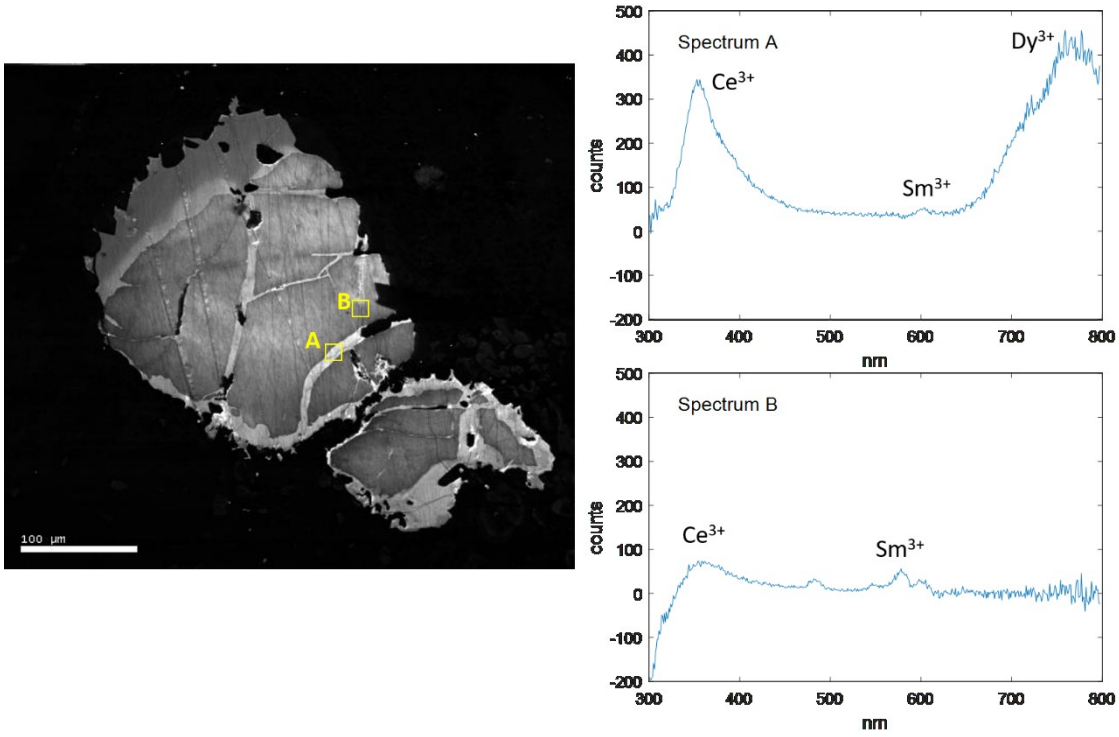


Figure B-8 CL spectra of xenocrystic apatite grain from Leslie

## Appendix C Electronic Supplementary Data

Supplementary data in electronic appendix is available through DalSpace, and includes:

1) All major and trace element analyses (including limits of detection) of apatite from this study,
2) Major element analyses of core-rim pairs in apatite,
3) Major and trace element analyses from track study of Leslie xenocryst